General Disclaimer

One or more of the Following Statements may affect this Document

- This document has been reproduced from the best copy furnished by the organizational source. It is being released in the interest of making available as much information as possible.

- This document may contain data, which exceeds the sheet parameters. It was furnished in this condition by the organizational source and is the best copy available.

- This document may contain tone-on-tone or color graphs, charts and/or pictures, which have been reproduced in black and white.

- This document is paginated as submitted by the original source.

- Portions of this document are not fully legible due to the historical nature of some of the material. However, it is the best reproduction available from the original submission.

STRESS ANALYSIS, THERMOMECHANICAL FATIGUE EVALUATION, AND ROOT SUBCOMPONENT TESTING OF GAMMA/GAMMA PRIME-DELTA EUTECTIC ALLOY

by

K. D. Sheffler and J. J. Jackson

PRATT & WHITNEY AIRCRAFT
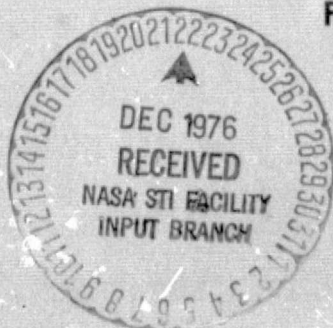DIVISION OF UNITED TECHNOLOGIES CORPORATION
EAST HARTFORD, CONNECTICUT

December 1976

prepared for

NATIONAL AERONAUTICS AND SPACE ADMINISTRATION

FINAL REPORT

1. Report No.	2. Government Accession No.	3. Recipient's Catalog No.
NASA CR-135005		

4. Title and Subtitle	5. Report Date
Stress Analysis, Thermomechanical Fatigue Evaluation, and Root Subcomponent Testing of Hollow Blades of Gamma/Gamma Prime-Delta Eutectic Alloy	December 1976
	6. Performing Organization Code

7. Author(s)	8. Performing Organization Report No.
K.D. Sheffler and J.J. Jackson	PWA 5472
	10. Work Unit No.

9. Performing Organization Name and Address	
Pratt & Whitney Aircraft Division United Technologies Corporation East Hartford, Connecticut	11. Contract or Grant No.
	NAS3-19714, NAS3-19732
	13. Type of Report and Period Covered

12. Sponsoring Agency Name and Address	
National Aeronautics and Space Administration Washington, D.C. 20546	Contractor Report
	14. Sponsoring Agency Code

15. Supplementary Notes

Project Manager Fredric H. Harf, Materials and Structures Division, NASA Lewis Research Center, Cleveland, Ohio

16. Abstract

Thermomechanical fatigue (TMF) and root subcomponent tensile, creep, and low cycle fatigue (LCF) tests were conducted to determine the capability of a fully lamellar Ni-20.1w/oCb-2.5w/oAl-6.0w/oCr-0.06w/oC,γ/γ' - δ directionally solidified eutectic alloy to sustain the airfoil thermal fatigue and root attachment loads anticipated in advanced, hollow, high work turbine blades. A three dimensional finite element elastic stress analysis was performed on typical advanced hollow eutectic airfoil and root-platform designs to determine appropriate conditions for these tests. Results of TMF tests conducted on longitudinal specimens (stress axis parallel to the solidification direction) containing a simulated leading edge cooling hole pattern indicated the longitudinal TMF properties to be more than adequate for the particular advanced hollow blade analyzed, with the strain range for a 10^4 cycle life being more than 50% above the maximum strain range calculated for the advanced hollow blade. Transverse TMF properties (stress axis perpendicular to the solidification direction) are lower than longitudinal properties, but appear adequate. Based on results obtained from a transverse specimen containing simulated cooling holes, a thermal fatigue life in the order of 14,000 cycles is predicted for the particular blade analyzed. Root subcomponent test results indicate that the short term load carrying capability of the eutectic is suitable for advanced attachment applications. Root LCF properties appear marginal, while the sustained load (creep) attachment capability of the eutectic is not satisfactory for advanced blade applications, with a root creep life on the order of 4-20 hours being measured at typical advanced attachment load and temperature conditions. A fabricated blade, incorporating a D.S. eutectic airfoil bonded to a superalloy root, is suggested as the best approach for application of γ/γ' - δ as an advanced hollow turbine blade material.

17. Key Words (Suggested by Author(s))	18. Distribution Statement
Eutectic, Turbine Alloys Directional Solidification Mechanical Properties Thermal Fatigue, Stress Analysis	Unclassified-Unlimited

19. Security Classif. (of this report)	20. Security Classif. (of this page)	21. No. of Pages	22. Price*
Unclassified	Unclassified	92	

NASA-C-168 (Rev. 6-71)

FOREWORD

This report describes work performed by the Pratt & Whitney Aircraft Division of the United Technologies Corporation for the Lewis Research Center of the National Aeronautics and Space Administration under Contract NAS3-19714 and NAS3-19732. The program was administered for Pratt & Whitney Aircraft by Dr. K.D. Sheffler, Program Manager, with assistance provided by Mr. J.J. Jackson and Mrs. D.A. Boychuck. Airfoil Stress Analysis was performed by Mr. J.V. Ruberto under the supervision of Mr. M. Sette. Root Stress Analysis was performed by Mr. W.H. Ask under the direction of Mr. J. Rieder. Mr. A.E. Gemma acted as a consultant for both of these analytical programs. Dr. M.L. Gell and Dr. G.R. Leverant acted as technical consultants to the program. The NASA Project Manager was Mr. F.H. Harf, with Dr. H.R. Gray acting as consultant.

TABLE OF CONTENTS

1.0 SUMMARY

The objective of this program was to evaluate the capability of the direc-
tionally solidified γ/γ' - δ, lamellar, eutectic alloy to sustain the air-
foil thermal fatigue and root attachment loads expected in advanced, hollow,
high work turbine blades. To accomplish this objective, finite element, elastic
stress analyses were performed on typical advanced turbine blade and root
designs. Results of these analyses were used to establish test parameters
for thermomechanical fatigue, and root subcomponent tensile, creep, and low
cycle fatigue tests on eutectic specimens, and to evaluate the test results
in terms of predicted blade life. Results of these studies are summarized
in the following paragraphs.

1.1 STRESS ANALYSIS

Three dimensional finite element elastic stress analyses which reflect the aniso-
tropic physical and elastic properties of the directionally solidified (D.S.)
eutectic were performed in the airfoil and root-platform areas of typical
advanced, hollow, high work D.S. eutectic turbine blades. The primary objective
of the airfoil stress analysis was to determine the maximum spanwise (parallel
to the blade axis) and chordwise (transverse to the blade axis) thermomechanical
strain ranges and the strain-temperature phase relationships in an advanced,
film cooled hollow eutectic airfoil. Results indicated maximum strain ranges
on the airfoil are comparable to those that would be obtained for the same airfoil
made from D.S. Mar-M200+Hf, an advanced D.S. nickel base superalloy. In the span-
wise direction, a maximum strain range of 0.0016m/m was calculated in the eutectic
airfoil, as compared to a D.S. Mar-M200+Hf strain range of 0.0020m/m. The
spanwise strain-temperature phase relationship tended toward Cycle I (maxi-
mum tension applied at minimum temperature, maximum compression applied at
maximum temperature). A maximum chordwise strain range of 0.0018m/m was
calculated for the eutectic blade, as compared to 0.0014m/m for D.S. Mar-
M200+Hf, with the chordwise strain-temperature phase relationship tending
toward a symmetrical cycle shape (i.e., maximum tensile and compressive
strains both occurring at an intermediate temperature).

Based on results of an earlier program (Contract NAS3-17811), which indi-
cated that the design-limiting property of γ/γ' - δ might be intermediate
temperature strength in shear parallel to the solidification direction,
attention in the root-platform analysis was focused on determination of
maximum radial shear stresses in an advanced eutectic attachment design.
Analytical results indicated local (concentrated) shear stresses approxi-
mately double the ultimate shear strength of γ/γ' - δ at the maximum blade
pull. As indicated in later paragraphs, where results of root subcomponent
tests are discussed, the load carrying capability of the eutectic attachment
was found to be significantly above that predicted from the stress analysis,
primarily because of local inelastic relaxation of concentrated stresses,
which was not reflected in the linear elastic stress analysis.

1

1.2 THERMOMECHANICAL FATIGUE TESTING

Results of thermomechanical fatigue tests conducted on coated* longitudinal and transverse γ/γ' - δ D.S. eutectic specimens using strain-temperature cycles calculated for the advanced eutectic airfoil indicated that the eutectic thermal fatigue properties should be adequate for advanced hollow blade applications, provided large transverse Cycle I strains do not occur. Large strains of this type were not found in the blade analyzed. The life-limiting thermal fatigue properties were measured on a transverse specimen containing a simulated cooling hole. Predicted TMF life for this mode of failure was on the order of 14,000 between 471 and 910°C (880 and 1670°F) for the particular advanced blade studied. Specific test results leading to this lifetime prediction are summarized in the following paragraphs.

Results obtained on smooth longitudi   fatigue specimens tested with the calculated spanwise advanced blade strain-temperature cycle indicated a strain range on the order of 0.0050m/m for 10^4 cycles to failure. This strain range is more than 3 times the maximum calculated blade strain range of 0.0016m/m. Increasing the cycle temperature from the 504-938C (940-1720°F) calculated range to a range of 427-1038C (800-1900°F) caused a slight reduction of properties, to an estimated 10^4 cycle strain range of about 0.0044m/m. The application of 427-1038C (800-1900°F) Cycle I loading caused a larger reduction of smooth longitudinal fatigue properties, with an extrapolated 10^4 cycle strain range of 0.0025m/m being obtained with this type of loading. The significant smooth longitudinal property reduction found with Cycle I loading was attributed to the influence of cycle shape on coating crack initiation, with the occurrence of high tensile strain at low temperatures being the driving force for early coating failure.

Testing of longitudinal "showerhead" specimens which contained an array of simulated leading edge cooling holes essentially eliminated the influence of cycle shape and temperature range on TMF life, with the strain range for 10^4 cycles to failure being on the same order as that estimated for smooth Cycle I loading ($\approx$0.0025m/m). Apparently the stress concentration caused by the presence of cooling holes provides a sufficient driving force for crack initiation to eliminate large differences caused by the influence of cycle shape on smooth specimen coating crack initiation. The longitudinal thermal fatigue properties of the eutectic showerhead specimens were comparable to those exhibited by B1900+Hf, a typical conventionally cast nickel base superall

As with smooth longitudinal specimens, cycle shape and temperature range were found to have a significant influence on smooth transverse TMF properties. Smooth transverse tests conducted with the calculated chordwise blade cycle indicated a strain range on the order of 0.0030m/m for a 10^4 cycle blade life. Increasing cycle temperature and changing the cycle shape to Cycle I reduced the 10^4 cycle strain range to respective values on the order of .0021 and .0015m/m. While the Cycle I result is below

---

* $\approx$ 64μm(2.5 mils) NiCrAlY + $\approx$ 6μm (0.25 mil) Pt.

the maximum calculated chordwise strain range, it is above the maximum chordwise strain range of 0.0012m/m calculated for Cycle I type loading, and does not represent the life-limiting thermal fatigue mode for the blade analyzed. The life limiting thermal fatigue mode was found on a specimen which contained a simulated cooling hole and was tested with the calculated chordwise engine cycle. Results of this test indicated a thermal fatigue life on the order of 14,000 cycles for the particular advanced hollow blade analyzed. It should be noted that this prediction, as well as the transverse Cycle I projection, are based on extrapolation of short time data obtained at relatively high strain ranges, and that additional testing would be desirable to confirm these predictions.

1.3 ROOT SUBCOMPONENT TESTS

Results of tensile, creep, and low cycle fatigue pull-out tests conducted on coated eutectic subcomponent attachment specimens indicate that sustained load (creep) shear pull-out of the eutectic root will likely be the design limiting property of $\gamma/\gamma' - \delta$ for advanced blade applications. As mentioned previously, results of tensile pull-out tests conducted at 760C (1400°F) indicate the short-term load carrying capability of a eutectic attachment to be significantly above that predicted by the linear elastic stress analysis. Triplicate pull tests indicated a failure load on the order of 356kN (80,000 lb.) for the blade analyzed, with failure occurring by tooth shear. When analyzed in terms of fully distributed tooth shear stress, this failure load corresponds to a shear stress very close to the 386MPa (56 ksi) ultimate shear strength of the eutectic composition tested, indicating that local plastic deformation fully relaxes the high concentrated stresses calculated in the linear elastic stress analysis.

While some difficulty was encountered in root LCF testing of the eutectic, test results indicate the LCF life of the advanced eutectic attachment to be at least 3000 cycles at the 222kN (50,000 lb.) maximum blade pull. This result is considered marginal in terms of advanced hollow blade applications.

As mentioned above, the design limiting property of the eutectic appears to be the sustained load carrying capability of the attachment. Sustained load pull-out tests conducted in the anticipated operating temperature range of 760-700C (1400-1300°F) resulted in pull-out lives in the range of 4 to 20 hours, which is not adequate for an advanced blade application. The concept of a fabricated blade having a D.S. eutectic airfoil bonded to a superalloy root therefore is proposed as the best approach for the successful application of $\gamma/\gamma' - \delta$ as a hollow blade material in advanced turbine engines. Implementation of this concept is considered to be within reach of current bonding technology.

2.0 INTRODUCTION

Advanced gas turbine engines which will operate with increased turbine
inlet temperatures and/or increased rotor speeds (higher blade stresses)
will require turbine materials with strength and temperature capabilities
beyond those of current generation nickel base superalloys. Directionally
solidified eutectic superalloys containing Ni_3Cb (δ phase) reinforcing
platelets in an Ni_3Al (γ') strengthened nickel-chrome matrix have a potential
temperature advantage of 56 to 83C° (100 to 150°F) at a given stress (or
40 to 60% increase in load carrying capability at a given temperature)
over the best directionally solidified nickel base superalloy and thus are
prime candidates to meet the challenge of advanced turbine material require-
ments.

Advanced high work turbine blades will be hollow to reduce weight and to
permit internal cooling, and will contain arrays of cooling holes to pro-
vide film cooling of the outer airfoil surface. Demonstration of the δ-
strengthened D.S. eutectic (γ/γ' - δ) as a viable advanced turbine material
requires additional characterization of mechanical behavior to evaluate the
capability of this alloy to sustain the airfoil thermal fatigue and root
attachment loads imposed in this type of advanced design. To meet these
requirements, this program was conducted to generate the appropriate stress
analysis for these advanced turbine blades and to initiate the required
laboratory testing for evaluation of key mechanical properties.

The analytical effort involved calculation of anticipated thermal fatigue
strain-temperature cycles, as well as root stress distribution, in advanced
high work eutectic turbine blades, using a three dimensional finite element
analysis technique which accounts for the anisotropic elastic properties of
the D.S. eutectic. The experimental effort included thermomechanical
fatigue testing of longitudinal and transverse γ/γ' - δ D.S. eutectic speci-
mens with and without simulated cooling holes using the strain-temperature
cycles determined from the stress analysis. Root subcomponent tensile,
creep, and fatigue tests also were conducted to evaluate the advanced blade
attachment capability of γ/γ' - δ. Based on results of these tests, life-
time predictions were made for advanced, hollow, high work D.S. eutectic
turbine blades.

3.0 STRESS ANALYSIS

The objective of this task was to determine the distribution of stress and strain in the airfoil and root-platform areas of advanced, hollow, high work D.S. eutectic turbine blades, using analytical methods which reflect the anisotropic physical properties of the D.S. γ/γ'-δ eutectic alloy (see Appendix). The general approach to achievement of this objective involved the use of a three dimensional linear elastic finite element computer program, ASKA (Automated System for Kinematic Analysis)[*]. Application of this technique involves break-up of the root-airfoil structure into a discrete number of three dimensional elements having directional characteristics representative of the anisotropic elastic properties of the eutectic alloy. These elements are connected at a discrete number of nodes to determine the response of the structure to applied loads or displacements. Definition of the finite element break-up is accomplished through use of an ASKA preprocessor which generates, labels, and assembles the nodes and elements into a mathematical model of the structure. Equilibrium equations are written for each node in terms of elements connected to that node and any external forces and boundary conditions that may be applied. The resulting system of simultaneous equations representing all nodes used to define the structure is solved to determine mechanical and/or thermal displacements associated with the applied loads. Stresses in each element are calculated from displacements using the known anisotropic elastic constants. Specific application of this technique to the eutectic airfoil and root-platform structures is discussed in the following sections.

3.1 AIRFOIL ANALYSIS

The objective of the airfoil analysis was to identify the location and magnitude of the most severe temperature-strain (thermal fatigue) cycles in a typical advanced, high work turbine blade, using the ASKA three dimensional analysis described above. The blade geometry selected for this analysis is an advanced design incorporating a large airfoil curvative (high camber) together with a high degree of film cooling provided via a large number of small cooling holes distributed over the entire airfoil surface (Figure 1). The approach to calculation of the strain and temperature distribution in this blade involved an ASKA finite element heat transfer analysis at a number of transient and steady state operating conditions to determine the temperature cycle and thermal expansion strains experienced at various locations in the airfoil. This information, coupled with variations of centrifugal load through each operating point, provided the desired information concerning the variations of strain and temperature through a typical engine operating cycle.

External boundary conditions for the heat transfer analysis were established by engine performance requirements analysis, which defines the temperature, pressure, and velocity distribution of the combustion gas envelope surrounding the airfoil. Internal boundary conditions were based on the amount of heat extracted from the interior by the cooling air, which is established on the basis of previous experience with similar blade designs.

---

[*]Additional information concerning this technique may be found in the ASKA Users Reference Manual, ISD Report No. 73, available from the University of Stuttgart, Stuttgart, Germany, 1971.

The three dimensional finite element analysis performed on the airfoil utilized the Hexc 20 element of the ASKA program. This element is a 20 noded isoparametric three dimensional element as shown in Figure 2. The structural model was built from 56 element groups consisting of nine elements per group assembled in a spanwise (radial) airfoil orientation. The airfoil was completely defined with 5206 nodal points resulting in 8012 unknowns and 208 suppressed degrees of freedom. Figure 3 shows the resulting modeling of the concave and convex walls.

Input at each node included the temperature dependence and anisotropy of the material properties (see Appendix). The three dimensional thermal loads were applied using thermal strain components at the nodal locations. Centrifugal loads were applied at the nodal location on an elemental basis. Each of five steady state and transient cases analyzed consisted of a unique set of thermal and centrifugal loads and reflected the required changes in material properties resulting from changes in the three dimensional temperature distribution.

Results of the airfoil strain-temperature analysis indicate that the maximum normal strain ranges calculated in the x, y, and z direction occur at different locations on the airfoil.* Magnitudes of these strain ranges (see Figure 1) are $\Delta\varepsilon_x = 0.0018$m/m, $\Delta\varepsilon_y = 0.0012$m/m, and $\Delta\varepsilon_z = 0.0016$m/m, respectively (Table 1). The complete strain-temperature cycle (peanut curves) corresponding to each of the above strain ranges is shown in Figure 4. In the case of $\Delta\varepsilon_y$ and $\Delta\varepsilon_z$, the maximum tensile strain occurs at or near the minimum temperature in the cycle and the maximum compressive strain at or near the maximum temperature in the cycle (i.e., TMF cycle I). For $\Delta\varepsilon_x$, on the other hand, the maximum tensile and compressive strains occur at an intermediate temperature (i.e., a "baseball" TMF cycle). For comparative purposes, results of a parallel analysis for D.S. Mar-M200+Hf, an anisotropic nickel base superalloy that is bill-of-material in advanced P&WA engines, are included in Table I. While $\Delta\varepsilon_z$ is larger for D.S. Mar-M200+Hf (0.0020m/m vs. 0.0016m/m) and $\Delta\varepsilon_x$ for $\gamma/\gamma'-\delta$ (0.0018m/m vs. 0.0014m/m), these calculated values indicate similar thermally-induced strain ranges for the two anisotropic alloys. Results of thermomechanical fatigue tests conducted on the D.S. $\gamma/\gamma'-\delta$ eutectic alloy with temperature strain cycles of the types identified above are discussed in section 4.

3.2 ROOT-PLATFORM ANALYSIS

The objective of the root platform analysis was to determine the magnitude and distribution of stress in the root and platform areas of the advanced, hollow eutectic turbine blade attachment illustrated in Figure 5, using a finite element method which accounts for the anisotropic elastic properties of the eutectic. In a separate section (Section 5.0) experimental root subcomponent tests are presented for comparison with the analytical results.

Because large load and stress gradients normally exist in turbine blade attachments, the accuracy of a finite element root stress analysis depends on the fineness of the elements used to represent the structure. The available core capacity of current generation computers limits the degree of refinement which can be achieved with a three dimensional analysis such as the previously described ASKA. A two-step approach, therefore, was used for the eutectic blade analysis. A three dimensional ASKA analysis of a coarse break-up was first performed to define the overall load distribution in the blade. Based on these

_____

*The specific positions on the airfoil at which these cycles are found are classified information, obtainable on request by persons having a confidential security clearance and a need to know.

results, a refined two dimensional analysis was performed to accurately cal-
culate local stresses in critical areas of the root.

To insure correct simulation of attachment stresses in the separate experimental
program, two root stress analyses were performed; one on the actual root-airfoil
configuration (Figure 5), and the other on the root configuration machined in
the end of the test block used for subcomponent testing (Figure 6). Load distri-
butions from the root-airfoil analyses were compared with the root subcomponent
analysis to determine the degree to which the experimental test simulated the
stresses developed in the blade root.

Shown in Figure 7b is a perspective view of the root model used for both the
blade and the test specimen 3D analyses. Included in this illustration are the
twenty nodes associated with a typical ASKA Hexc 20 element used to construct
the model. The mating disk-lug model is shown in Figure 7a. The elastic constants
for Waspaloy, a typical nickel base disk material, were used in calculation of
the lug displacements. Boundary conditions imposed on the mated root and disk-
lug are illustrated in Figure 8. The disk lug is fixed (no displacements permitted)
at the bottom, with only radial and axial displacements being permitted along the
centerplane of the lug.

For evaluation of stresses in the root subcomponent test specimen, a uniform
displacement was applied to the top surface shown in Figure 8. Stresses in
the actual blade attachment were calculated by application of calculated sub-
platform blade displacements to this same model. Calculating the subplatform
displacements was accomplished by the application of body forces (centrifugal
loads) to each element of the blade and platform model shown in Figure 9.

Based on results of an earlier study,[1] which indicated that the design limiting
properties of γ/γ'-δ may be intermediate temperature strength in shear applied
parallel to the solidification direction, primary attention in the analytical
study was focused on determination of radial (parallel to the blade axis) shear
stresses in the teeth. Shown in Figure 10 are local (concentrated) shear stress
levels determined from the ASKA (3D) analysis at various locations near the
top surface of each tooth. Comparison of results from the blade with results
from the test specimen indicates significant differences between local values
of shear stress. While some of this difference results from centrifugal loads
developed within the root, and not simulated by the application of a uniform
load to the neck of the test specimen, the major part of the difference
results from the fact that the centrifugal load is not distributed uniformly
in the blade neck. Shown in Figure 11 is a plot of displacement in the neck
of the blade at the location where a uniform displacement was assumed for cal-
culation of test specimen stresses. These data show a significant variation
of displacement (and hence stress) between the convex and concave sides of the
blade as well as along each side. This non-uniform distribution results from
the complex stress pattern which exists at the interface between the root and
the airfoil (Figure 12). Despite the substantial variation of localized stresses
along and among individual teeth seen in Figure 10, resultant average tooth
loads determined in the centrifugally loaded blade are relatively uniformly
distributed from side to side and among the teeth on each side (Figure 13).

As indicated above, a refined two dimensional finite element analysis was per-
formed on the blade root to more accurately define local stresses in critical
areas of the attachment. As shown in Figure 14, execution of the 2D analysis
involved application of boundary displacements calculated from the 3D analysis
to a refined two dimensional model of a mated root-half/disk lug pair. Unde-

flected and deflected 2D break-ups of this mated pair are shown in Figure 14, while tooth shear and tooth bending stresses determined in the deflected model are shown in Figure 15.

Examination of the results in Figure 15b indicates shear stresses significantly in excess of 386MPa (56 ksi) ultimate shear strength of the optimized γ/γ'-δ D.S. eutectic alloy at 760C (1400°F). This result must be interpreted in light of the fac that the two dimensional section analyzed was taken at the most highly stressed location of the root as defined by the 3D analysis; and that the effects of localized plastic deformation, which would tend to "seat" the attachment in the disk lug and spread the loading more uniformly across each tooth, are not accounted for in the ideally-elastic analysis. As discussed in section 5, experimental results indicate that the effects of localized inelastic stress relaxation are significant, so that measured failure loads were considerably in excess of those which would be predicted on the basis of results from the linear elastic analysis shown in Figures 10 and 15.

4.0 THERMOMECHANICAL FATIGUE EVALUATION

The objective of this evaluation was to determine the longitudinal and transverse thermomechanical fatigue (TMF) capability of $\gamma/\gamma'-\delta$ subjected to the types of strain-temperature cycles calculated for an advanced eutectic turbine blade (See Section 3.1). To achieve this objective, tests were conducted which involved the application of synchronized, independently programmed temperature and uniaxial mechanical strain cycles to D.S. eutectic fatigue test specimens. Details of the experimental program and test results are discussed in the following paragraphs.

4.1 EXPERIMENTAL DETAILS

The test specimen used for experimental evaluation of TMF properties was a tubular design incorporating internal ridges for direct measurement and programmed closed-loop feedback servocontrol of uniaxial longitudinal strain (Figure 16). While this specimen does not simulate possible multiaxial strains in the actual airfoil, previous experience has shown reasonably good correlation between test specimen and airfoil behavior. Synchronized temperature cycling was accomplished by infra-red temperature feedback control of an induction coupled heating apparatus. Temperature feedback also was used to electronically compensate the strain feedback signal for thermal expansion, which permitted direct measurement and servocontrol of true mechanical strain at all temperatures in the TMF cycle. All tests were conducted at a frequency of 0.017 Hz (1 minute per cycle) which provides strain rates on the same order as those experienced during transient engine operation. Additional details concerning the experimental technique may be found in Reference 2.

The Ni-20.1Cb-2.5Al-6Cr-0.06C* eutectic test material was processed in two forms for respective evaluation of TMF properties parallel and perpendicular to the solidification direction. Based on results reported from an earlier NASA sponsored alloy and structural optimization program,[1] processing conditions for both forms were selected to produce a fully lamellar (plane front solidified) microstructure.

Castings for longitudinal test specimens (stress axis parallel to the solidification direction) were processed in a previously described[1] water quench Bridgman furnace using a 1.9 cm (0.75 inch) diameter by $\approx$15 cm (6 inches) long recrystallized alumina crucible withdrawn parallel to the cylinder axis. Based on previous experience, a solidification rate of .64 cm (0.25 inch) per hour was used to produce the desired fully lamellar microstructure shown in Figure 17a. To minimize casting cycle time, only the central 5 cm (2 inches) of each bar was solidified at this rate, with the bottom and top ends being processed at rates between 1.2 cm (0.5 inch) and 2.5 cm (1 inch) per hour. Metallographic examination of longitudinal flats polished on the outside surface of each casting and on the cylindrical core machined from the center of each hollow TMF specimen blank was performed to verify the desired microstructural quality.

---

*Weight percent

9

Material for transverse TMF specimens (stress axis perpendicular to the solidification direction) was produced in a previously described [1] modified Bridgman furnace using conventional alumina shell molds having the hourglass shape shown in Figure 18a. The mid-section thickness of this casting was reduced to promote a higher thermal gradient for achievement of the desired fully lamellar microstructure with the applied freezing rate of 0.64cm (0.25 inch) per hour. As indicated in Figure 18b, a relatively large pour cup was attached to the top of this casting to add "thermal mass", which promotes higher gradients. As with the longitudinal castings, surface examination and sectioning of the specimen core were used to screen specimen blanks for microstructural quality. A typical microstructure produced by this process is shown in Figure 17b.

As shown in Figure 1, advanced hollow blade designs typically incorporate elaborate cooling schemes, involving numerous small cooling holes distributed over the blade surface, to reduce metal operating temperatures. To simulate the stress concentration caused by the presence of closely spaced holes on the leading edge of an advanced hollow eutectic blade, selected longitudinal tests were conducted on "showerhead" specimens which contained a simulated leading edge cooling hole pattern (Figure 19).

Results of a prior NASA sponsored coating program indicated that $\gamma/\gamma' - \delta$ will require total surface protection for application in a gas turbine environment. [3] To simulate engine application, all specimens were coated on the O.D. with $\approx 64\mu m$ (2.5 mils) of a vapor deposited NiCrAlY overlay coating* plus $\approx 6\mu m$ (0.25 mil) Pt, which was identified as the optimum coating system for $\gamma/\gamma' - \delta$ on the previous NASA Program. [3] A typical photomicrograph of this coating in the thermally exposed condition is shown in Figure 20.

The experimental program involved a total of eighteen TMF tests. Twelve of these tests were conducted on longitudinal specimens and six on transverse specimens. Of the twelve longitudinal specimens, six were smooth and six contained the showerhead hole pattern shown in Figure 19. While the primary objective of the testing was to determine cycles to failure (defined as 50% load drop) as a function of applied mechanical strain range, crack initiation data also were obtained for most tests by microscopic examination of surface replicas taken periodically during testing. As discussed in subsequent paragraphs, emphasis was placed on evaluation of TMF behavior with the engine strain-temperature relationships shown in Figure 4. However, a limited number of Cycle I tests (maximum tension applied at minimum temperature, maximum compression applied at maximum temperature, see Figure 21) also were conducted to determine the influence of cycle shape on longitudinal and transverse TMF properties.

---

*PWA 267 specification, nominal composition Ni-18Cr-12Al-0.3Y

4.2 TEST RESULTS

4.2.1 Smooth Longitudinal

Five of the six smooth longitudinal tests conducted in this part of the program involved testing with the spanwise temperature-strain phase relationship shown in Figure 4c. Two of these five tests were conducted with the calculated strain-temperature curve expanded symmetrically about the mean strain to obtain data for an S-N curve, as illustrated in Figure 22. Results of these tests (Table II), plotted as open circles in Figure 23a, indicate that smooth TMF life will be substantially in excess of 10^4 cycles at the maximum spanwise strain range of 0.0016m/m calculated for the advanced blade.

Because the trend for some advanced engines is toward higher operating temperatures, a second set of three smooth longitudinal tests was conducted to determine the influence of increased peak cycle temperature on smooth longitudinal TMF behavior. For this series of tests, both the strain and temperature ranges of the spanwise engine cycle were expanded, again in such a way as to maintain the cycle shape shown in Figure 4c. Results of these tests, plotted as half-shaded circles in Figure 23a, indicate about a 75% reduction of fatigue life as a result of the increased temperature range. Despite this life debit, the higher cycle temperature smooth specimen results continue to be well above the requirements for the advanced blade analyzed.

To investigate the influence of cycle shape on smooth TMF life, a single test was conducted with Cycle I loading (Figure 21). Results of this test, plotted as a shaded circle in Figure 23a, indicate a substantial influence of cycle shape on life. However, extrapolation of the Cycle I data parallel to the S-N curves developed for the engine cycle indicates that the smooth longitudinal Cycle I TMF capability of the eutectic continues to be in excess of advanced hollow blade requirements.

4.2.2 Longitudinal Showerhead

Longitudinal showerhead TMF behavior was evaluated with the same three types of cycles used for evaluation of smooth longitudinal behavior. As shown in Table III and in Figure 23b, the life differences resulting from variations of cycle shape and temperature range were smaller than life differences found on smooth specimens. In particular, the large life debit found with Cycle I loading of smooth specimens was not found with Cycle I loading of showerhead specimens. While the showerhead results generally tended to be lower than results obtained on smooth specimens, extrapolation of the showerhead data indicates a cyclic life well beyond 10^4 cycles at the calculated maximum engine spanwise strain range of 0.0016m/m.

11

Because of differences observed in load drop behavior for the smooth and showerhead specimens, the showerhead data were examined in terms of 5% load drop (a more conservative failure criterion) as well as the more commonly used 50% load drop failure criterion. Comparison of the typical showerhead load drop curve (Figure 24b) with the smooth load range curve shown in Figure 24a reveals that, whereas the smooth specimen load range typically fell off abruptly very near the termination of testing, the showerhead load range curves typically tended to drop much more gradually. Thus, while the 50% and the more conservative 5% load drop failure criterion are virtually identical for the smooth specimens, a significant difference exists between the two criteria for the showerhead specimens. Despite this difference, the 5% load drop showerhead results plotted in Figure 25 continue to indicate that longitudinal showerhead fatigue properties are in excess of design requirements for the advanced blade analyzed.

4.2.3 Transverse

Transverse thermomechanical fatigue tests were conducted primarily with the maximum chordwise engine cycle shown in Figure 4a. As with longitudinal tests, three sets of transverse test conditions were investigated. As illustrated in Figure 26, smooth transverse load drop behavior with all of these cycles was similar to smooth longitudinal behavior, so that transverse test results were analyzed only in terms of the 50% load drop failure criterion.

The first of the three sets of transverse test conditions involved testing with the cycle shown in Figure 4a expanded about the mean strain to develop an S-N curve. Results of three tests conducted with these conditions (Table IV), plotted as open diamonds in Figure 23c, indicate that the smooth transverse TMF properties of the eutectic are well above requirements for the particular advanced hollow blade analyzed.

The second set of transverse test conditions involved expansion of the chordwise engine cycle about the mean temperature. The result of a single test conducted with an expanded temperature range of 343-1038C (650-1900°F) is plotted as a half-shaded diamond in Figure 23c. While increasing the engine cycle temperature range reduces the transverse TMF capability, an extrapolation of the available data parallel to the lower temperature engine cycle curve indicates a life well above 10,000 cycles at the maximum calculated chordwise strain range of 0.0018m/m.

The result of a single transverse test conducted with Cycle I loading, which is similar to the engine cycle shown in Figure 4b, is plotted as a shaded diamond in Figure 23c. As with smooth longitudinal tests, Cycle I loading causes a very large debit of smooth transverse TMF properties. Based on the previously discussed stress analysis, which indicates a chordwise Cycle I strain range in the order of 0.0012m/m (Figure 4b), and assuming that the Cycle I result can be extrapolated parallel to the engine cycle data, chordwise thermal fatigue life should be above 10^4 cycles in areas of the blade which experience Cycle I loading (see Figure 23c). It is suggested that additional data should be generated to confirm this prediction.

Because of the relatively large size of the elements used for the advanced hollow blade stress analysis (Figure 3), it was not possible to accurately determine whether or not the location of the maximum chordwise strain range might be coincident with one of the cooling holes which are distributed over the surface of the advanced blade analyzed (Figure 1). A single transverse test therefore was conducted using the 471-910C (880-1670°F) chordwise engine cycle on a specimen containing two isolated cooling holes which were perpendicular to the load axis and were centered in diametrically opposite locations along the gage section. This specimen was cycled to 1059 cycles at the maximum calculated chordwise engine strain range of 0.0018m/m, with no cracks being detected. It was then uploaded and cycled to failure at a strain range of 0.0037m/m. Results of this test, shown as open diamonds with flags in Figure 23c, indicate about an order of magnitude life debit with respect to a smooth test conducted with identical test conditions. Assuming that this data can be extrapolated parallel to the smooth data extrapolation, a life above 10^4 cycles is predicted for th possible case where the maximum chordwise strain range occurs at a oling hole location.

Thus, depending on whether or not this situation occurs, either cooling hole associated transverse failure or chordwise Cycle I loading appear to represent the life limiting types of TMF cycling for the advanced hollow eutectic blade analyzed, with the more conservative of these two predictions (i.e., hole associated failure) indicating a blade life on the order of 14,000 cycles. As with the Cycle I lifetime prediction, additional transverse TMF data on specimens containing simulated cooling holes should be generated to confirm this prediction.

4.3 DISCUSSION

4.3.1 Smooth Longitudinal Behavior

Two separate and distinct failure modes were observed with the different test conditions applied to smooth longitudinal TMF specimens. The first of these was coating-initiated fatigue cracking, which was the dominant failure mode associated with the 504-938C (940-1720°F) engine cycle and 427-1038C (800-1900°F) Cycle I test conditions. Examples of this crack initiation mode are illustrated in Figure 27. The second mode involved failure from thermal fatigue cracks initiated at internal extensometer ridges. This failure mode, which was dominant with the 427-1038C (800-1900°F) engine cycle, is illustrated in Figure 28a. As shown in Figure 28b, ridge associated crack initiation also was found in the 504-938C (940-1720°F) engine cycle specimens which failed from coating cracks.

Comparison of the 504-938C (940-1720°F) and 427-1038C (800 - 1900 °F) engine cycle crack initiation data (Table II) indicates that increasing the temperature range does not have a deleterious influence on coating crack initiation life at the 0.0056m/m strain range*. While the comparison is not as clear at the 0.0070m/m strain range, it appears that the change in failure mode from coating to ridge initiated failure must result from the influence of temperature on substrate crack initiation and/or propagation rate. Thus, it appears that ridge associated cracks

---

*It must be emphasized that this statement relates specifically to experimental observations for the engine cycle shown in Figure 4c, and cannot be extended by implication to other cycle shapes.

13

initiated in all of the smooth longitudinal engine cycle specimens, but that ridge associated initation and/or propagation was sufficiently slower at the lower temperature to allow time for initiation and propagation of coating cracks. The reason for the occurrence of ridge initiation, which is not frequently found in conventional and D.S. superalloy specimens of the same design, is not clear at the present time.

The large life debit resulting from Cycle I loading is attributed to the influence of cycle shape on coating crack initiation. As indicated in Table I , the smooth longitudinal Cycle I specimen failed from coating initiated cracks at a life well below the number of cycles required to initiate coating cracks with either of the engine cycles studied. The specific factors thought to be responsible for accelerated Cycle I coating crack initiation are discussed below.

Major factors which influence coating crack initiation are the magnitude of the maximum tensile strain in the coating and the temperature at which the maximum tensile strain occurs.[4] These factors are particularly important if the coating tensile strain peaks at low temperatures where coating ductility can be relatively low. Thus, as shown in Figure 29, Cycle I loading can be more damaging to the coating than either of the two engine cycles because of the lower temperature at which the maximum tensile strain occurs.

The magnitude of the maximum tensile strain experienced by the coating during TMF cycling is influenced by high temperature stress relaxation of both the coating and the substrate, as well as by thermal expansion mismatch strains between the coating and the substrate. An example of substrate stress relaxation, or "shakedown", is illustrated in Figure 30 for specimen A76-103. Shown in Figure 30a is the measured change of length which occurred during TMF cycling of this specimen. The corresponding shift for mean strain and stress are shown in Figure 30b and 30c, while the upward shift of the effective strain temperature cycle is shown in Figure 30d. The load shakedown measured for each of the three cycles investigated on smooth longitudinal specimens is compared in Figure 31. It is apparent that Cycle I loading causes a significantly greater increase of tensile strain than either of the engine cycles. As was the case with all of the tests conducted on the program, the magnitude of the applied strains was such that no cyclic plastic strain was experienced by the specimen.

Compounding the influence of Cycle I substrate shakedown on coating crack initiation are differential coating relaxation and thermal expansion mismatch strains. As discussed in more detail in Reference 4, differential high temperature relaxation of compressive stresses in the coating can significantly increase the maximum coating tensile strain, as illustated schematically in Figure 32. Also illustrated in this figure is the potential influence of thermal expansion mismatch strain, which can add as much as 0.0019m/m to the 427-1038C (800-1900°F) coating strain range for the γ/γ' - δ - NiCrAlY/Pt system.*   Thus, through the combined influences of basic cycle shape, substrate and coating stress relaxation, and thermal expansion mismatch strain, the peak tensile strain experienced by the coating could have achieved levels as high as 0.0075m/m at 427C (800°F)

_____

*T.E. Strangman , unpublished research, Pratt & Whitney Aircraft Group, Commerical Products Division, United Technologies Corporation.

on the 427-1038C (800-1900°F) Cycle I specimen tested at a 0.0056m/m strain range. As shown in Figure 32, this level of tensile strain could approach the coating fracture strain at 427C (800°F), although additional coating ductility data are required to confirm this possibility. The high level of low temperature coating tensile strain experienced in Cycle I loading also could cause significant cyclic coating plasticity, which also would tend to reduce coating fatigue life and contribute to the early coating crack initiation observed in the Cycle I test.

Thus it is concluded that the relatively low smooth longitudinal fatigue life experienced with Cycle I thermomechanical fatigue results from high peak tensile strain experienced by the coating at low temperatures, which causes early initiation and enhanced propagation of coating cracks. While additional Cycle I data would be desirable to confirm the extrapolation shown in Figure 23a, it should be reiterated that the longitudinal smooth thermomechanical fatigue behavior of the eutectic does not appear to be life limiting for the particular advanced blade analyzed.

4.3.2 Longitudinal Showerhead Behavior

As expected, examination of tested showerhead specimens showed crack initiation occurring exclusively at the simulated cooling holes (Figure 33). While initiation occurred at all locations along the hole barrel (Figure 34), a general trend was observed for preferential initiation at the entry and exit ends of the hole where the hole-specimen surface interface geometry forms an acute angle in a plane normal to the stress axis (Figure 34a & b). By coincidence, this location on the hole barrel was approximately co-planar for successive holes on the inner diameter (I.D.) and outer diameter (O.D.) surface, as illustrated in Figure 35.

The reduced TMF properties of showerhead specimens as compared to smooth specimens and the smaller influence of cycle shape on life are attributed to accelerated crack initiation at cooling holes, Tables II and III. This observation is consistent with the observations made in an earlier section concerning the role of crack initiation as a causal factor for variations of life seen with different cycle shapes applied to smooth specimens. Apparently the stress concentration provided by the presence of cooling holes provides a sufficient driving force for crack initiation to eliminate large differences caused by the influence of cycle shape on coating crack initiation. It is interesting to note in this connection that the smooth longitudinal Cycle I data point, where early crack initiation was thought to occur as a result of high peak coating tensile strains occurring at low temperatures, falls within the scatter band for the showerhead 5% load drop results (Figure 25).

4.3.3 Transverse Behavior

Transverse TMF specimen behavior was more difficult to analyze than longitudinal specimen behavior, primarily because it was difficult to identify the crack initiation site(s) on transverse fracture surfaces. The importance of initiation as a major component of transverse TMF life is indicated by comparison of results obtained with identical test conditions on the smooth and simulated cooling hole specimens (compare specimen E576A and E600 A, Table IV), where life is reduced about an order of magnitude

15

by hole-associated crack initiation. Even on the cooling hole specimen, where initiation was known, based on visual observations made through a travelling telescope, to occur at the hole, no clear evidence of initiation was visible on the fracture surface (Figure 36).

Based on relatively subtle differences of oxide coloration observed on transverse TMF fracture surfaces, it is hypothesized that initiation generally tended to occur on the uncoated I.D. surface in locations where the aligned structure was tangent to the inside wall (Figure 37). Corrollary evidence for initiation in this area was found in the form of secondary cracks found on the I.D. of most transverse specimens (Figure 38). It appears that preferential oxidation of grain boundaries and Ni_3Cb lamellae (Figure 39) may be involved with the transverse initiation process. It is probable that the reduced life found with increased cycle temperature is associated with oxidation effects. The depth of selective Ni_3Cb oxidation on specimen E582C (Figure 40), on the order of $200\mu m$ (8 mils), was much greater than was found on any of the other transverse specimens (reference Figure 38 and 39 as a typical range). This observation reinforces previous conclusions concerning the need for total surface protection in turbine blade application of γ/γ' - δ. No secondary coating cracks were found on any of the transverse TMF specimens, which also tends to support the I.D. initiation hypothesis.

Concerning the large transverse life debit seen with Cycle I loading, two contributory factors can be proposed. First, this specimen was found to be slightly δ (Ni_3Cb) dendritic, with failure occurring at a δ dendrite (Figure 41). Evidence for preferential oxidation of other similarly located δ dendrites was found on the I.D. surface of the Cycle I specimen (Figure 42).

The second factor thought to be associated with accelerated failure of the Cycle I specimen was the significant shakedown which occurred very early in testing (Figure 43). Large shakedown was not found on the chordwise engine cycle transverse specimens because both peak tensile and compressive strains occurred in a lower temperature range (Figure 4a). The large tensile stresses experienced by the Cycle I specimen after shakedown were close to the yield stress at the minimum cycle temperature, meaning that this specimen probably experienced significant cyclic plasticity. For a material with limited intrinsic ductility, cyclic plasticity would tend to severely reduce cyclic life.

Thus, it is concluded that the low transverse TMF life of the Cycle I specimen resulted from the combined effects of slightly deviant microstructure and excessive shakedown which caused cyclic plasticity associated with high peak tensile strains applied at low temperatures. It should be reiterated that this test was conducted at three times the maximum calculated chordwise Cycle I strain range, and that, based on the extrapolation shown in Figure 23c, the chordwise Cycle I thermal fatigue properties of the eutectic should be adequate for the particular advanced hollow blade analyzed. However, additional TMF tests to confirm these findings should be conducted.

5.0 ROOT SUBCOMPONENT TESTING

The objective of this study was to experimentally determine the capability of γ/γ' - δ to meet advanced hollow blade root attachment requirements. As described below, the approach taken to achieve this objective involved creep, fatigue, and tensile pull-out tests conducted on an advanced hollow root attachment configuration machined into the end of a directionally solidified eutectic test block (Figure 6).

5.1 EXPERIMENTAL DETAILS

The Ni-20.1Cb-2.5Al-6.0Cr-0.06C eutectic test material evaluated in this program was produced using conventional alumina shell molds which provided castings having the configuration shown in Figure 44. Directional solidification parallel to the root axis was accomplished in the previously mentioned radiation cooled modified Bridgman furnace at a rate of 0.64 cm (0.25 inch) per hour. Metallographic examination of the casting surface and of tested specimens indicated a fully lamellar microstructure in the lower part of the castings from which the fir-tree configuration was machined (Figure 44).

Prior to fabrication of test specimens, machining trials were conducted to determine the optimum parameters for machining of the fir tree configuration in D.S. γ/γ' - δ. Results of these trials indicated the procedure specified in Table V as suitable for the root machining process.

To simulate application of γ/γ' - δ with full surface protection, root subcomponent specimens were overlay coated with $\approx$ 64 μm (2.5 mils) of NiCrAlY. To obtain a uniform coating thickness and assure good fit-up between the root and broach block, the uncoated root form was ground 64 μm (2.5 mils) undersize and $\approx$ 128 μm (5 mils) of coating was applied to the as-ground root. The coated root was then finish machined to print, leaving a $\approx$ 64 μm (2.5 mils) NiCrAlY coating envelope on the eutectic substrate.

5.2 ROOT PULL-OUT TESTS

Based on the previously discussed root stress analysis (Section 3.2), which indicated maximum concentrated shear stresses as high as 923 MPa (134 ksi) in the root (Figure 15), as compared to a 760C (1400°F) ultimate shear strength of 386 MPa (56 ksi) for carbon modified γ/γ' - δ,[1] it was expected that the root subcomponent specimens might fail at loads significantly below the maximum blade pull of 224kN (50,386 lb.). Results of triplicate 760C (1400°F) pull-out tests (Table VI) indicate that the subcomponent pull-out load is more on the order of 356kN (80,000 lb.), with failure occurring in a tooth shear mode (Figure 45). The fully distributed shear stresses indicated in Table VI, which were calculated using the measured tooth shear area, are very close to the 386MPa (56 ksi) ultimate shear strength at the 760C (1400°F) test temperature, indicating that localized plastic deformation of the teeth fully relaxes the high concentrated stresses calculated in the linear elastic stress analysis. Based on the above results, it is concluded that the short term load carrying capabilities of the eutectic is adequate for advanced blade attachment requirements.

5.3 ROOT SUBCOMPONENT LOW CYCLE FATIGUE

Some difficulty was encountered in efforts to conduct low cycle fatigue tests on the root subcomponent specimen shown in Figure 6. This specimen consisted of a fir-tree root configuration machined at one end of the test block and a threaded hole for load-train attachments tapped at the other end. The first two attempts to conduct 760C (1400°F) LCF tests with a load range of 0-178kN (0-40,000 lb) (Table VII) resulted in splitting of the eutectic grip block at the load-train attachment hole, (Figure 46a). The poor transverse properties of the eutectic which resulted in this failure were attributed to the highly degenerate structure in the massive block which contained the load-train attachment hole (Figure 46b). To prevent these failures in the remaining specimens, the thick grip sections containing the attachment hole were turned down to accept a shrink-fit superalloy collar (Figure 47). This approach prevented splitting of the eutectic grips during subsequent fatigue tests.

Using the shrink-fit collar collar approach, a specimen was fatigue tested for 11,140 cycles at 760C (1400°F), 0-178kN (0-40,000 lb.), at which point a crack was detected in the eutectic specimen at the root of the bottom tooth serration (Figure 48). Attempts to conduct a test at 0-222kN (0-50,000 lb.) load (nominal blade pull) were not successful because of failure of the B-1900 + Hf superalloy broach block (simulated disk slot) after 471 cycles (Figure 49). The first attempt to conduct the 0-222kN (0-50,000 lb.) test was made using a broach block that had accumulated approximately 12,000 cycles during the 0-178kN (0-40,000 lb.) test. The second attempt, made with a broach block that had not previously been used for fatigue testing, ran 2964 cycles before failure of the broach block. In both cases of broach block failure, the bottom tooth of the eutectic specimen was damaged when the block failed (Figure 50) so that further testing of the specimen was not possible. Since the eutectic specimen did not fail prior to the superalloy broach block failure, the LCF life of the $\gamma/\gamma'-\delta$ root configuration tested must be greater than 2964 cycles at 760C (1400°F) and the maximum blade pull of 222kN (50,000 lb.).

Based on the eutectic root fatigue results, it is concluded that the root LCF properties of $\gamma/\gamma'-\delta$ may be marginal for the advanced hollow blade analyzed, with 760C (1400°F) root fatigue life being above 3000 cycles at the nominal maximum blade pull. However, additional testing would be required to define the actual root LCF life. A desired goal for LCF capability is usually 5000 to 10,000 cycles at maximum conditions. Based on the crack found in the 0-178kN (0-40,000 lb.) specimen, it appears that the root failure mode may involve transverse cracking at the base of the first serration rather than tooth shear failure as in direct pull-out.

5.4 ROOT CREEP TESTS

Results of sustained load (creep) pull-out tests on the D.S. eutectic root subcomponent specimens are presented in Table VIII. As with the previously discussed short-term pull-out tests, failure occurred in a tooth shear mode identical to that shown in Figure 45. When analyzed on a Larson-Miller diagram in terms of fully distributed shear stresses, Figure 51, the root subcomponent creep test results are consistent with laboratory shear creep data generated in a previous alloy development program.

18

The creep results presented in Table VIII indicate that the 760C (1400°F) creep life of the attachment analyzed is less than 5 hours at the nominal maximum blade pull of 222kN (50,000 lb.). A 60C (100°F) decrease of attachment temperature increases the attachment life, but not sufficiently for an advanced blade application. Based on the Larson-Miller curve shown in Figure 51, it would be necessary to decrease the attachment temperature to ≈600C (≈1100°F), or the shear stress level to ≈117MPa (17 ksi) (approximately 50% stress reduction) to increase attachment creep life beyond 10,000 hours, not accounting for possible safety factors. While the lower attachment temperature is not unreasonable in terms of some current generation designs, it is significantly below the anticipated operating temperature of advanced attachments. Stress reductions of the required magnitude also are considered to be beyond the scope of available attachment design techniques. It, therefore, must be concluded that the sustained load attachment capability of $\gamma/\gamma'-\delta$ is not adequate for advanced hollow turbine blade applications. A possible approach to solution of this problem would involve the development of a fabricated blade incorporating a D.S. eutectic airfoil bonded to a superalloy root. Such a development is within reach of current bonding technology.

6.0 CONCLUSIONS

The objective of this program was to evaluate the capability of $\gamma/\gamma' - \delta$ to sustain the airfoil thermal fatigue and root attachment loads imposed in advanced, hollow, high work eutectic turbine blades. Simulated airfoil thermal fatigue and root subcomponent tensile, creep, and low cycle fatigue tests were conducted to achieve this objective. Airfoil and root platform stress analyses were conducted to determine appropriate test conditions for the experimental program.

Based on results of longitudinal TMF tests conducted on smooth hollow specimens and on hollow specimens containing a simulated leading edge cooling hole pattern, it is concluded that the longitudinal TMF capability of the eutectic is adequate for advanced hollow airfoil applications. The minimum longitudinal properties, which were obtained on the simulated cooling hole specimens, indicated the strain range for 10^4 cycle life to be greater than 0.0025m/m, which is more than 50% above the calculated maximum spanwise airfoil strain range of 0.0016m/m. Transverse TMF properties, while somewhat lower than longitudinal properties, still appear to be adequate for the particular advanced blade analyzed. The life limiting transverse results were obtained on a transverse specimen containing simulated cooling holes. Based on these rather limited extrapolated results a thermal fatigue life of 14,000 cycles is predicted for the particular advanced hollow blade analyzed.

Based on results of root subcomponent tests, it is concluded that the sustained load (creep) properties of the eutectic in shear parallel to the solidification direction represent the life-limiting design property of $\gamma/\gamma' - \delta$. Short time root subcomponent pull-out tests indicated an ultimate load carrying capability 60% above the maximum pull for the particular attachment analyzed. Root LCF properties may be marginal, while root creep lives are not adequate for an advanced blade application. At the maximum blade pull of 222kN (50,000 lb.), root subcomponent pull-out lives on the order of 4-20 hours were measured in the anticipated operating temperature range of 760 to 700C (1400 to 1300°F), with failure occurring by a tooth shear mode. Based on the observation that neither reduced root operating temperature nor lower stress root designs could provide a large enough root creep life improvement, it is concluded that application of $\gamma/\gamma' - \delta$ as an advanced turbine blade material will require the development of a fabricated blade incorporating a D.S. eutectic airfoil bonded to a superalloy root. The development of such a blade is considered to be within the reach of current bonding technology.

7.0 REFERENCES

1. K.D. Sheffler, R.H. Barkalow, J.J. Jackson, and A. Yuen, "Alloy and Structural Optimization of a Directionally Solidified Lamellar Eutectic Alloy", NASA CR-135000, May 1976.

2. S.W. Hopkins, "Low Cycle Thermal Mechanical Fatigue Testing", ASTM Symposium of Thermal Fatigue of Materials and Components, New Orleans, La., 1975, ASTM STP 612 in Press.

3. E.J. Felten, T.E. Strangman, and N.E. Ulion, "Coatings for Directional Eutectics", NASA CR-134735, October 1974.

4. G.R. Leverant, T.E. Strangman, and B.S. Langer, "Parameters Controlling the Thermal Fatigue Properties of Conventionally Cast and Directionally Solidified Turbine Alloys", Superalloys: Metallurgy and Manufacture, B.H. Kear, et.al. Ed., Claitor's, Baton Rouge, La., 1976, p. 285.

TABLE I

Maximum Thermal Fatigue Strains Determined
From 3D Finite Element Analysis

		Direction (Reference Figure 1)		
		x	y	z
Maximum Strain Range (m/m)	D.S. Eutectic	0.0018	0.0012	0.0016
	D.S. Mar-M200+Hf	0.0014	-	0.0020

TABLE II

Results of Longitudinal Thermomechanical Fatigue Tests Conducted on Smooth γ/γ' - δ D.S. Eutectic
TMF Specimens Coated on the O.D. with ≈ 64μm (2.5 mils) NiCrAlY + ≈ 6μm (0.25 mil) Pt

Specimen Number	Strain Range m/m	Minimum Temperature		Maximum Temperature		Cycle[1] Shape	(2) Cycles to First Surface Indication	Cycles to 50% Load Drop	Comments
		°C	°F	°C	°F				
A76-103	0.0056	504	940	938	1720	S.E.C.	1527 < i < 2555	5224	Failed from coating crack, secondary cracks found at extensometer ridges
A76-216	0.0070	504	940	938	1720	S.E.C.	300 < i < 1260	1820	Failed from coating crack, secondary cracks found at extensometer ridges and on inside diameter of gage section
A75-813	0.0056	427	800	1038	1900	S.E.C.	Not detected	1938	Failed at extensometer ridge, no coating cracks detected
A76-120	0.0056	427	800	1038	1900	S.E.C.	Not detected	2220	Failed from extensometer ridge, no coating cracks detected
A76-171	0.0070	427	800	1038	1900	S.E.C.	261 < i < 562	562	Failed from extensometer ridge, secondary coating cracks observed
A76-211	0.0056	427	800	1038	1900	Cycle I	i < 239	239	Failed from coating crack

(1) S.E. C. = Spanwise Engine Cycle (See Figure 4c)

Cycle I - See Figure 21

(2) As-determined by microscopic examination of surface replicas

TABLE III

Results of Longitudinal Thermomechanical Fatigue Tests Conducted on Showerhead γ/γ' - δ D.S. Eutectic TMF Specimens Coated on the O.D. with $\approx$ 64μm (2.5 mils) NiCrAlY+$\approx$ 6μm (0.25 mil) Pt

Specimen Number	Strain Range m/m	Minimum Temperature °C	°F	Maximum Temperature °C	°F	Cycle[1] Shape	Cycles to First[2] Surface Indication	Cycles to 5% Load Drop	Cycles to 50% Load Drop
A76-130	0.0056	504	940	938	1720	S.E.C.	i < 109	250	351
A76-122	0.0040	504	940	938	1720	S.E.C.	i < 200	320	795
A76-207	0.0034	504	940	938	1720	S.E.C.	i < 1329	4600	5175
A76-124	0.0028	504	940	938	1720	S.E.C.	i < 2565	4200	8545
A76-214	0.0040	427	800	1038	1900	S.E.C.	576 < i < 876	1000	2520
A76-128	0.0040	427	800	1038	1900	Cycle I	i < 101	450	592

(1) S.E.C. = Spanwise Engine Cycle - See Figure 4c

Cycle I - See Figure 21

(2) As-determined by microscopic examination of surface replicas

24

TABLE IV

Results of Transverse Thermomechanical Fatigue Tests Conducted on $\gamma/\gamma' - \delta$
D.S. Eutectic TMF Specimens Coated on the O.D. with $\approx$ 64μm (2.5 mils) NiCrAlY + $\approx$ 6μm (0.25 mil) Pt

Specimen Number	Strain Range m/m	Minimum Temperature °C	°F	Maximum Temperature °C	°F	Cycle [1] Shape	Cycles to First Surface Indication	Cycles to 50% Load Drop	Comments
E582B[2]	0.0045	471	880	910	1670	C.E.C.	None detected	720	Failed in threads, no coating cracks found on unfailed gage section
E576A[2]	0.0037	471	880	910	1670	C.E.C.	821 < i < 1075	1857	
E579B[2]	0.0027	471	880	910	1670	C.E.C.	15,000 < i	>15,000	Test discontinued, no indications
E582C[2]	0.0037	343	650	1038	1900	C.E.C.	-	360	Not replicated prior to failure
E580C[2]	0.0037	427	800	1038	1900	Cycle I	-	37	Not replicated prior to failure
E600 A-I[3]	0.0018	471	880	910	1670	C.E.C.	None detected	>1059	Cycling terminated-specimen uploaded, see test E600 A-II
E600 A-II[3]	0.0037	471	880	910	1670	C.E.C.	-	188	Uploaded from 0.0018m/m - see specimen E600 A-I for prior cycling history, not replicated prior to failure

(1) C.E.C.= Chordwise Engine Cycle - see Figure 4a

  Cycle I - See Figure 21

(2) Smooth Specimen

(3) Simulated Cooling Hole Test

TABLE V

General Specification for Grinding Procedures for
Machining of γ/γ' - δ Eutectic Turbine Blade Roots

1. Rough grind root section to a machining envelope of +0.010" over finished print dimensions tangent to the root tip serrations. Use: 38A-(46 to 60)-I or J-8V7 or equivalent 7" diameter x 1" wide wheel. Remove 0.001"-0.002" per pass at wheel speed of 3600 rpm, flood coolant - soluble oil and water.

2. Rough grind end faces of root to +0.010" over finish per as above (see No. 1). Finish grind root end faces removing a maximum of 0.0005" per pass with 2 to 3 spark-out passes.

3. Single point form grind a root grinding wheel to finished print dimensions using a diaform type dresser. Use: 38A-(60 to 70)-I or J8V7 or equivalent 7" diameter X 1" wide wheel.

4. Rough grind root serrations to +0.010" over finished print dimensions with wheel from No. 3 above, redress as required. Use a plunge cut and hand feed to remove 0.001" to 0.002" per cut. Wheel speed: 3600 rpm, flood coolant, soluble oil and water.

5. Finish grind root serrations to finished print dimensions removing a maximum of 0.0005" per cut using same parameters as No. 4 above. Complete operation with 2 to 3 spark-out passes using newly-dressed wheel.

TABLE VI

Results of 760C (1400°F) Root Subcomponent Pull-Out Tests

Specimen Number	Pull Out Load		Fully Distributed Tooth Shear Stress	
	kN	Pounds	MPa	ksi
E596	368	82,750	401	58.2
E588	375	84,250	391	56.7
E597	359	80,750	400	58.0

TABLE VII

Results of 760C (1400°F) Root Subcomponent LCF Tests

(Cycled from Zero Load to Indicated Maximum Load)

Specimen Number	Maximum Load		Cycles To Failure	Comments
	kN	Lb		
E584	178	40,000	487	Failure of eutectic at load-train attachment hole.
E583	178	40,000	593	Failure of eutectic at load-train attachment hole.
E577	178	40,000	11,140	Crack detected, test terminated.
E578	222	50,000	471	Failure of superalloy simulated disk slot.
E592	222	50,000	2,964	Failure of superalloy simulated disk slot.

TABLE VIII

Results of Sustained Load Root Subcomponent Pull-Out Tests

Specimen Number	Applied Load		Test Temperature		Fully Distributed Tooth Shear Stress		Life, Hr.
	kN	Lb	°C	°F	MPa	ksi	
E545	267	60,000	760	1400	291	42.2	0.17
E589	222	50,000	760	1400	232	33.7	4.4
E586	178	40,000	760	1400	192	27.8	39.5
E585	222	50,000	700	1300	247	35.9	20.5
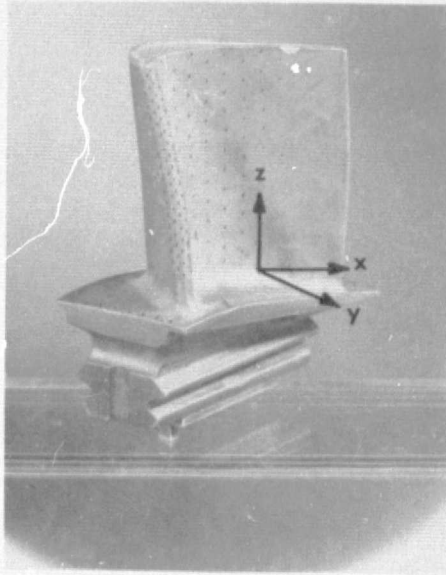
Figure 1 Advanced turbine blade being modeled for evaluation of $\gamma/\gamma'-\delta$ thermal fatigue performance capabilities. Axes indicate co-ordinate system employed for finite element analysis
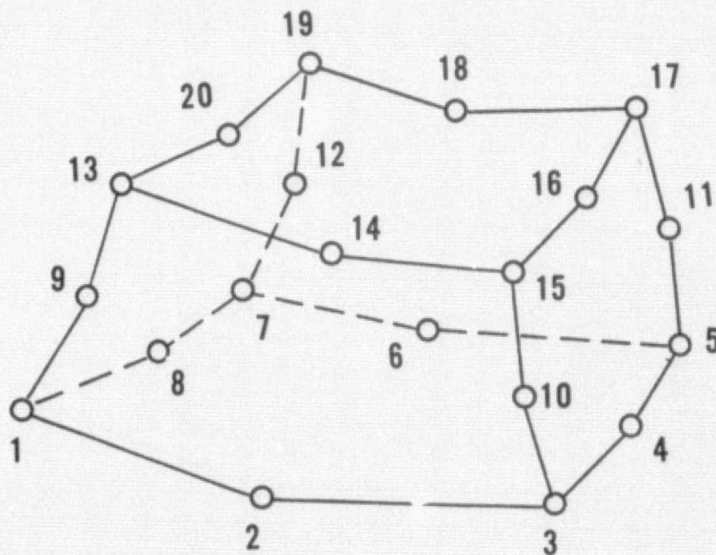
Figure 2 Typical ASKA (Automated System for Kinematic Analysis) Hexc twenty element
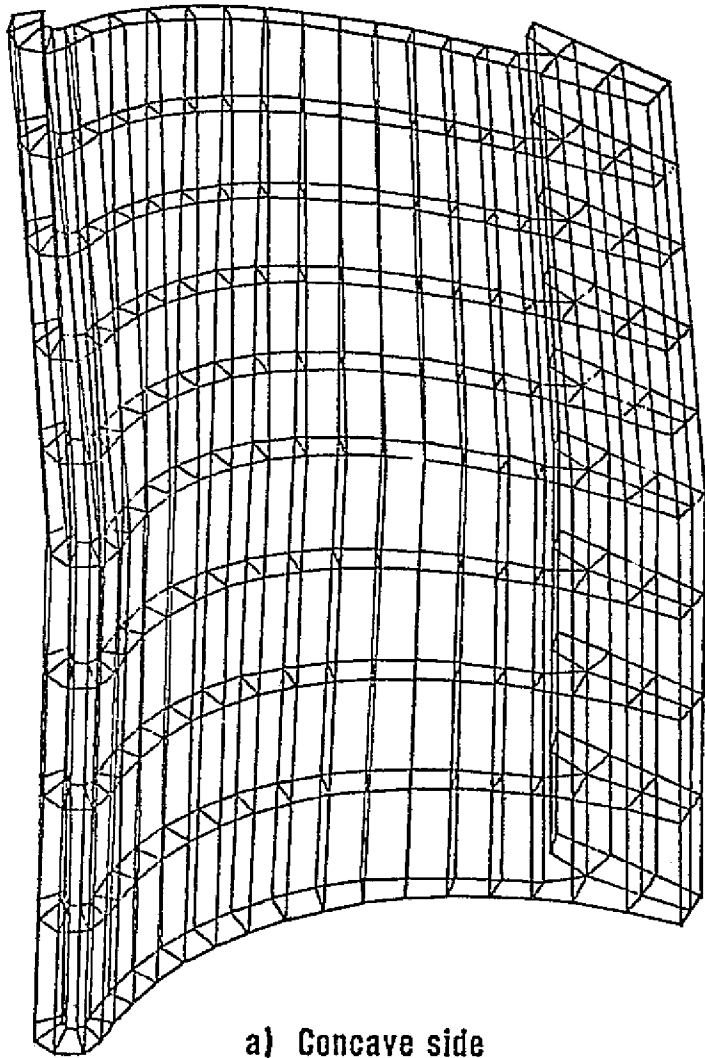
a) Concave side
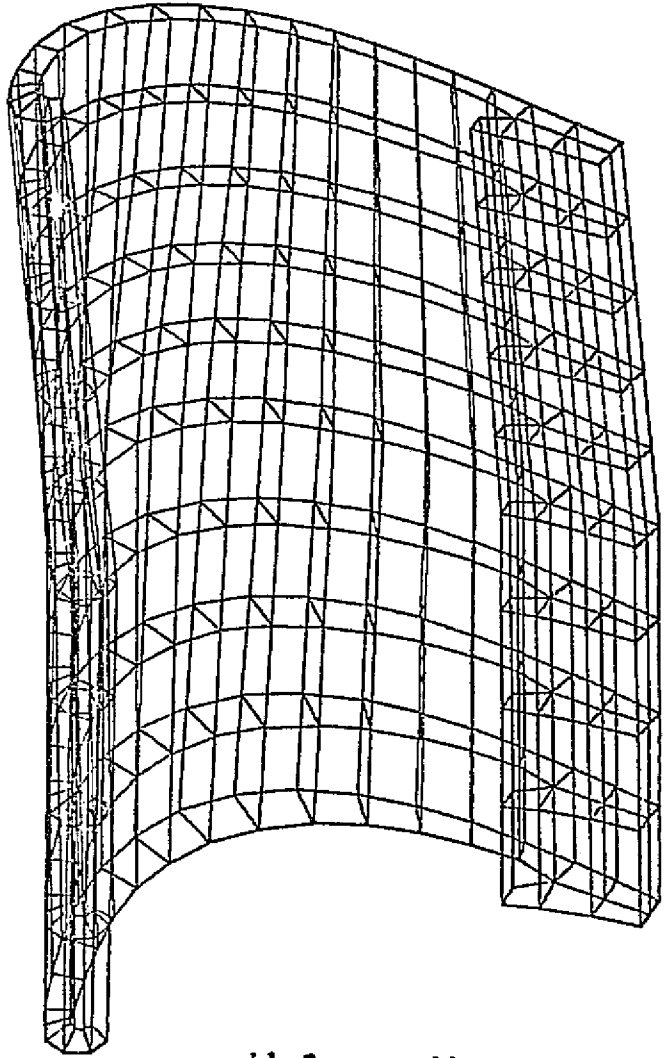
b) Convex side

Figure 3 ASKA three-dimensional airfoil model
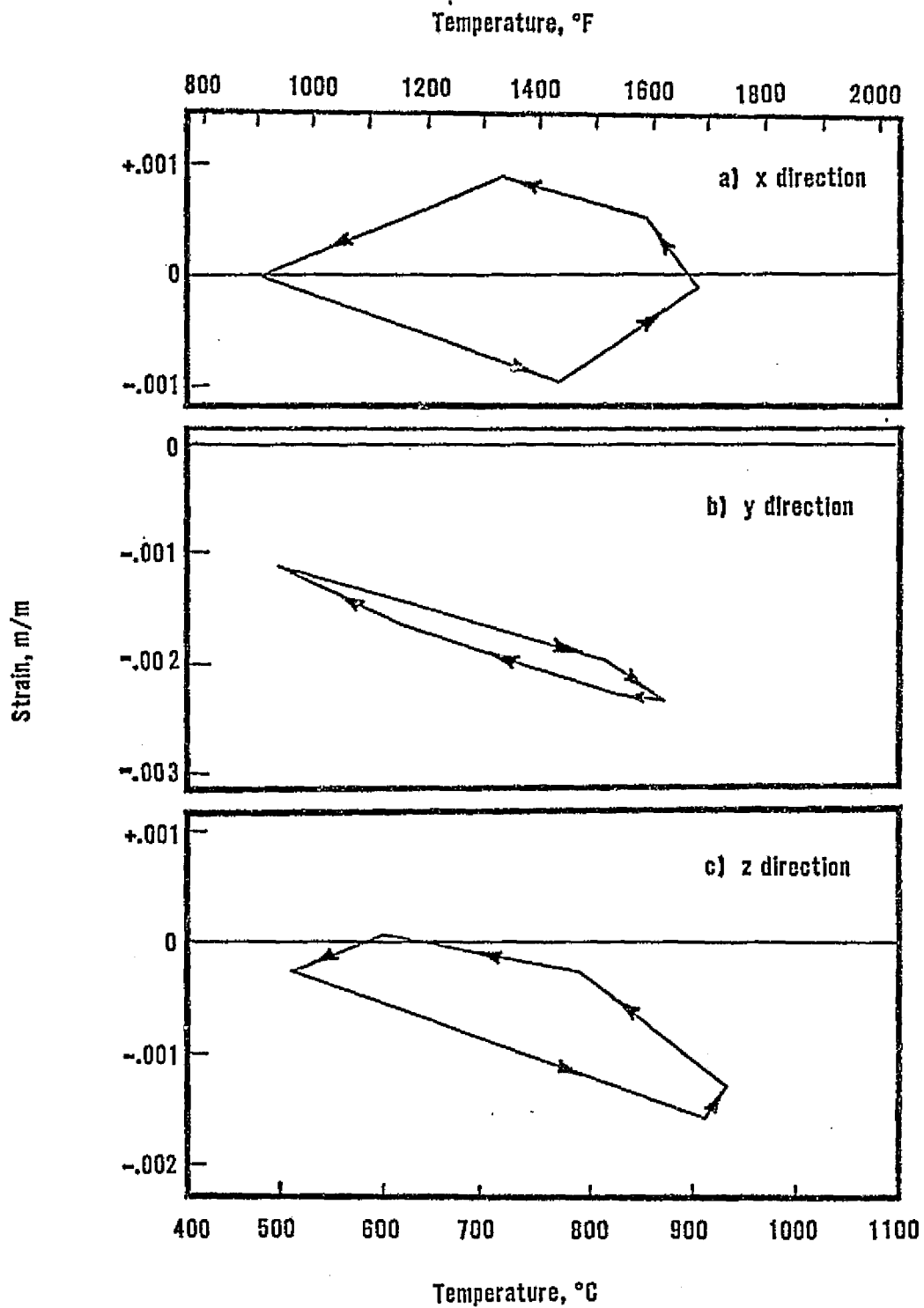
Figure 4 Temperature-strain relationships exhibiting the maximum strain range in the indicated directions (reference Figure 1) as determined by three-dimensional finite element analysis
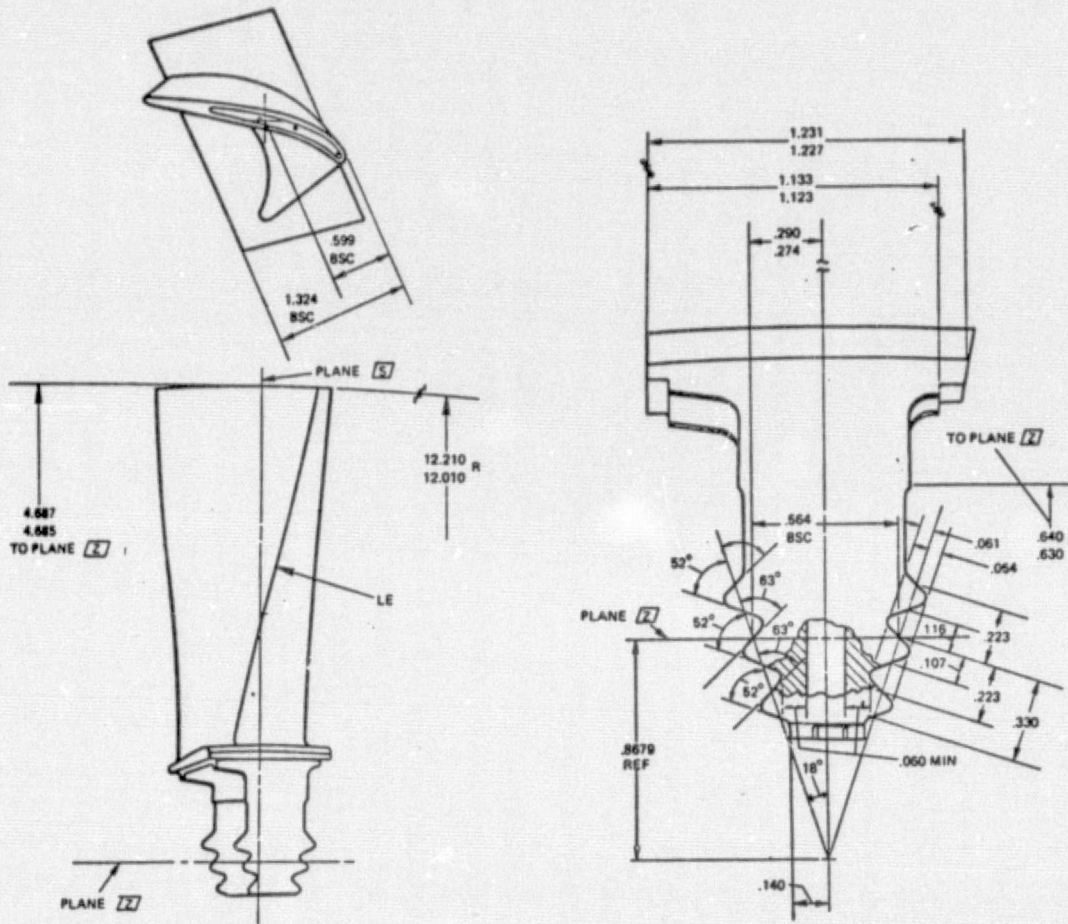
All dimensions are inches (1.0 inch = 2.54 cm)

Figure 5 Schematic representation of advanced turbine blade modeled to evaluate $\gamma/\gamma'-\delta$ root attachment capabilities
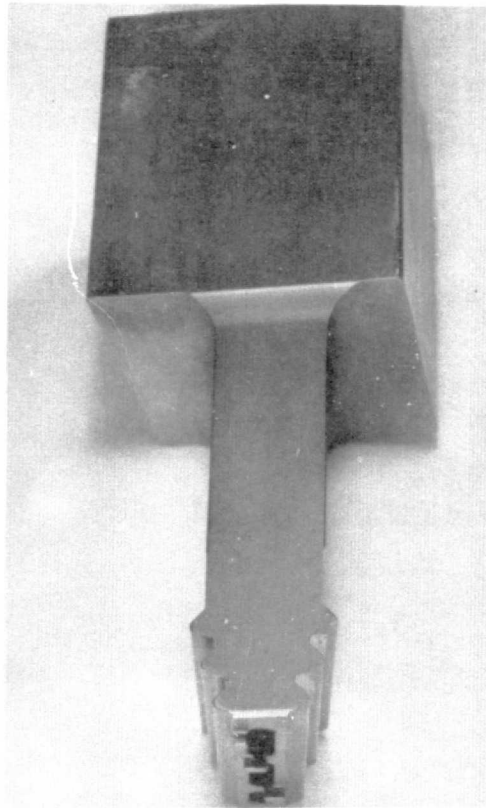
a) Root subcomponent specimen

(Root dimensions as per Figure 5)
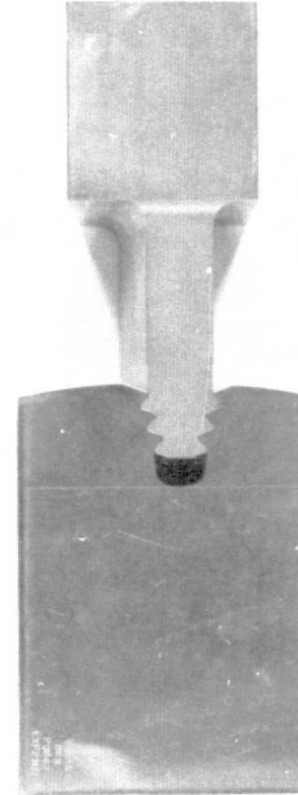
b) Mated root-pull block assembly

Figure 6   Specimen used for experimental evaluation of $\gamma/\gamma'-\delta$ D.S. eutectic root attachment capability

a) Left lug model

b) Root model
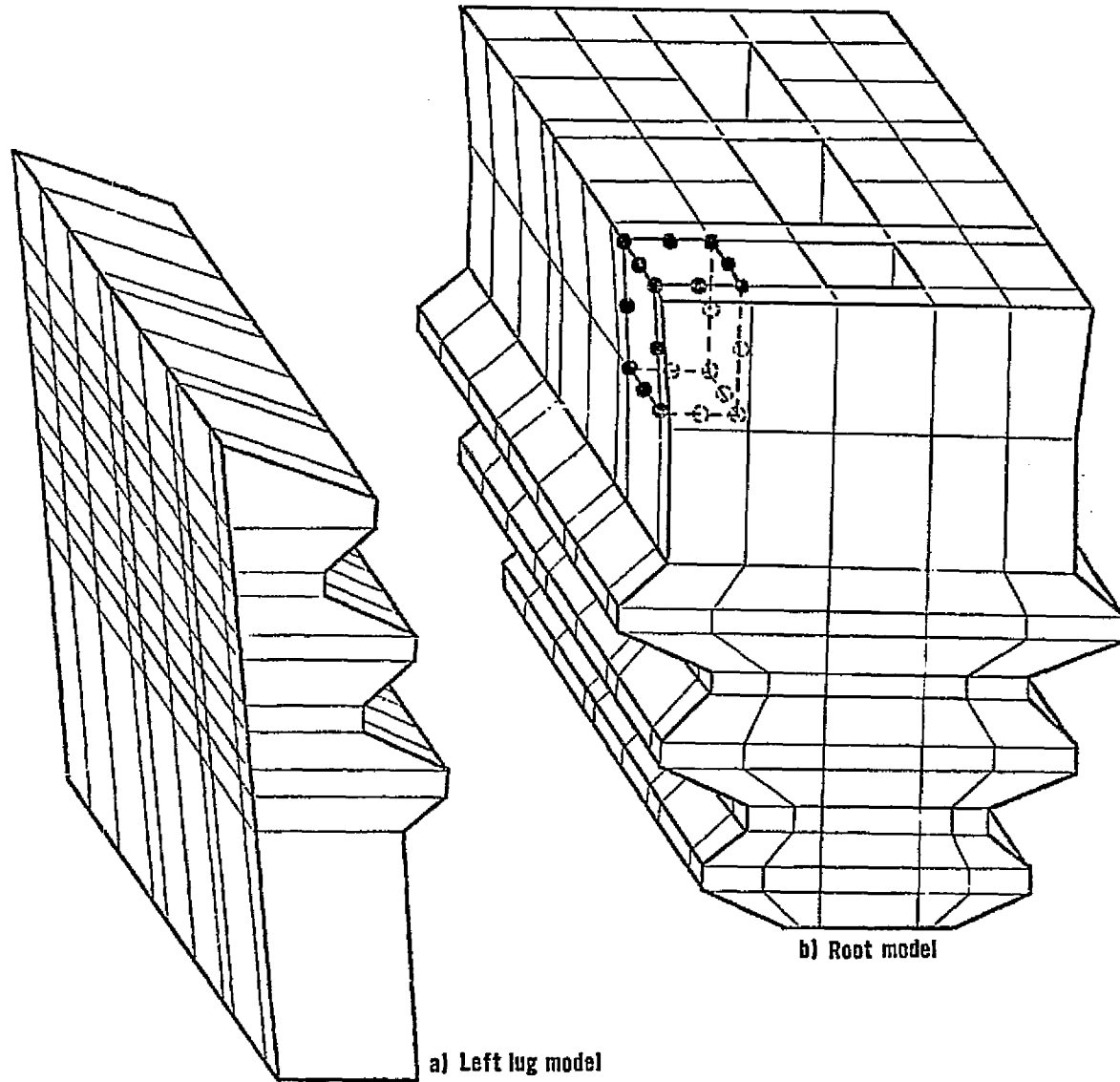
Figure 7   ASKA root and left disc lug models, showing nodes defined
for a typical Hexc twenty element

displacement applied to upper surface of model

Attachment model

fixed to allow sliding
along bearing surface

radial and axial motion only

Left lug model

Right lug model

radial

axial

tangential

fixed to ground
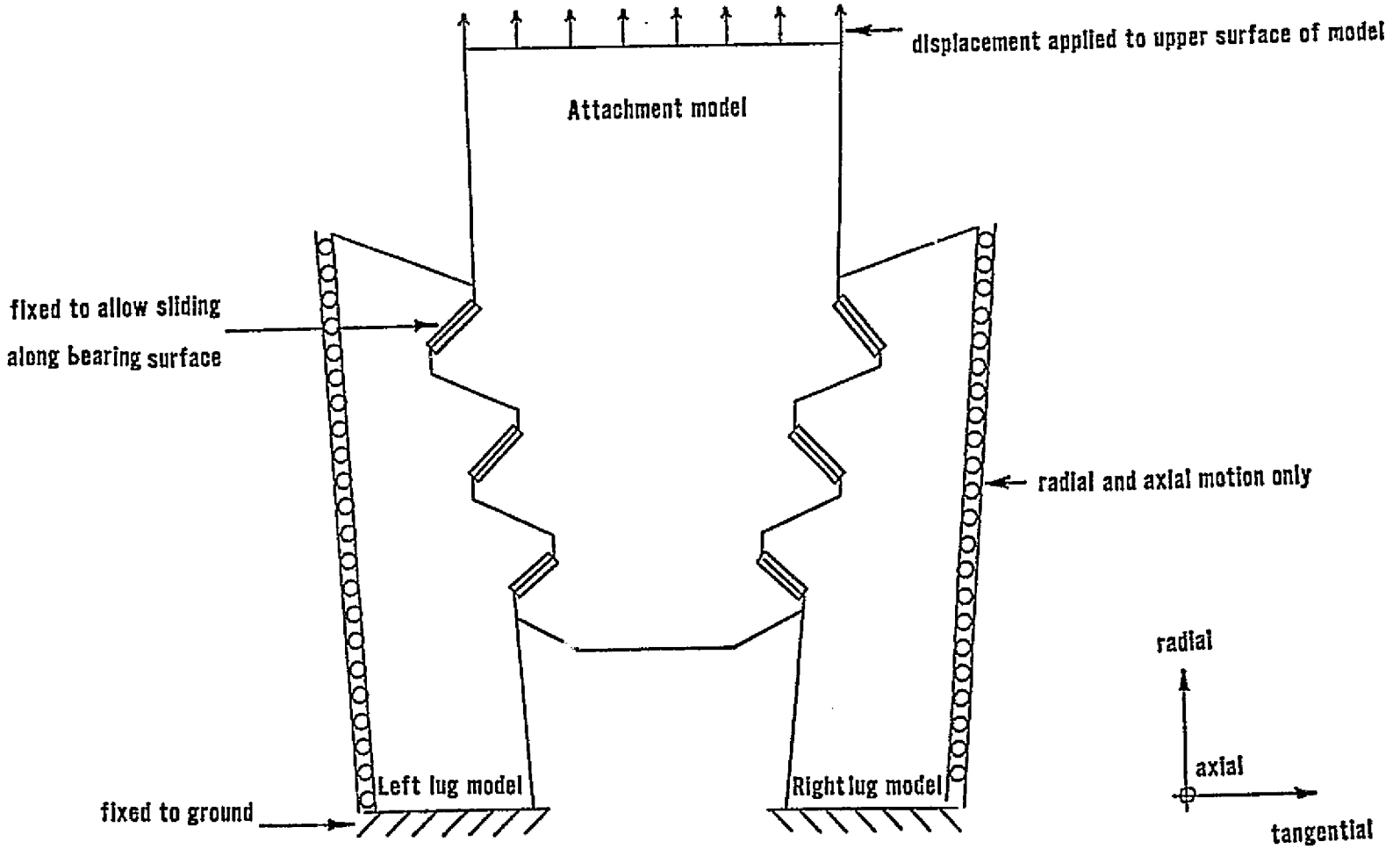
Figure 8 Boundary conditions used for analysis of root stresses

a) Neck

b) Platform

c) Concave airfoil

d) Convex airfoil
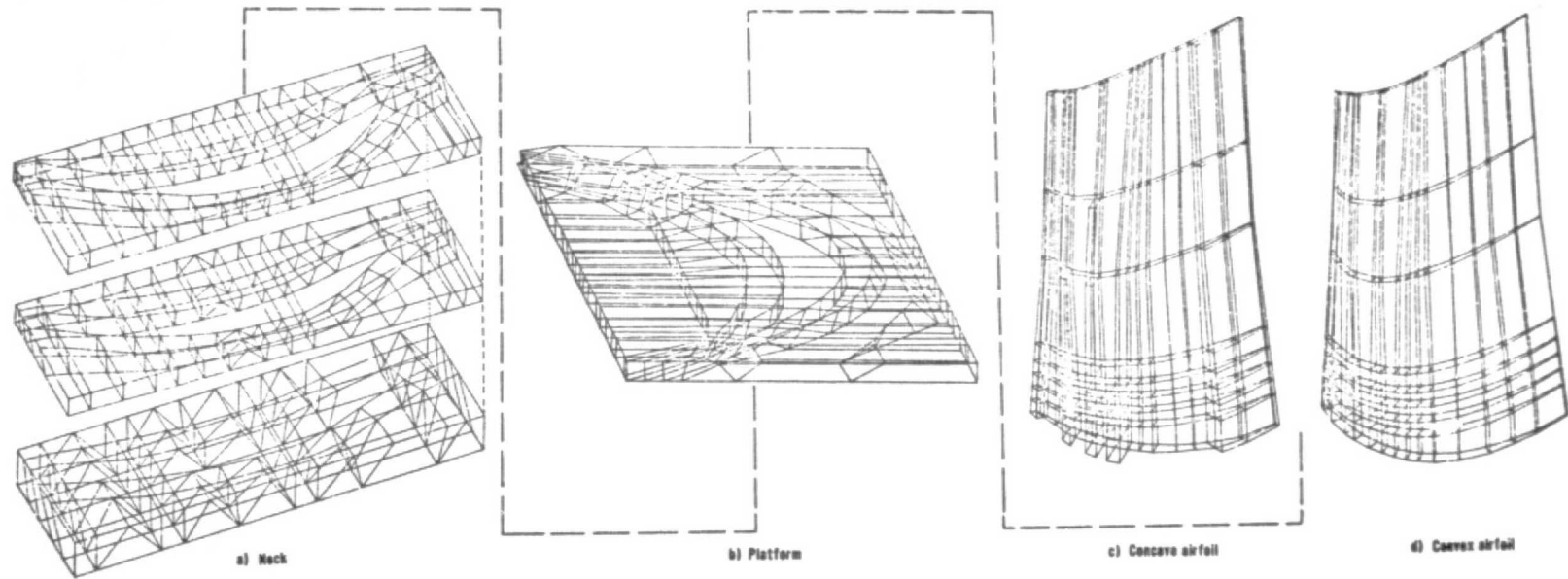
Figure 9 Airfoil – platform model used for ASKA three-dimensional stress analysis
(layers separated to permit presentation of element detail)
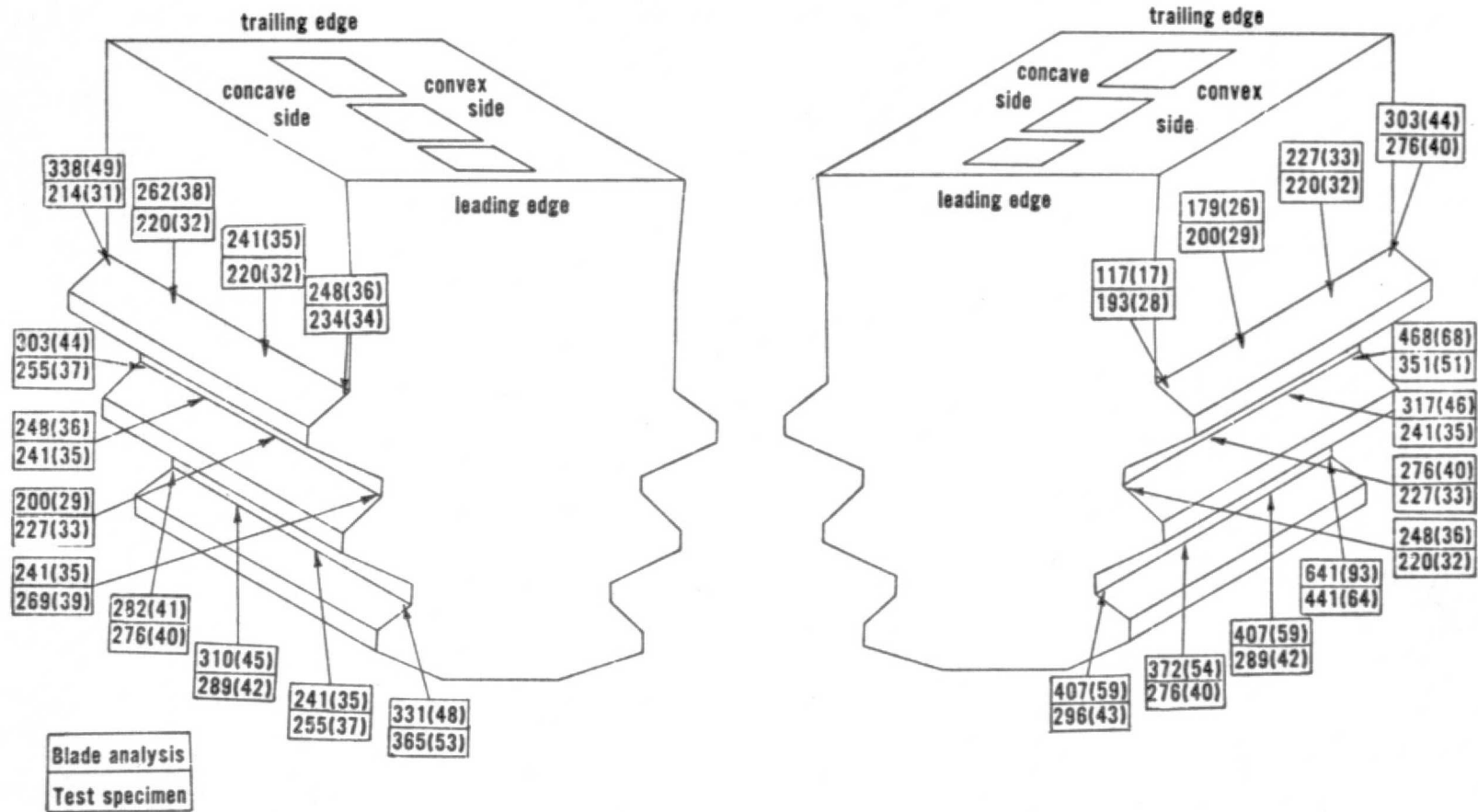
Figure 10 Concentrated shear stresses, MPa (KSI) determined at tooth bearing surfaces using ASKA three-dimensional finite element analysis
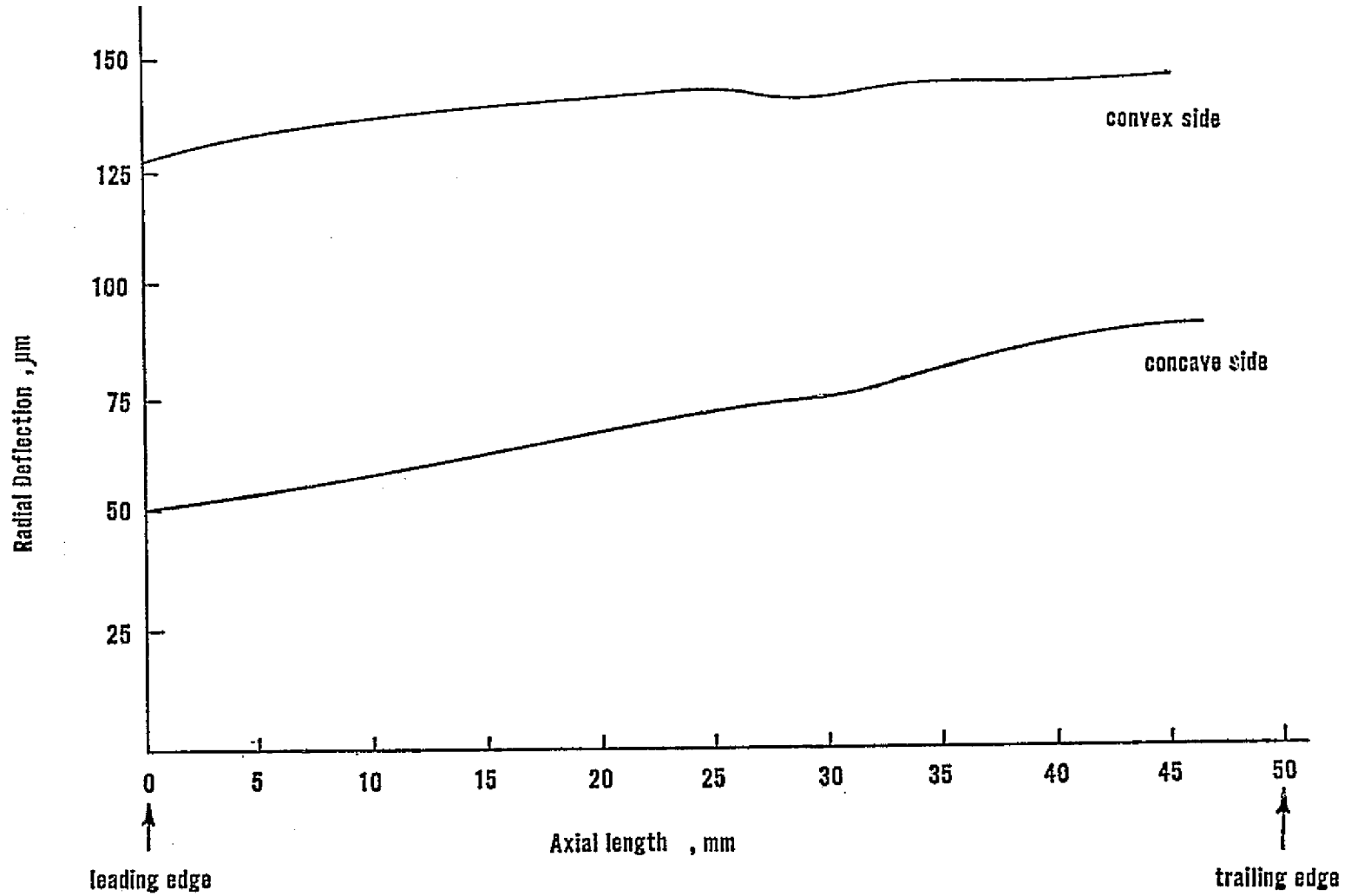
Figure 11 Radial deflections at top of attachment model due to blade pull
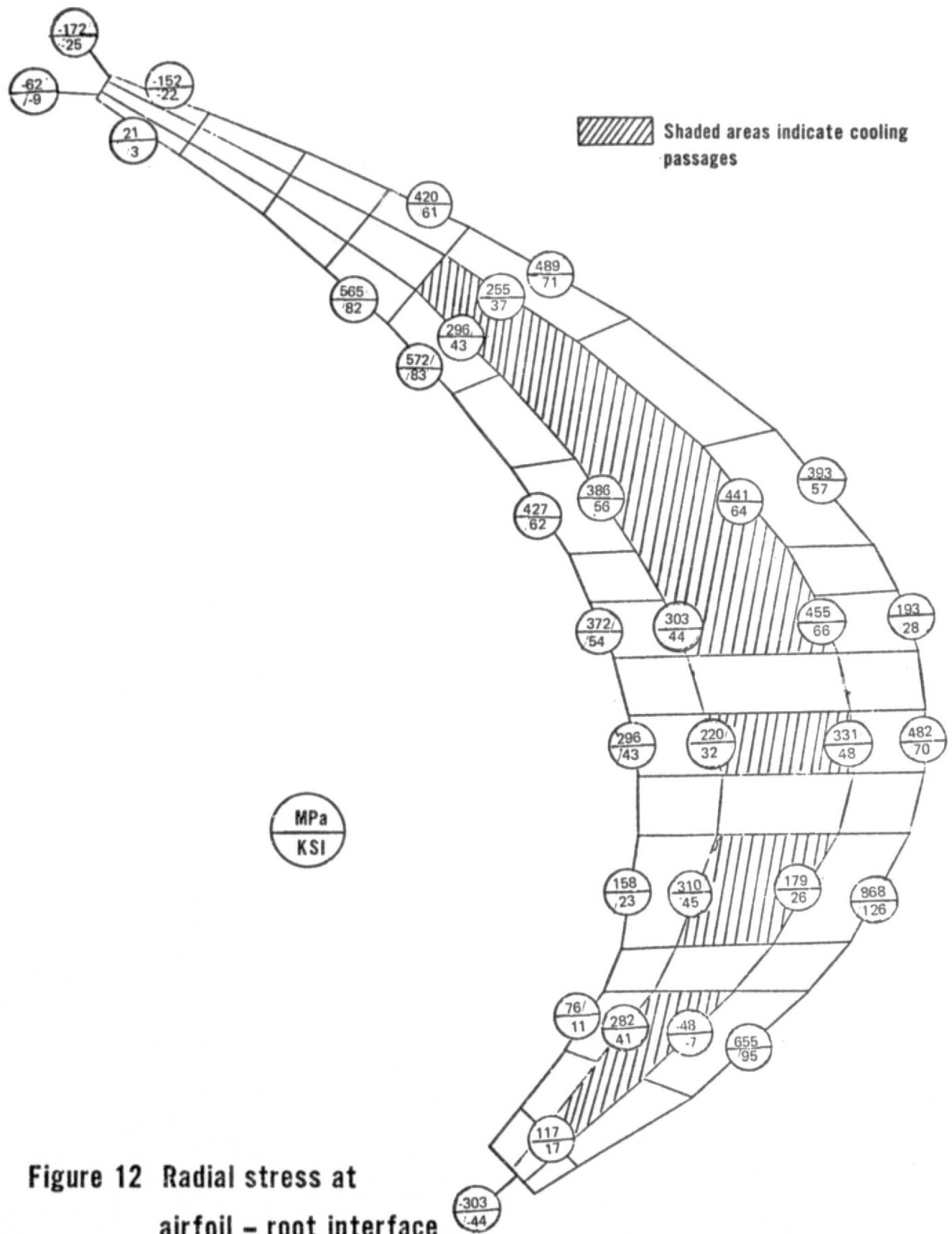
Figure 12 Radial stress at airfoil – root interface
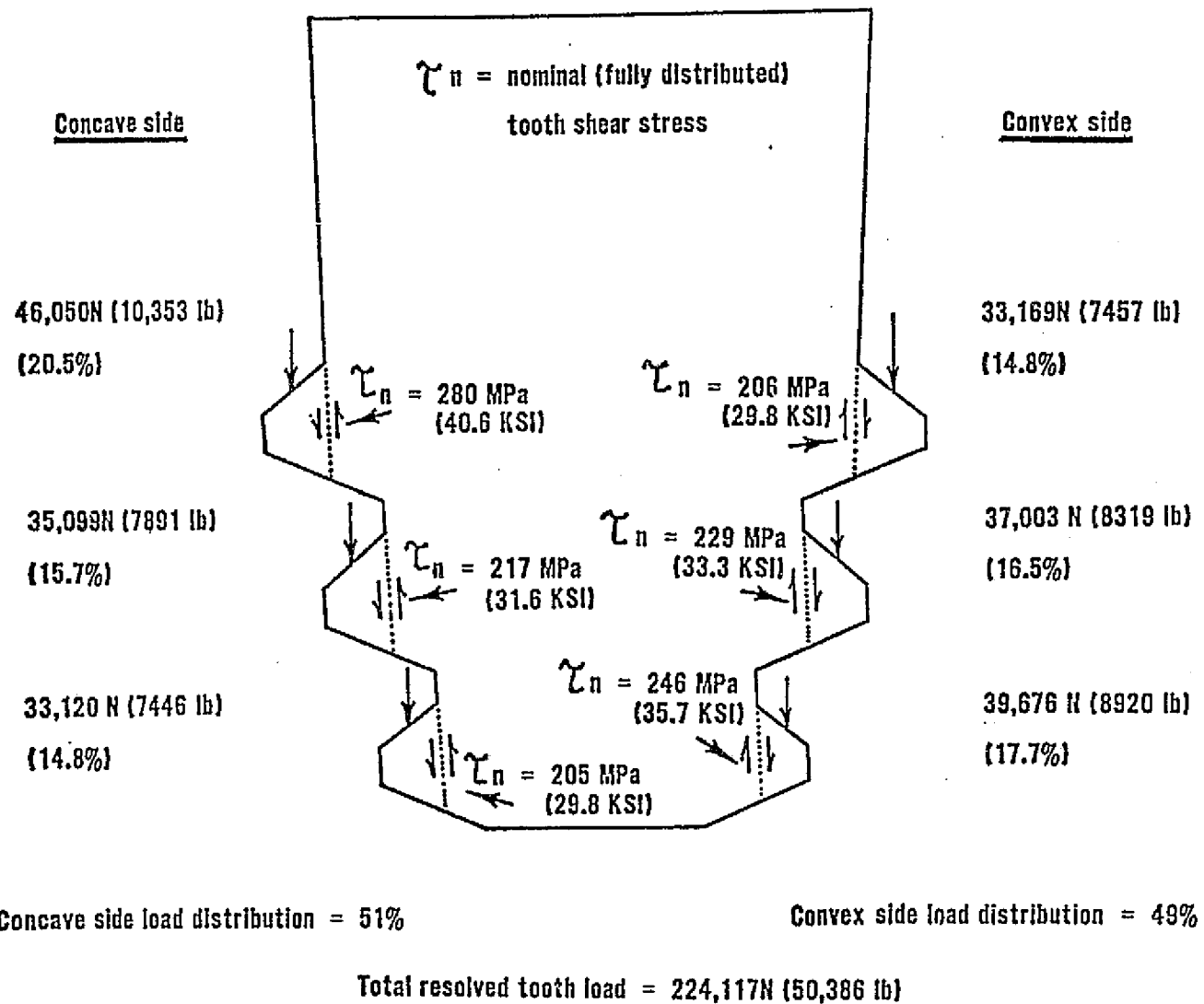
Figure 13 Resolved tooth loads

Concave side

Convex side

τ_n = nominal (fully distributed) tooth shear stress

46,050N (10,353 lb)
(20.5%)

33,169N (7457 lb)
(14.8%)

τ_n = 280 MPa (40.6 KSI)

τ_n = 206 MPa (29.8 KSI)

35,099N (7891 lb)
(15.7%)

37,003 N (8319 lb)
(16.5%)

τ_n = 229 MPa (33.3 KSI)

τ_n = 217 MPa (31.6 KSI)

33,120 N (7446 lb)
(14.8%)

39,676 N (8920 lb)
(17.7%)

τ_n = 246 MPa (35.7 KSI)

τ_n = 205 MPa (29.8 KSI)

Concave side load distribution = 51%

Convex side load distribution = 49%

Total resolved tooth load = 224,117N (50,386 lb)

deflections
calculated from
three-dimensional
analysis applied
to these surfaces

only radial deflections permitted

no deflections permitted

a) Undeflected model and applied
   boundary conditions

b) Deflected model

**Figure 14 Model used for two-dimensional root stress analysis – section analyzed
is located at the trailing edge on the convex side**

attachment

-455 MPa (-66 KSI)

-503 MPa (-73 KSI)
)

-648 MPa (-94 KSI)

-999 MPa (-145 KSI)

-861 MPa (-125 KSI)

-510 MPa (-74 KSI)

-599 MPa (-87 KSI)

-978 MPa (-142 KSI)

-799 MPa (-116 KSI)

-441 MPa (-64 KSI)

-503 MPa (-73 KSI)

-648 MPa (-94 KSI)

σ

lug

a) Normal stress across teeth

attachment

765 MPa (111 KSI)

469 MPa (68 KSI)

427 MPa (62 KSI)

579 MPa (84 KSI)

875 MPa (127 KSI)

469 MPa (68 KSI)

407 MPa (59 KSI)

586 MPa (85 KSI)

923 MPa (134 KSI)

503 MPa (73 KSI)

434 MPa (63 KSI)

379 MPa (55 KSI)

τ

lug

b) Shear stress

Figure 15 Local (concentrated) stresses calculated from two-dimensonal
analysis
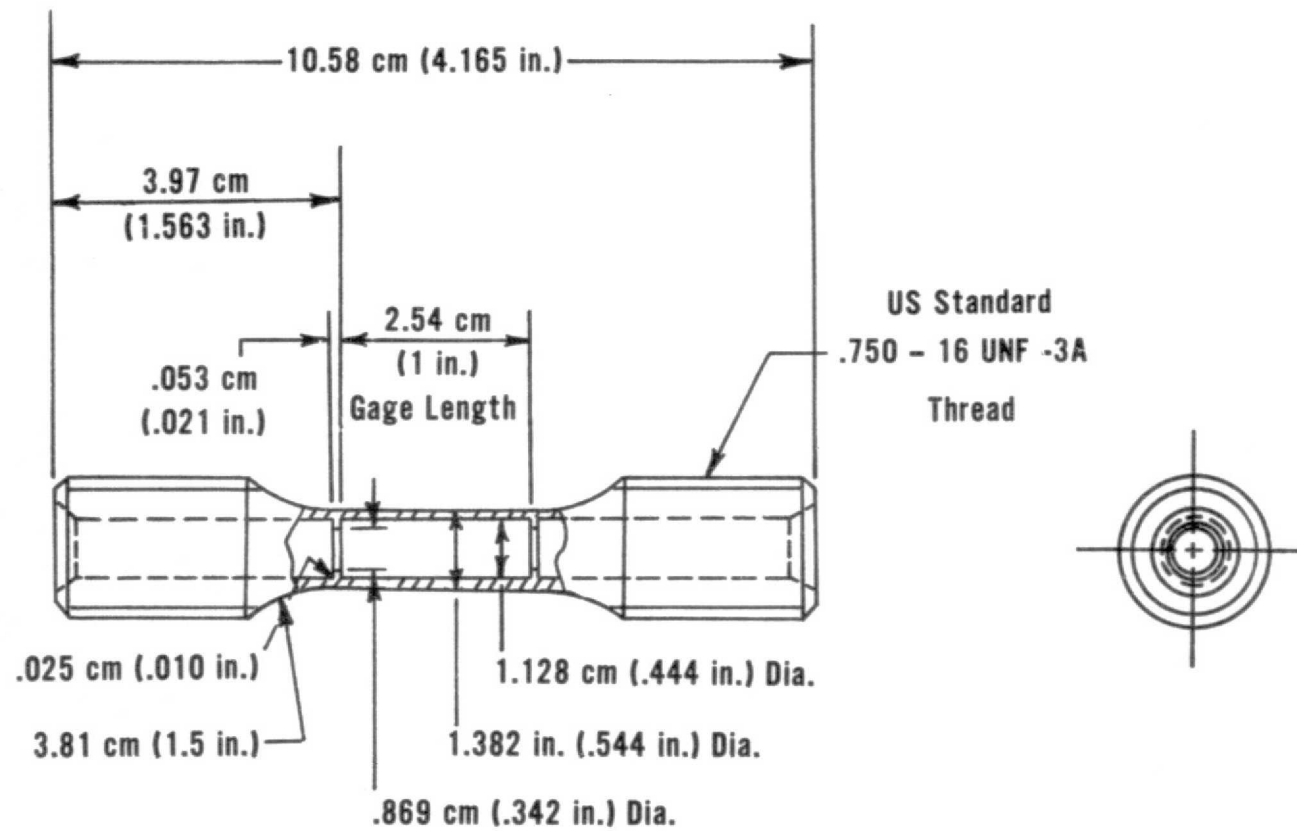
Figure 16 Thermomechanical fatigue test   specimen
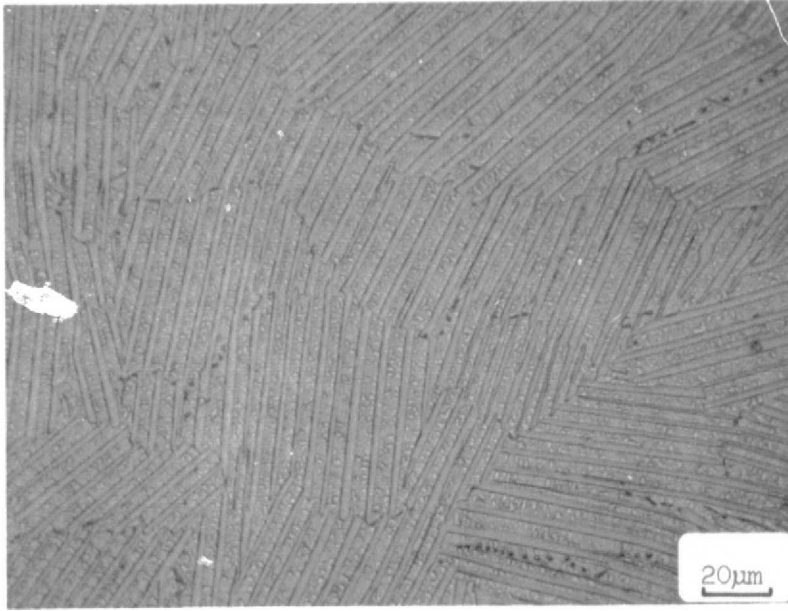
a) Longitudinal TMF Specimen A76-130
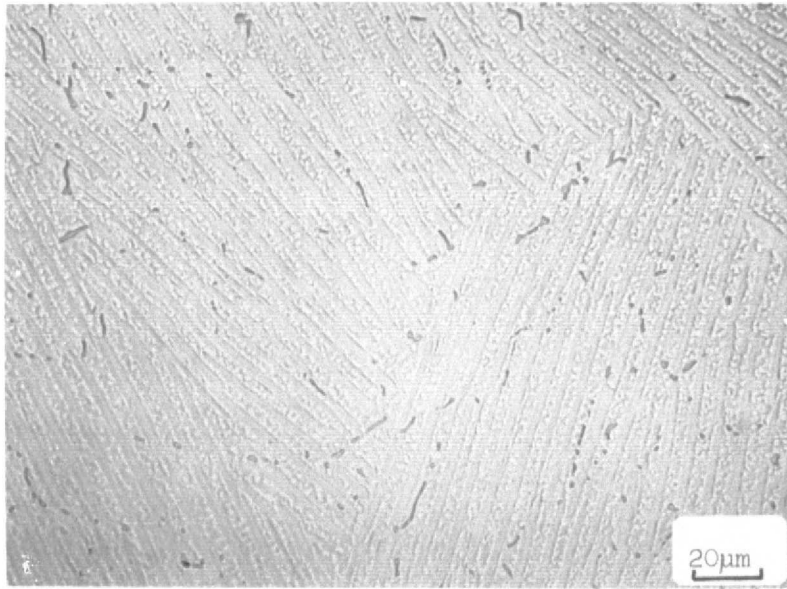
b) Transverse TMF Specimen E582B

Figure 17 Typical transverse microstructures found in longitudinal and transverse TMF castings

Solidification direction normal to paper
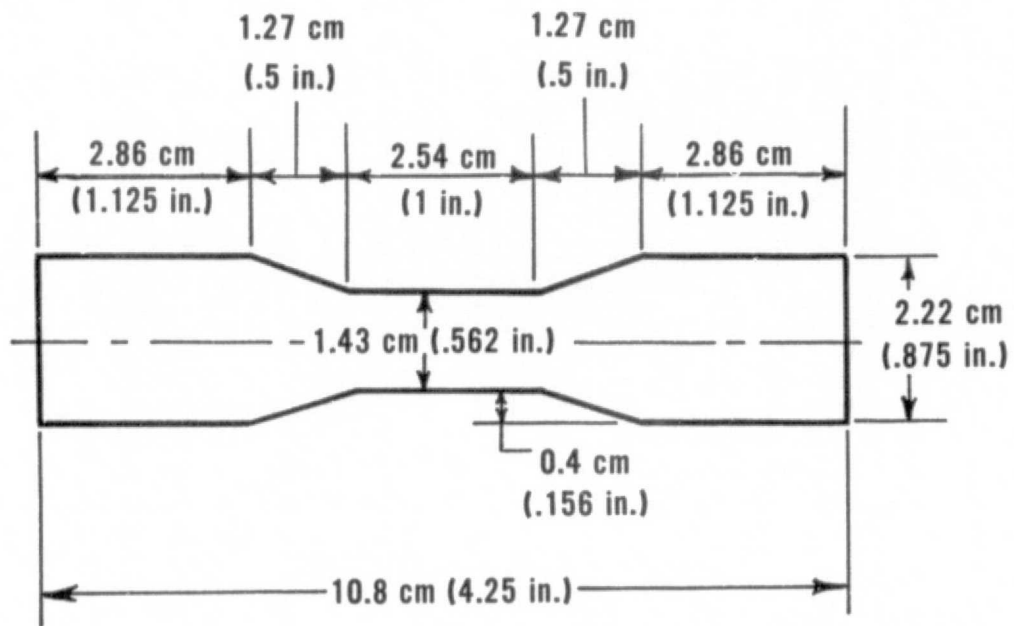
a) Casting cross section
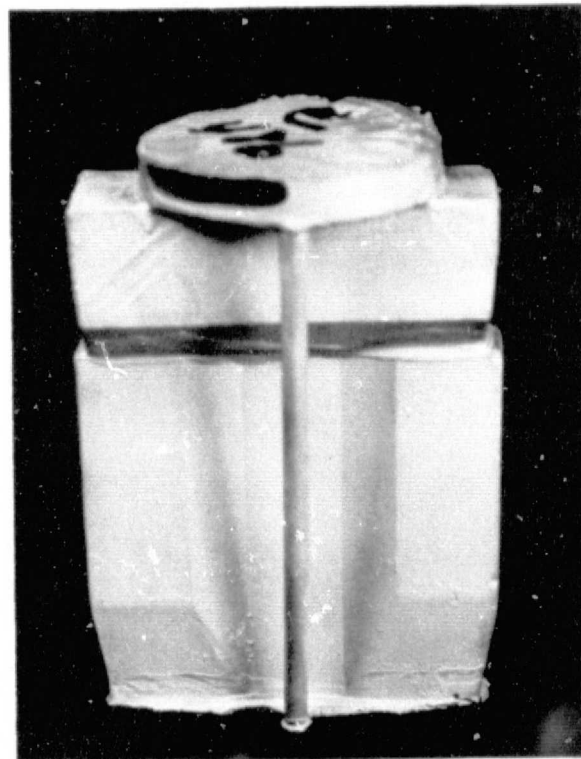
b) Photograph of casting

Figure 18 Casting used to produce material for transverse TMF specimens
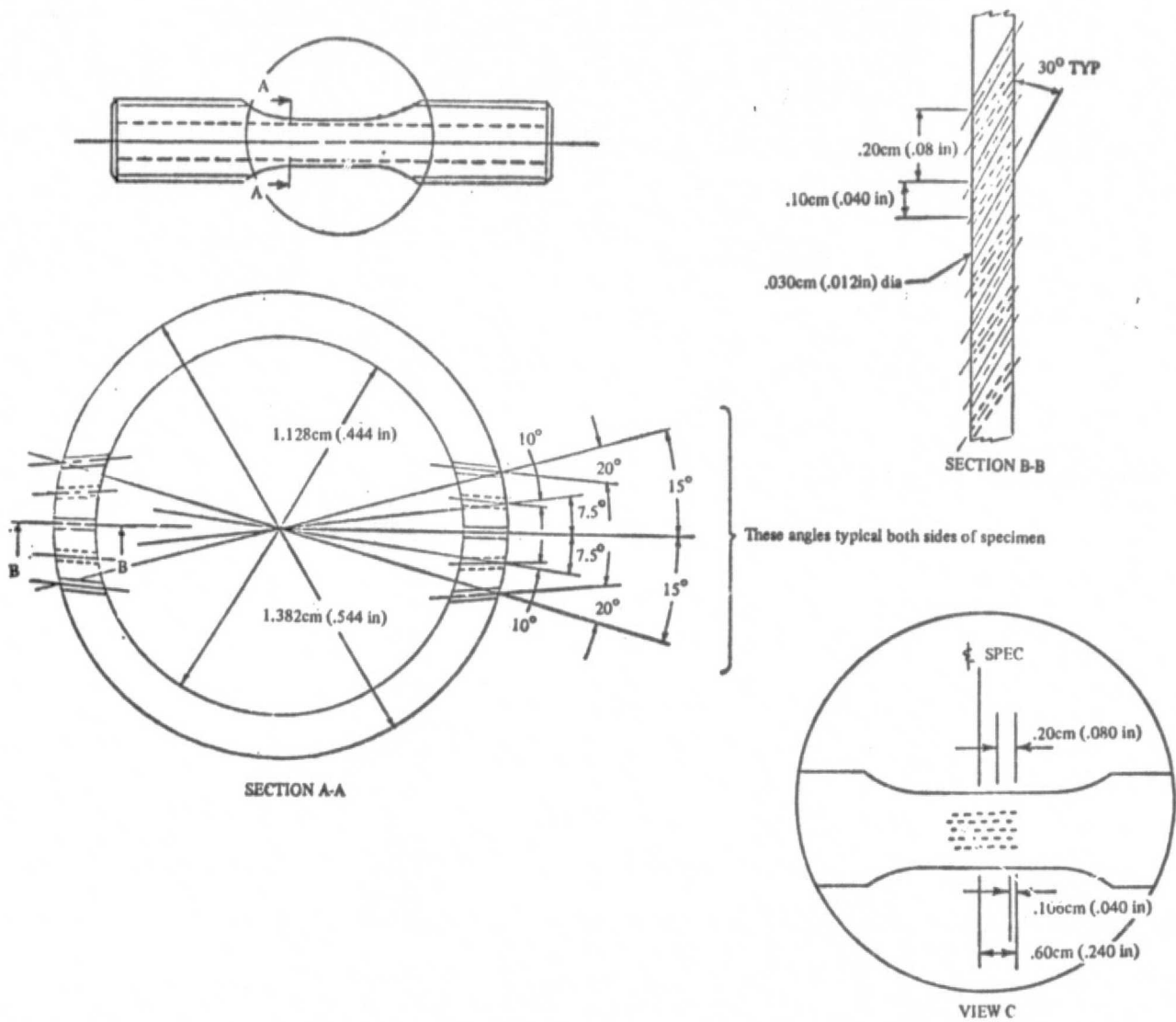
Figure 19 "Showerhead" thermomechanical fatigue test specimen used to evaluate the influence of leading edge cooling holes on thermal fatigue behavior
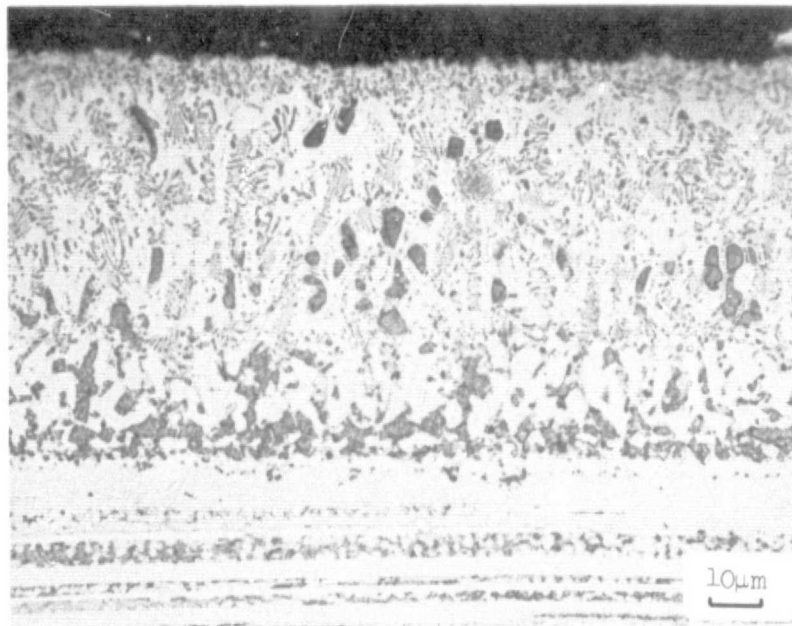
Figure 20 Coating microstructure found in specimen A76-122 cycled 865 times from 504 to 938°C (940 to 1720°F)
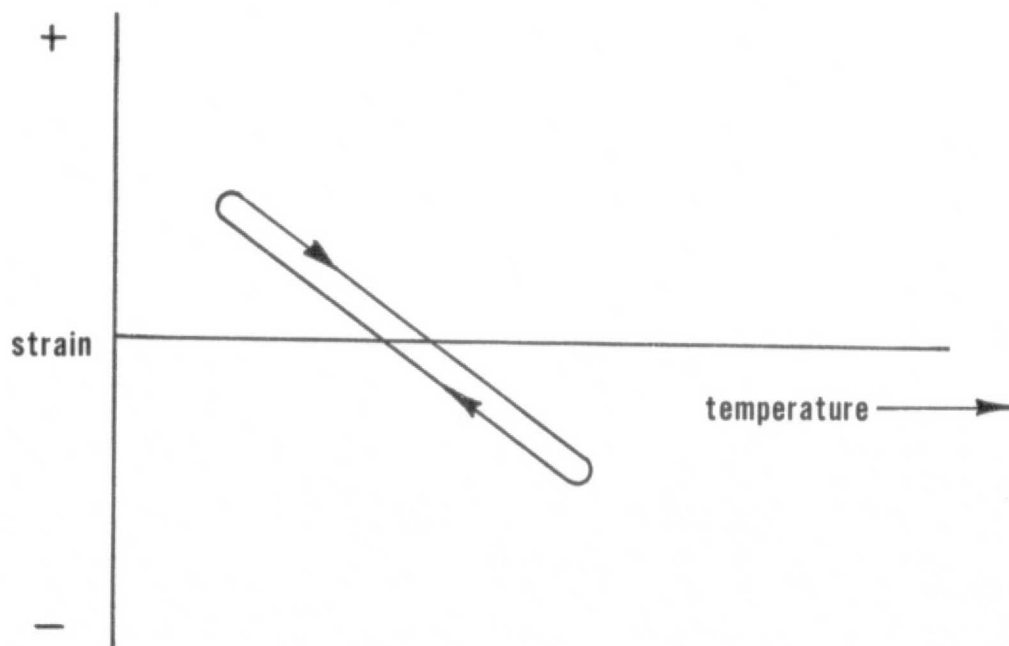
Figure 21 Schematic illustration of Cycle I thermomechanical fatigue cycle
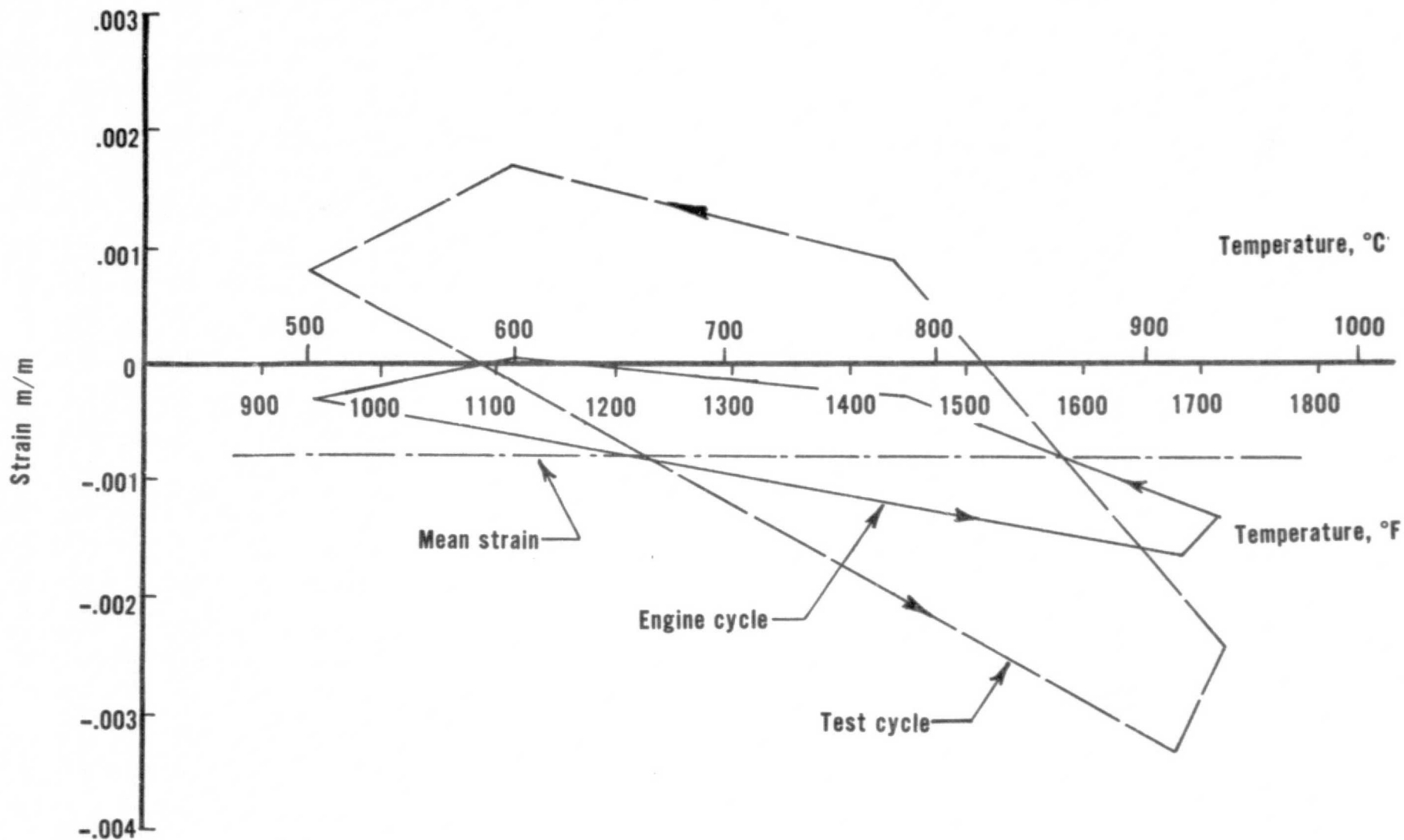
Figure 22 Scaling of maximum spanwise engine cycle to increase strain range
for generation of S-N curve
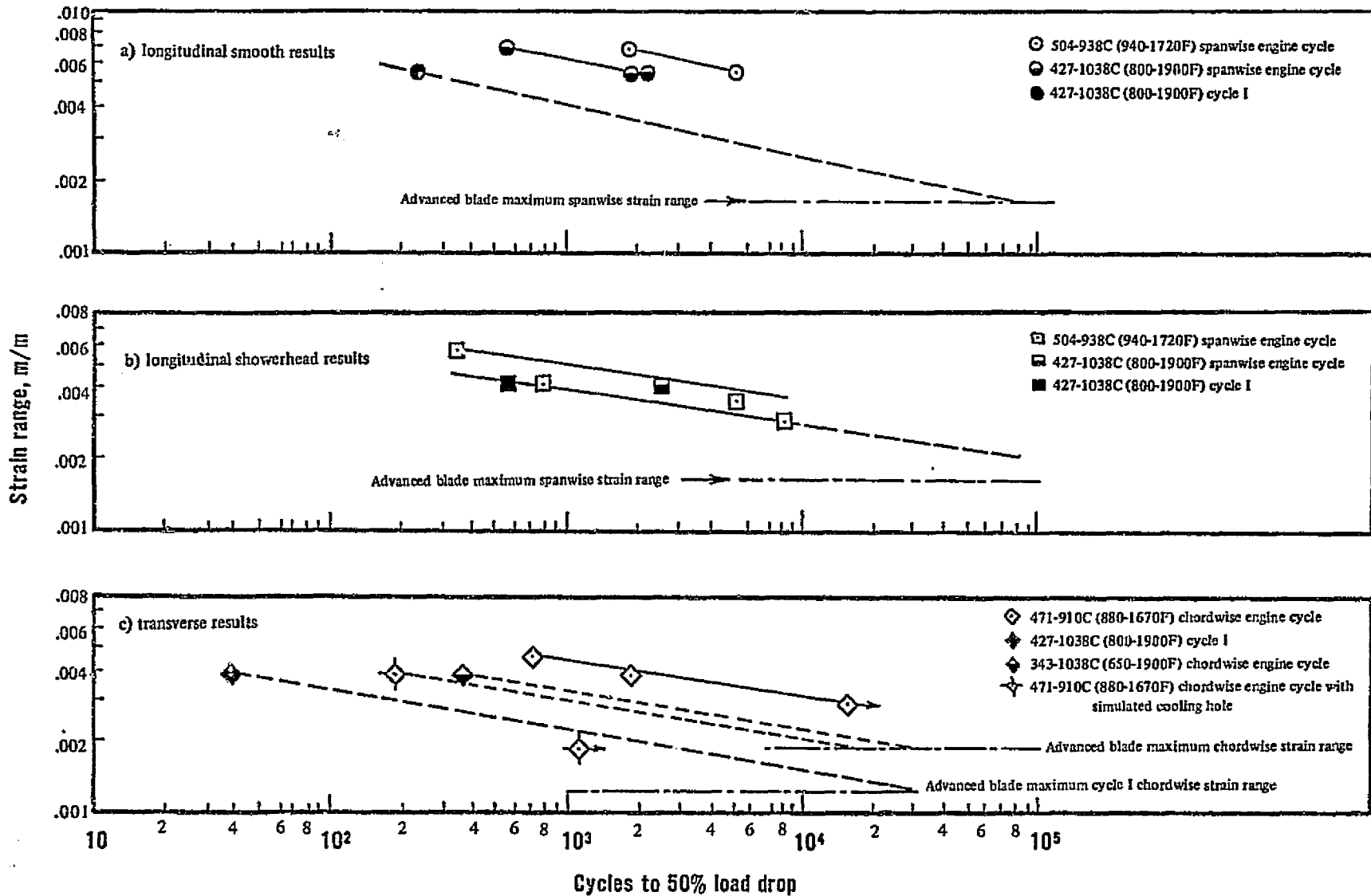
Figure 23 Results of thermomechanical fatigue tests on $\gamma/\gamma'-\delta$ D.S. Eutectic alloy
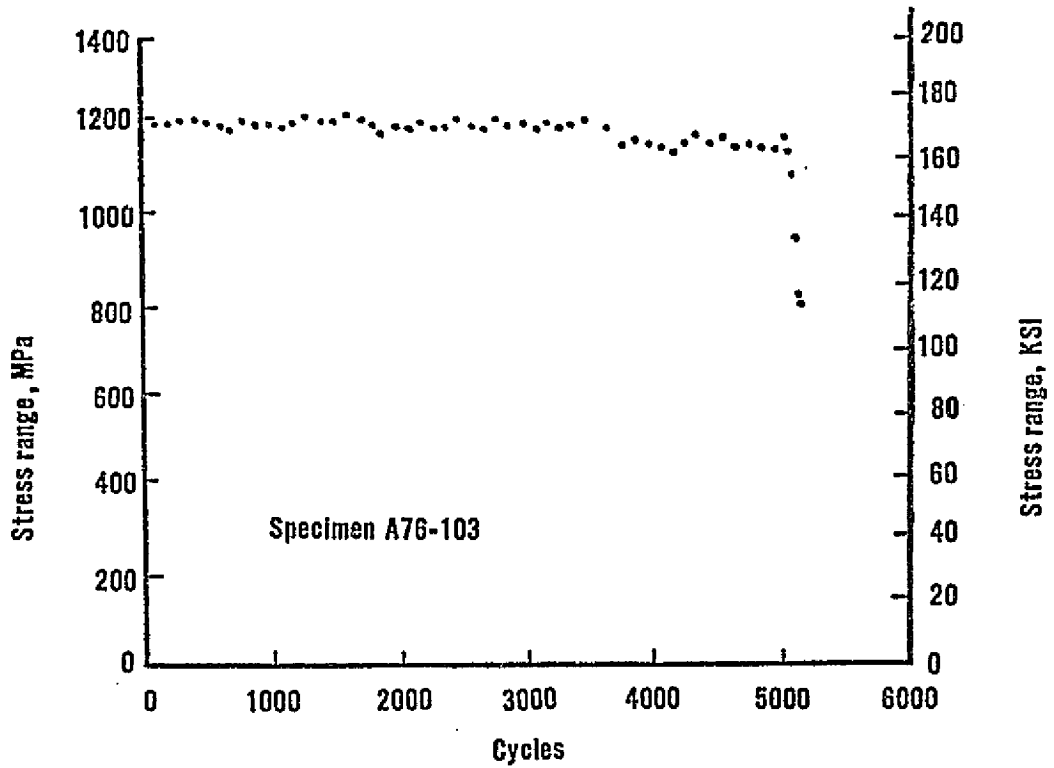
a) Smooth specimen load drop
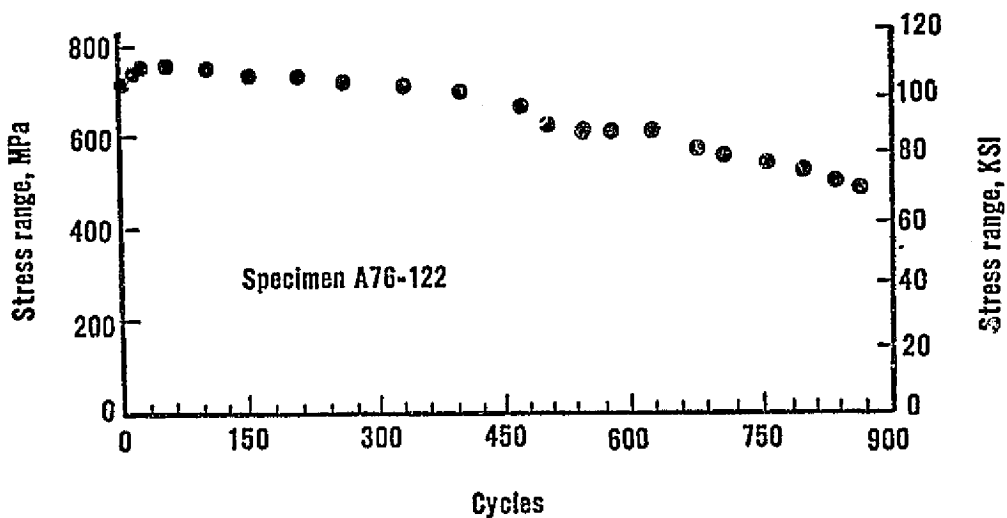
b) Showerhead specimen load drop

Figure 24   Typical load-drop curve for smooth and showerhead
longitudinal thermomechanical fatigue specimens
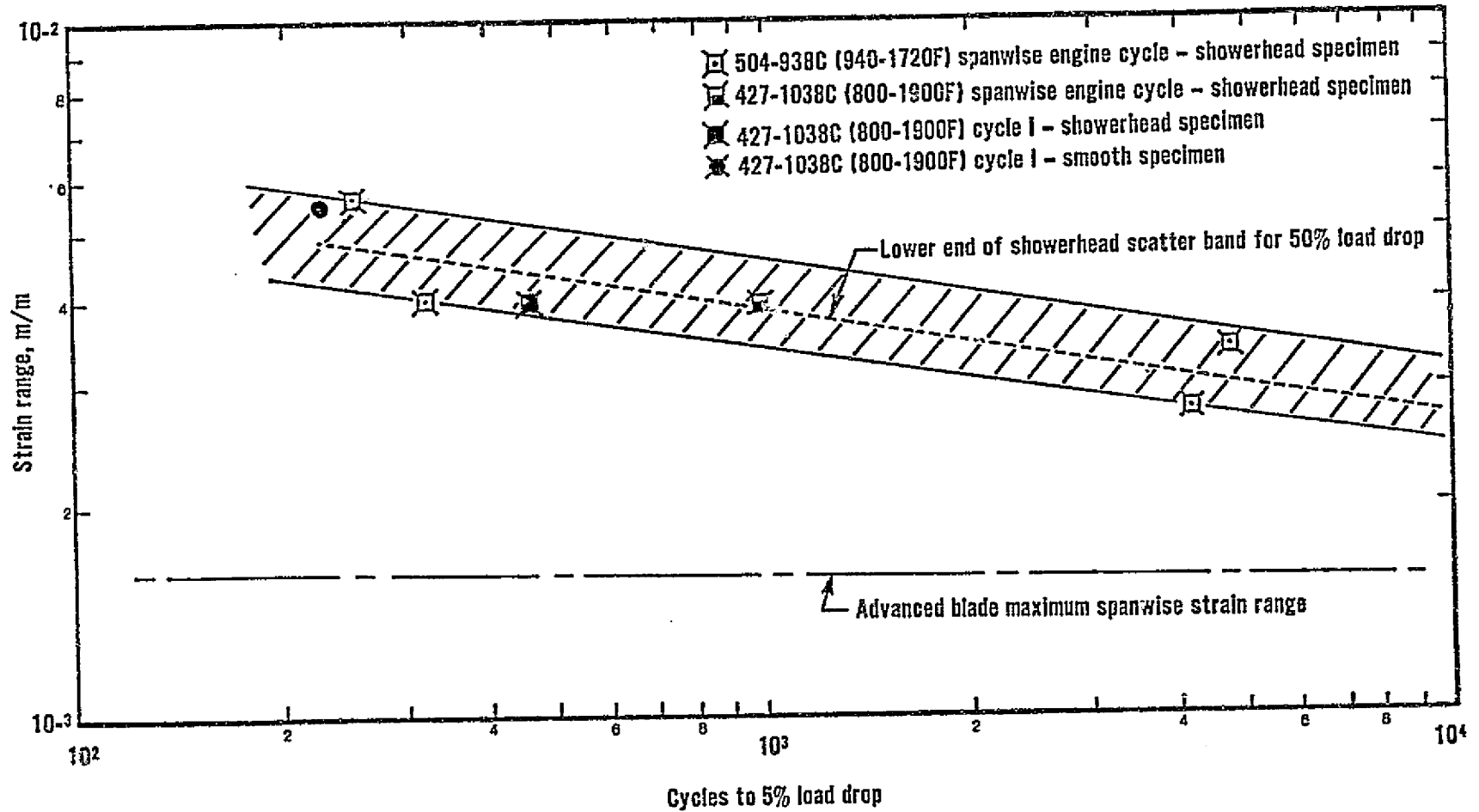
FIGURE 25 Longitudinal thermomechanical fatigue results characterized in terms of 5% load drop failure criterion
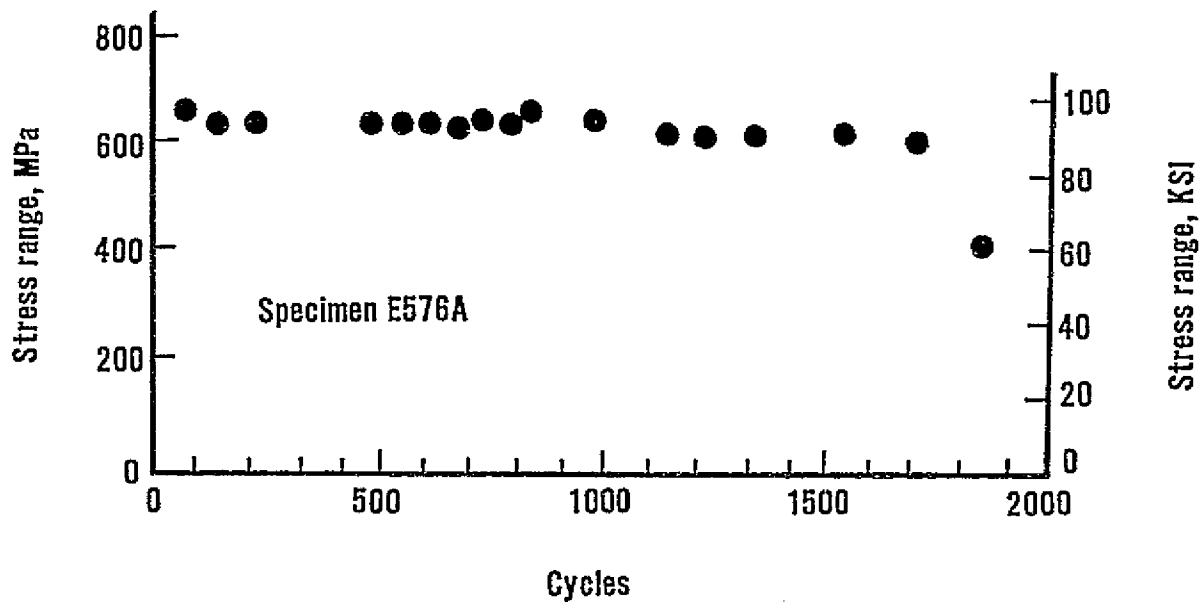
Figure 26 Typical load drop curve for transverse thermomechanical fatigue specimen
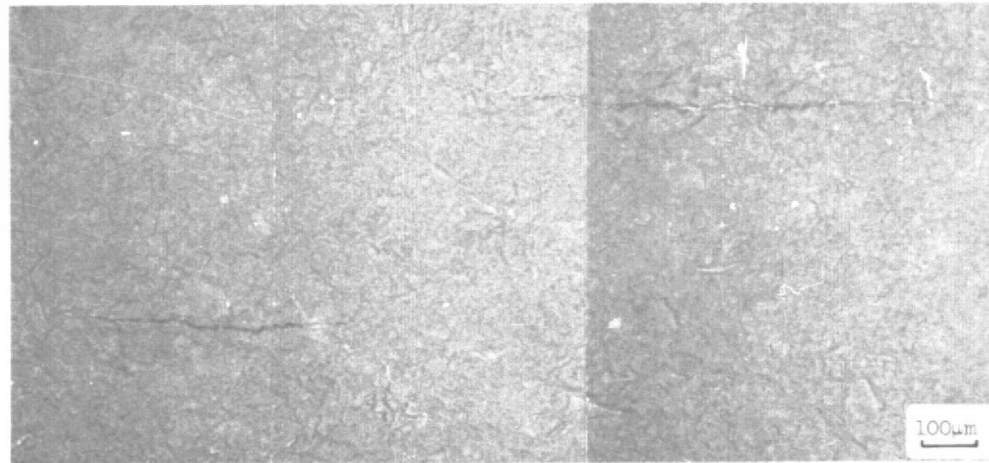
a) Coating cracks found on surface replica of specimen A76-103 at 3782 cycles
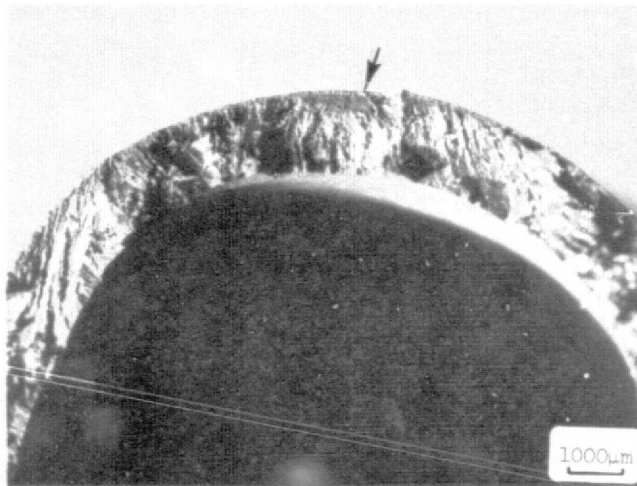
b) Fracture surface of specimen A76-103 showing coating-initiated fatigue crack (arrow)
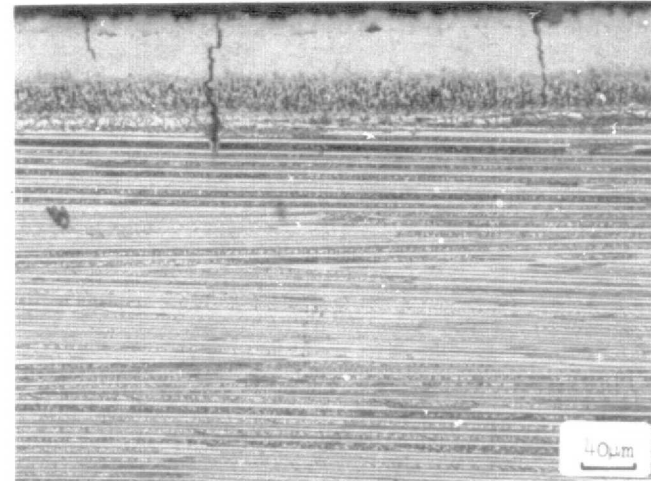
c) Secondary coating cracks found in specimen A76-216

Figure 27 Typical coating cracks found in smooth longitudinal thermomechanical fatigue specimens
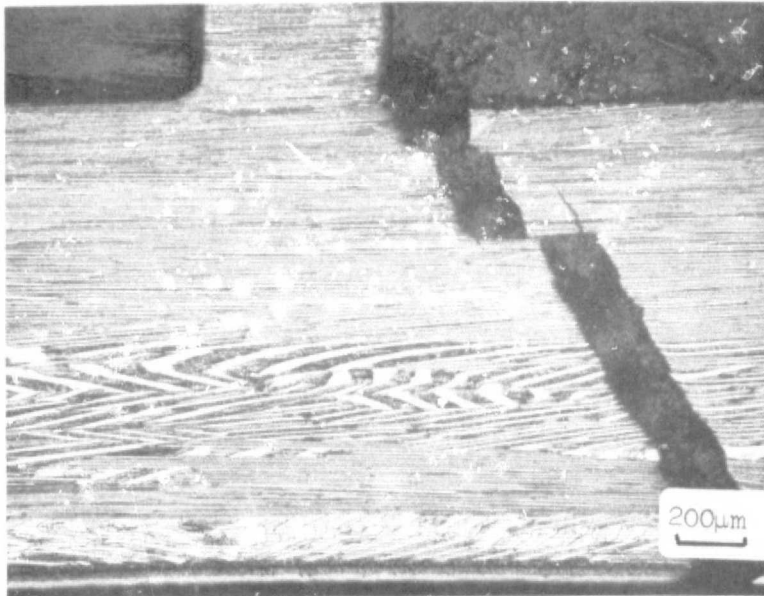
a) Extensometer ridge failure found in smooth longitudinal
   specimen A76-171 tested with 427-1038C (800-1900F)
   spanwise engine cycle
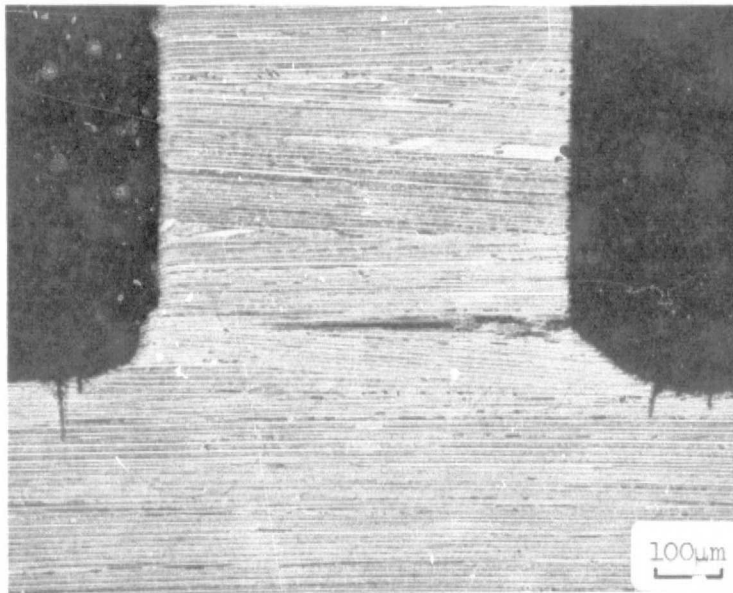
b) Incipient extensometer ridge cracks found in smooth
   longitudinal specimen A76-103 tested with 504-938C
   (940-1720F) spanwise engine cycle

Figure 28 Cracks found at internal extensometer ridges
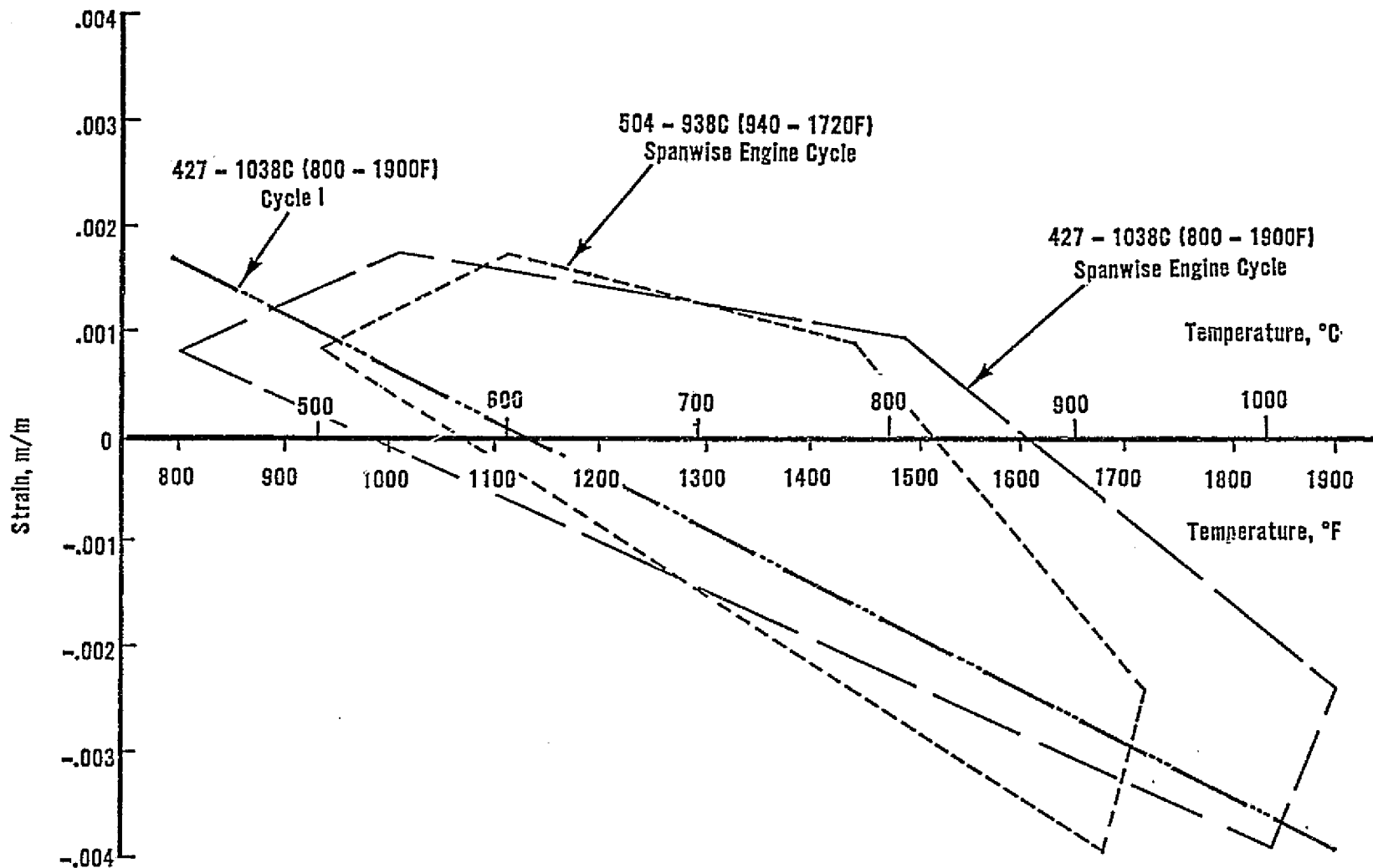
Figure 29 Comparison of three strain-temperature relationships investigated on smooth longitudinal specimens (0.0056 m/m strain range shown)
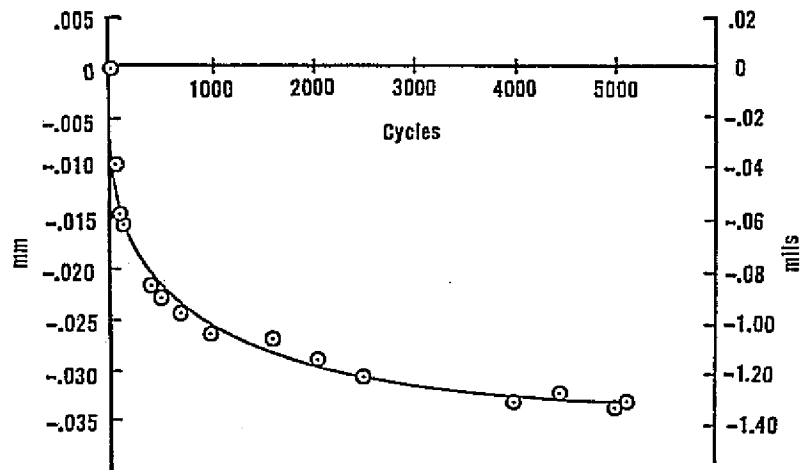
a) Change of specimen length
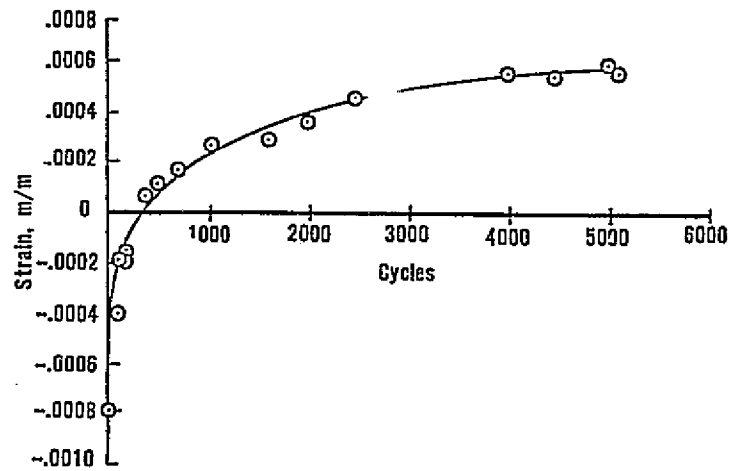
b) Change of mean strain
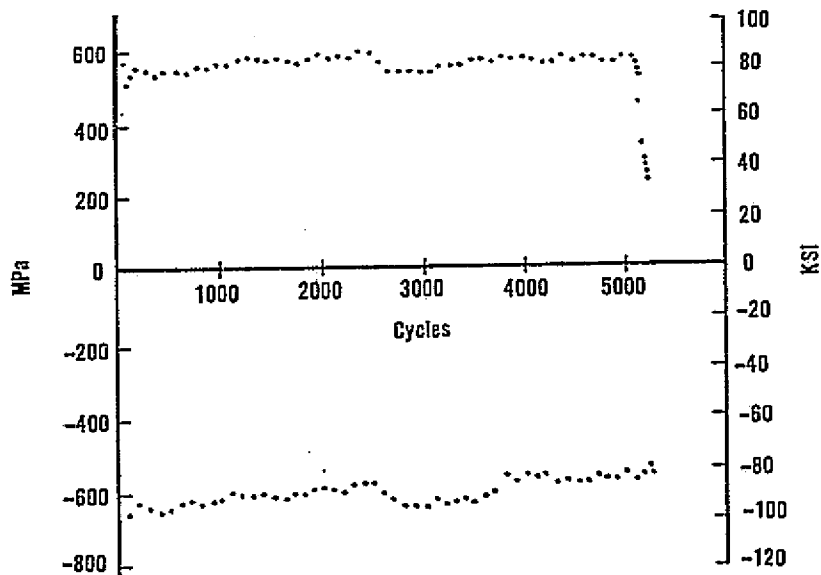
c) Peak tensile and compressive stresses
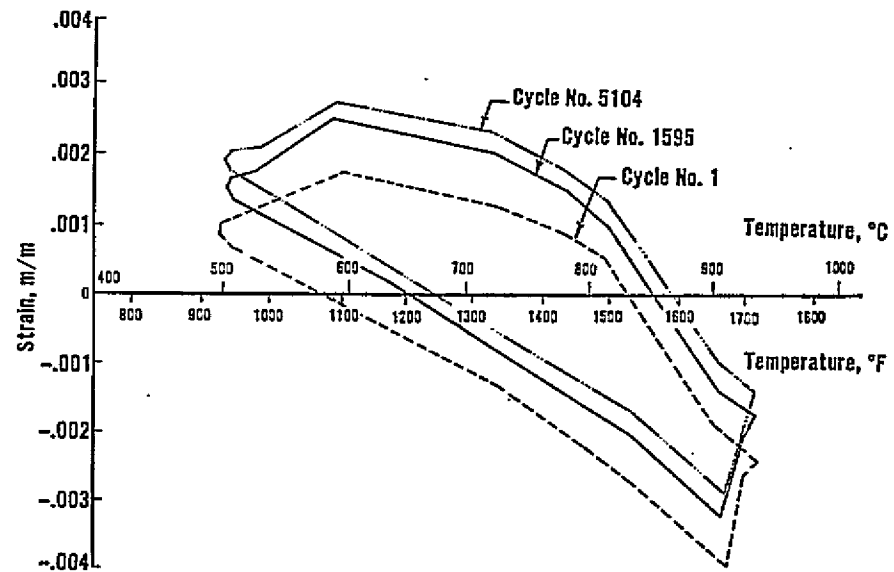
d.) Strain-temperature cycle

Figure 30   Incremental variation (shake down) of stress, strain and length
measured on smooth longitudinal specimen A76-103

stress ~ MPa

stress ~ KSI

Specimen A76-103, 504-938C (940-1720F)
Spanwise engine cycle, 0.0056 m/m Δε

Specimen A76-120, 427-1038C (800-1900F)
Spanwise engine cycle, 0.0056 m/m Δε

Specimen A76-211, 427-1038C (800-1900F)
Cycle I, 0.0056 m/m Δε

Cycles

Peak tensile and compressive stresses
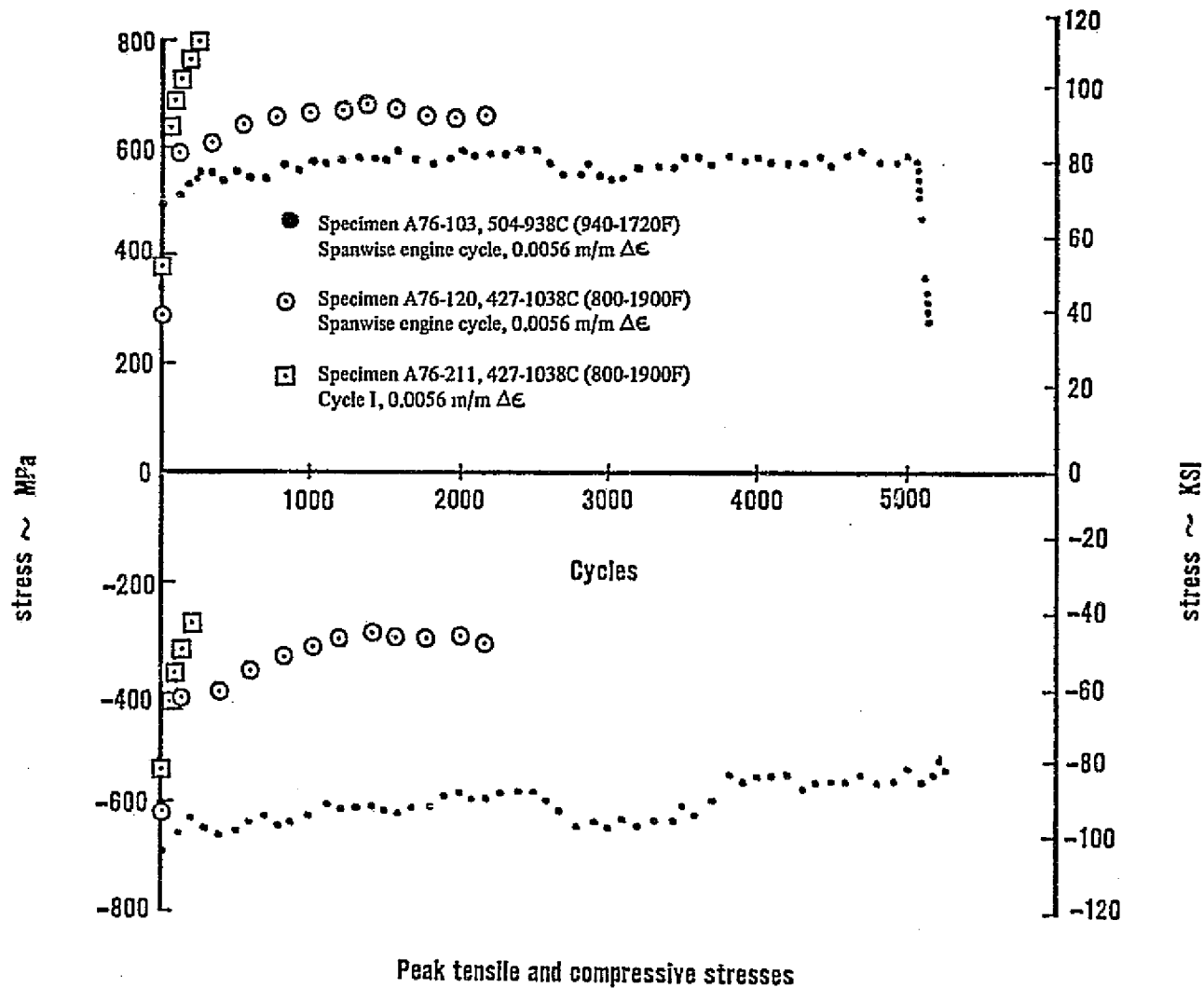
FIGURE 31 Load shake down observed for three types of strain-temperature cycles
investigated on smooth longitudinal specimens
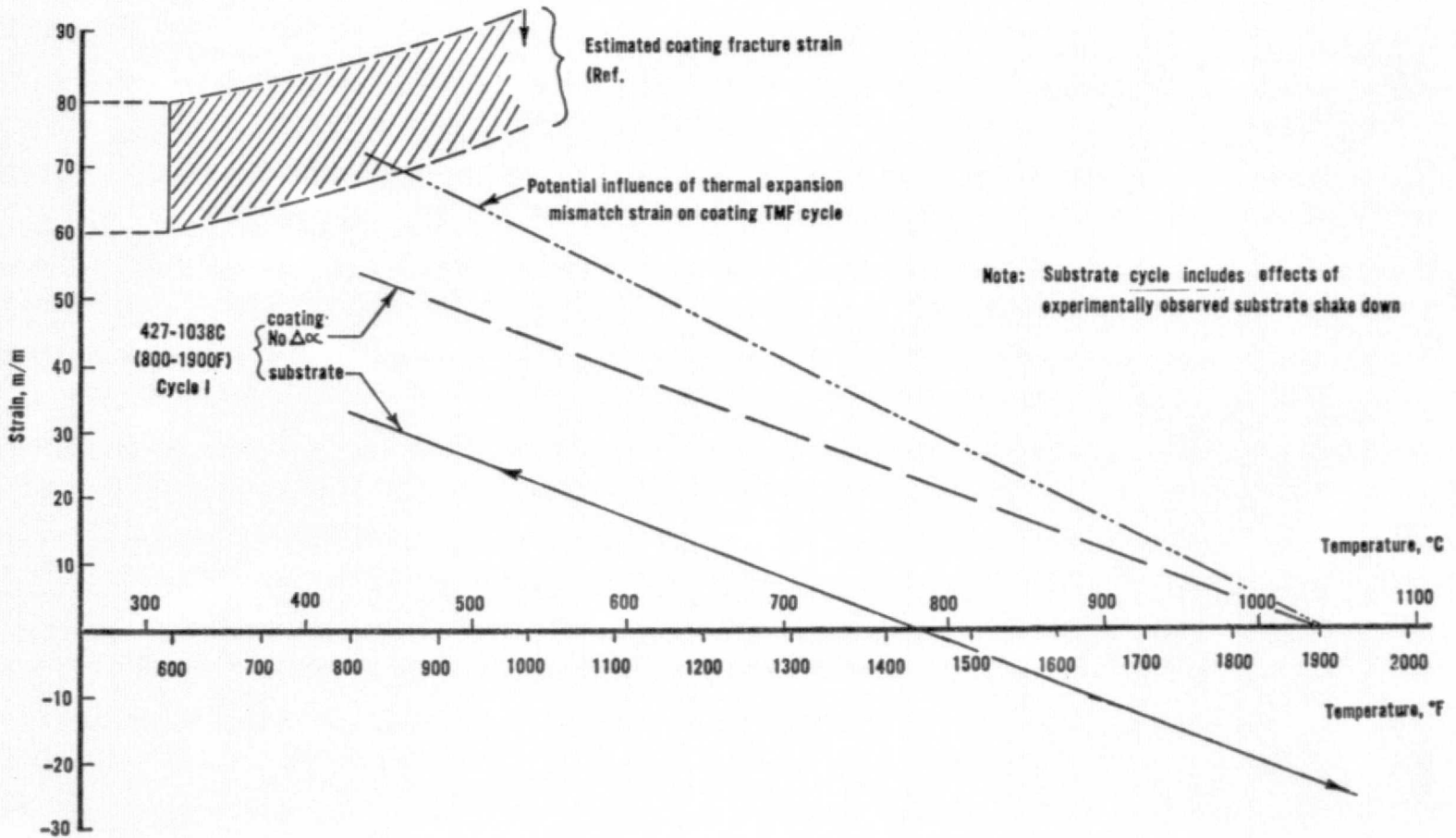
Figure 32 Potential influence of differential coating shake down and differential thermal expansion on thermomechanical strain experienced by coating
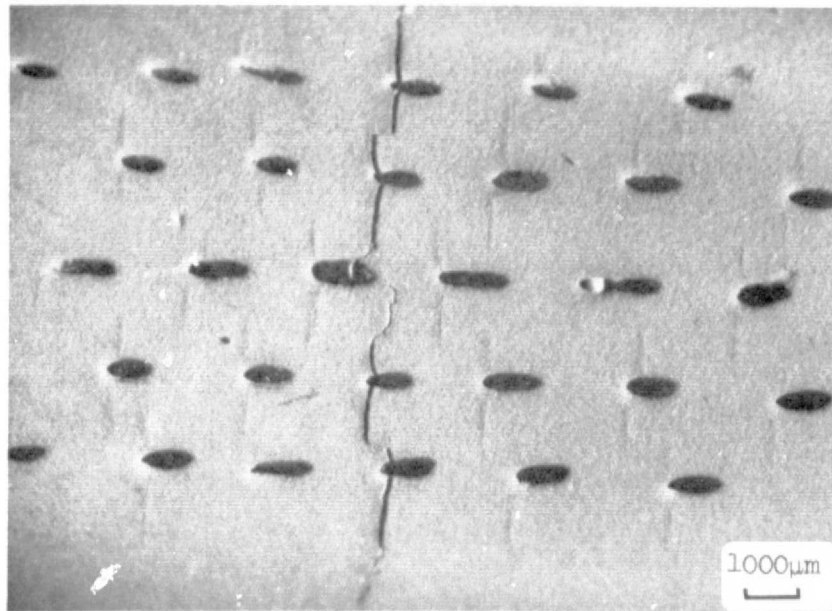
a) Specimen A76-128 surface view

(stress axis) ←→
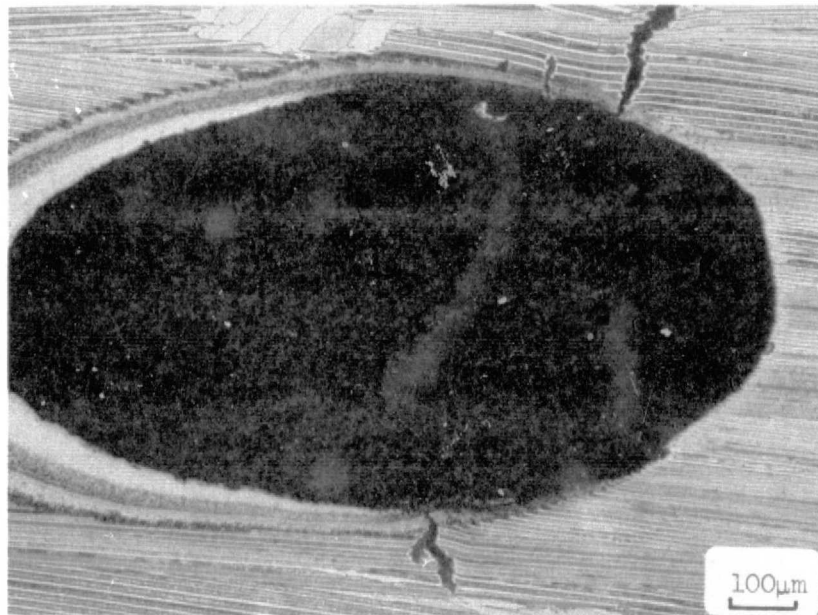
b) Specimen A76-130 polished just through coating

Figure 33 Typical cooling hole crack pattern observed on showerhead
thermomechanical fatigue specimens
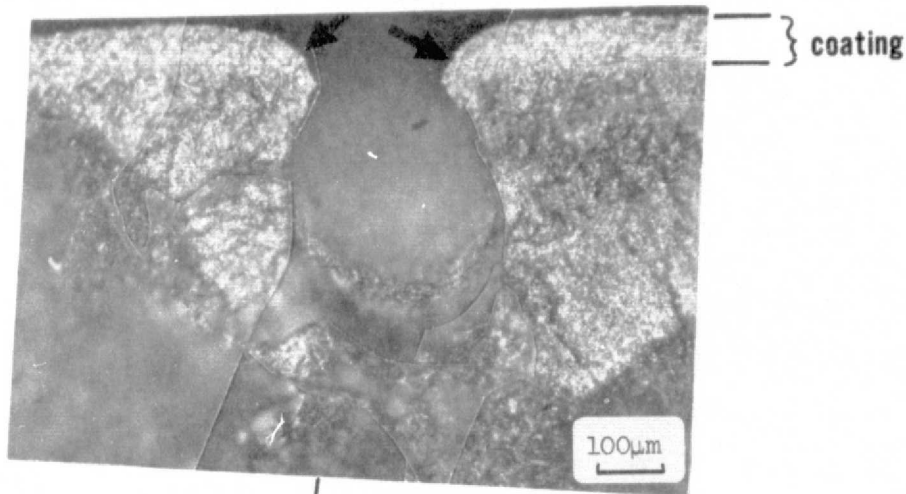
a) Crack initiation at the O.D. end of simulated cooling hole
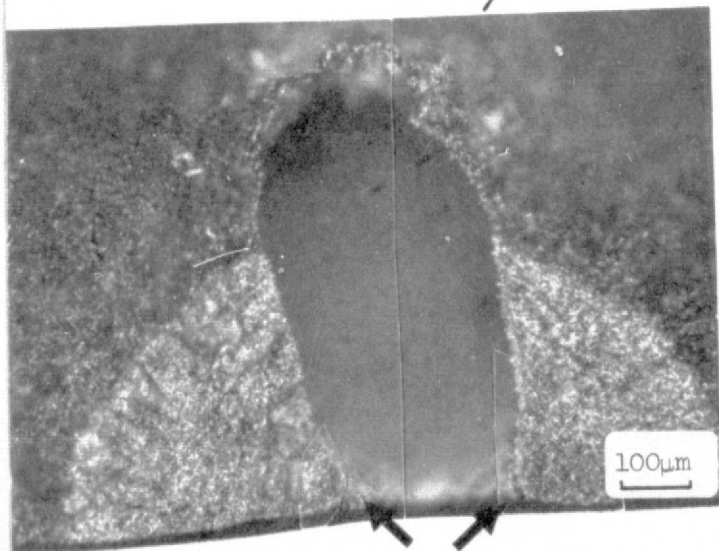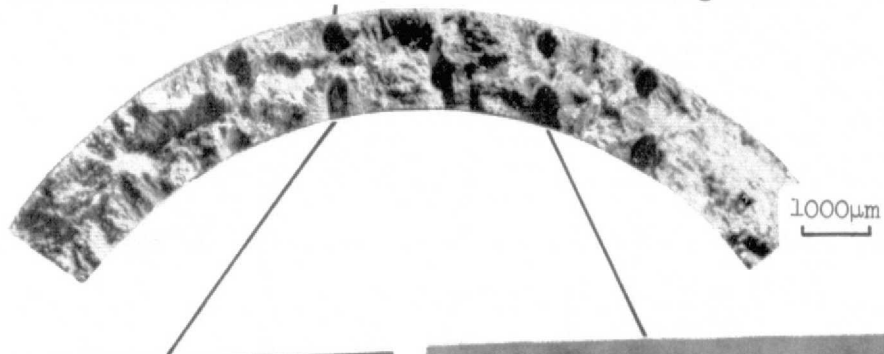
b) Crack initiation at the I.D. end of a cooling hole
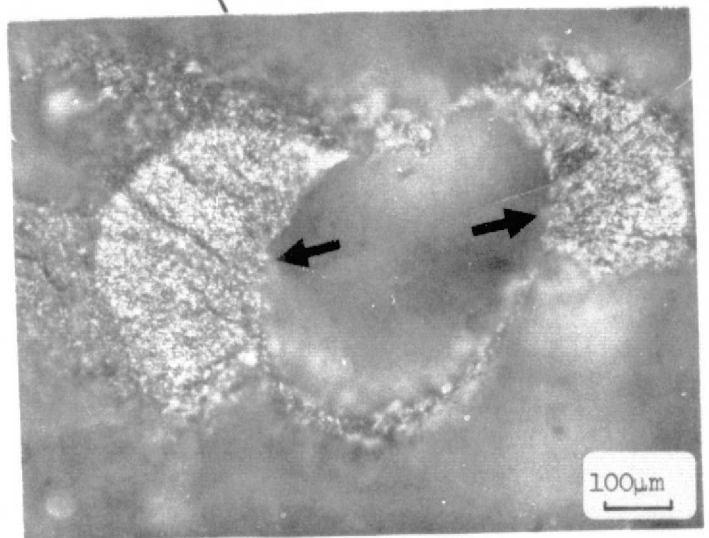
c) Crack initiation in hole barrel coating

Figure 34 Typical crack initiation sites (arrows) found on showerhead longitudinal thermomecanical fatigue specimen A76-128
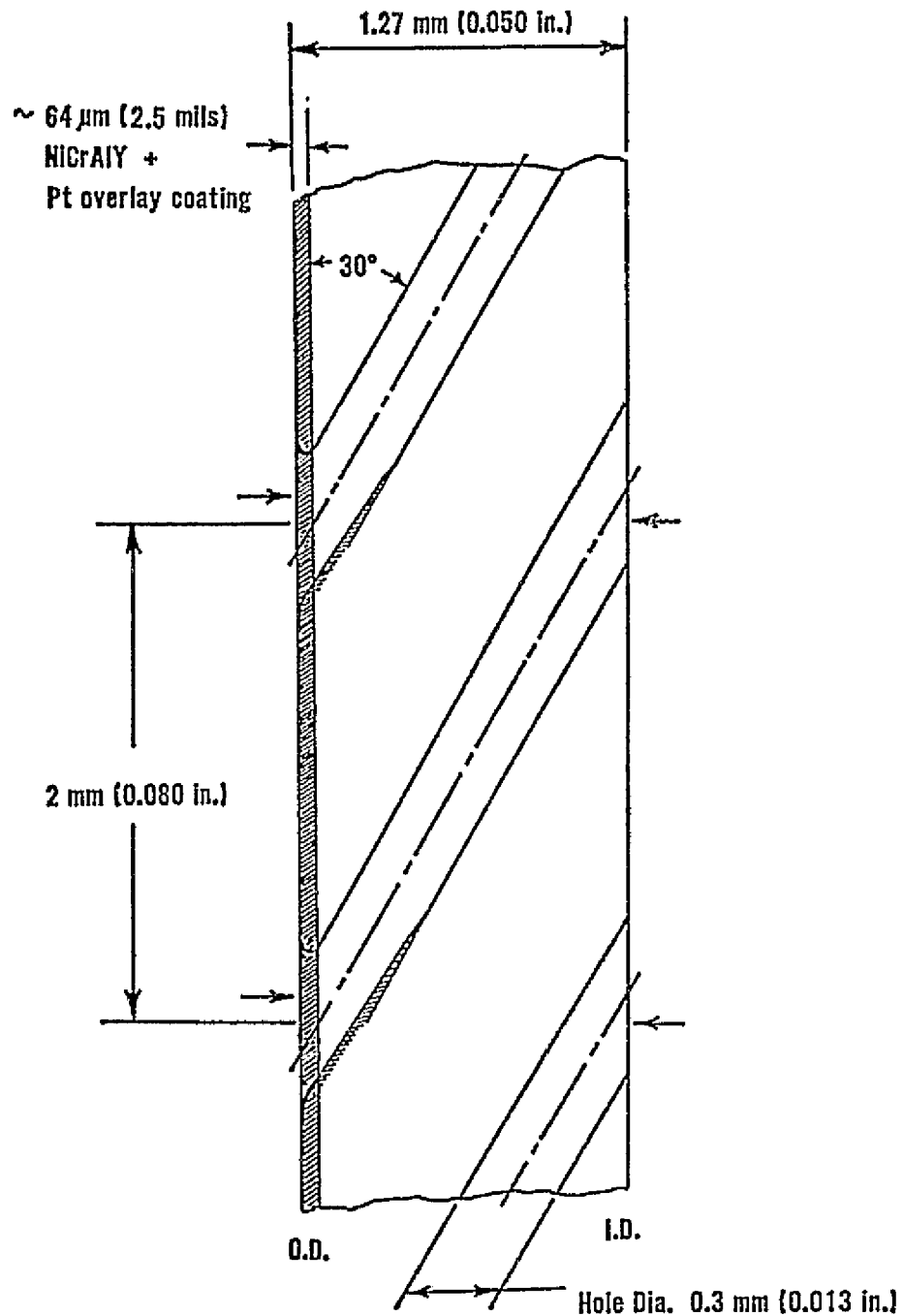
Figure 35 Cross-section through the wall of a showerhead thermomechanical fatigue specimen showing approximately coplanar location of preferred I.D. and O.D. fatigue crack initiation sites (arrows) on successive holes along specmen axis
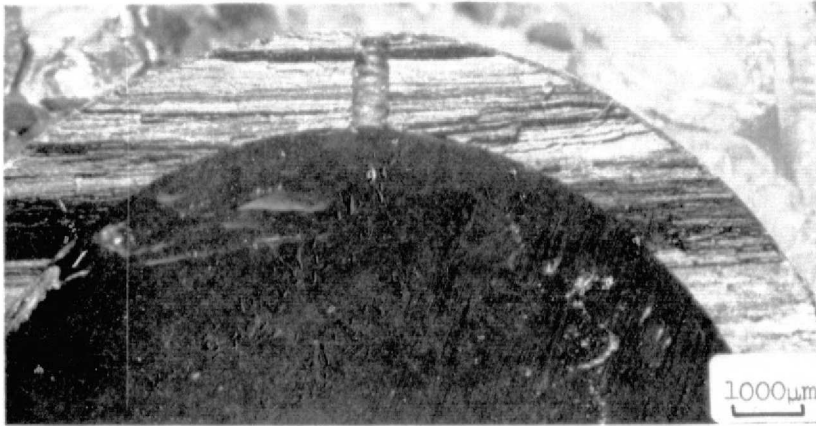
Figure 36 Fracture surface of transverse specimen E600A containing simulated cooling hole. Tested with 471-910C (880-1670F) chordwise engine cycle (Figure 4a). Cycled 1059 cycles at 0.0018 m/m engine strain range with no indications. Uploaded and cycled for 188 cycles to failure at 0.0037 m/m. Stress axis normal to plane of photograph
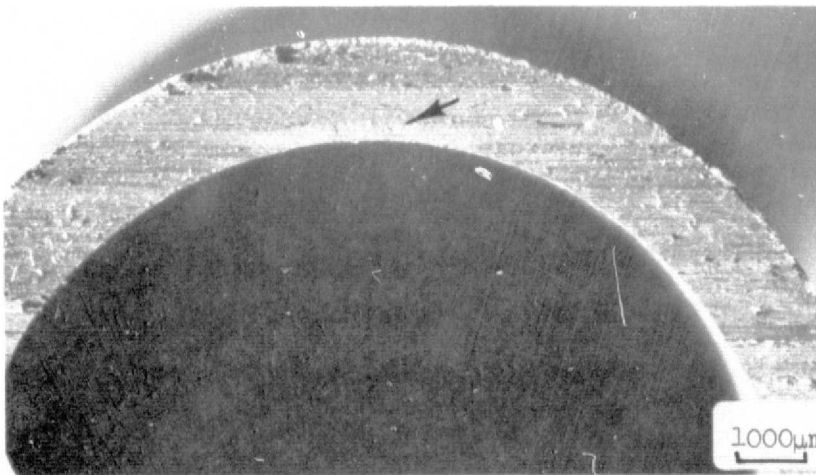
Figure 37 Fracture surface of smooth transverse specimen E576A tested 1857 cycles to failure with the 471-910C (880-1670F) chordwise engine cycle (Figure 4a) expanded to a 0.0037 m/m strain range. Arrow indicates suspected initiation site. Stress axis normal to plane of photograph

63
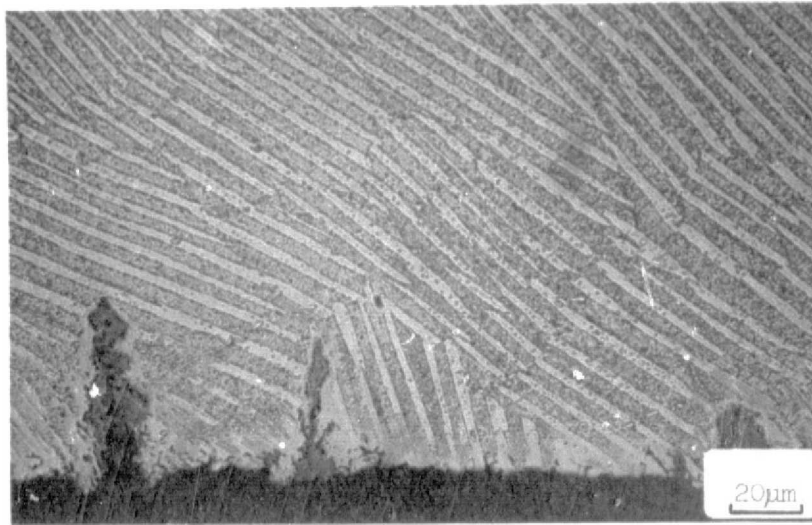
Figure 38 Secondary crack found on uncoated I.D. surface of transverse specimen E576A
tested 1857 cycles to failure with the 471-910C (880-1670F) chordwise
engine cycle expanded to a strain range of 0.0037 m/m. Stress axis horizontal
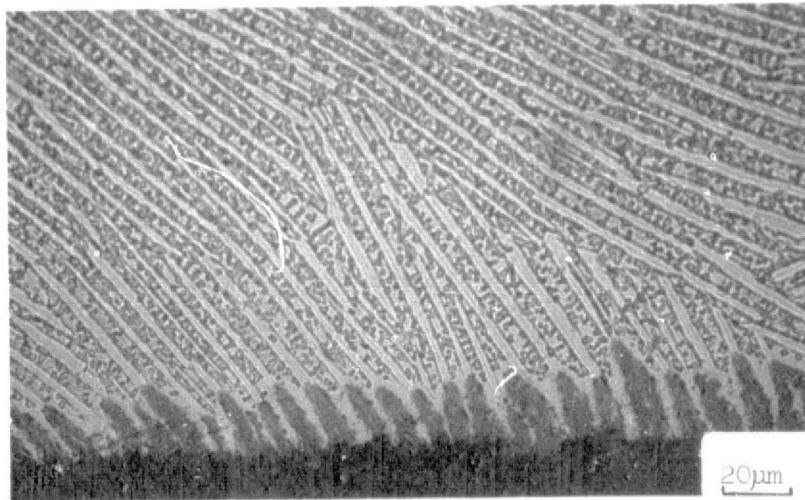
Figure 39 Selective oxidation of Ni$_3$Cb lamellae found on uncoated I.D. surface of transverse
specimen E600A tested with 471-910C (880 – 1670F) chordwise engine cycle.
Total exposure time≈22 hours
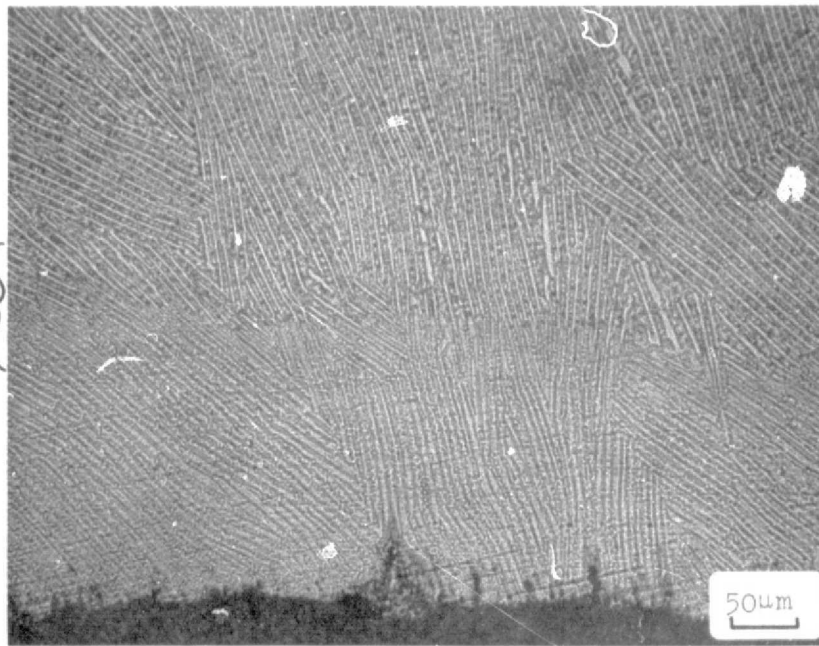
Depth of selectively oxidized zone ≈ 200 μm (≈0.008 in.)

50μm

a) Showing depth of selective oxidation and secondary cracks

10μm
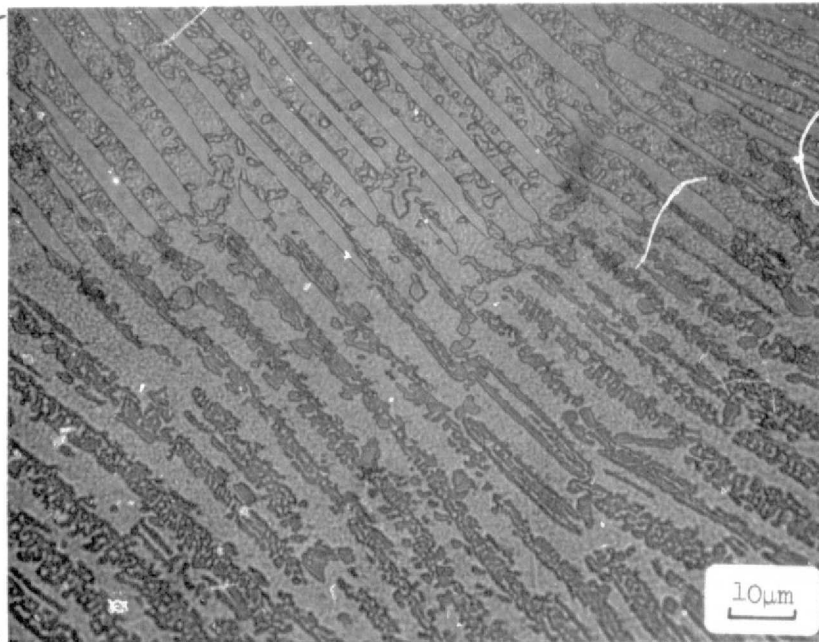
b) Detail of selective oxidation

Figure 40 Selective oxidation of Ni_3Cb lamellae found on the uncoated I.D. of specimen E582C tested 360 cycles to failure with the chordwise engine cycle (Figure 4a) expanded to a temperature range of 343-1038C (650-1900F). Total exposure time ≈ 7 hours. Stress axis horizontal
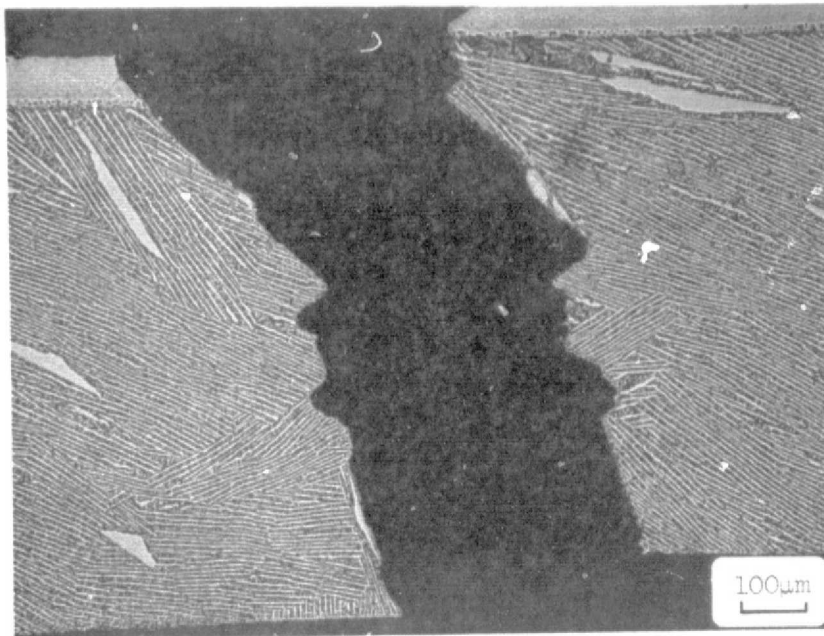
Figure 41 Fracture profile of smooth transverse specimen E580C
tested 37 cycles to failure with 427-1038C (800-1900F)
Cycle I loading. Stress axis horizontal
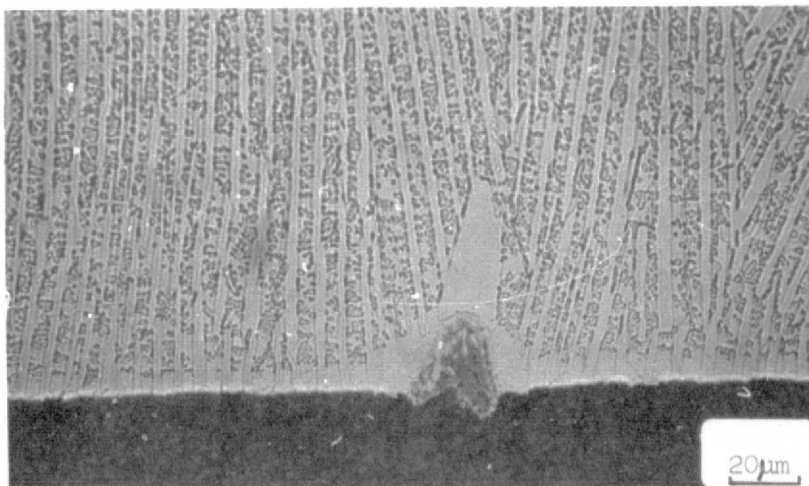
Figure 42 Selective oxidation of Ni$_3$Cb dendrite found in smooth
transverse specimen E580C. Total exposure time
≈1 hour. Stress axis horizontal
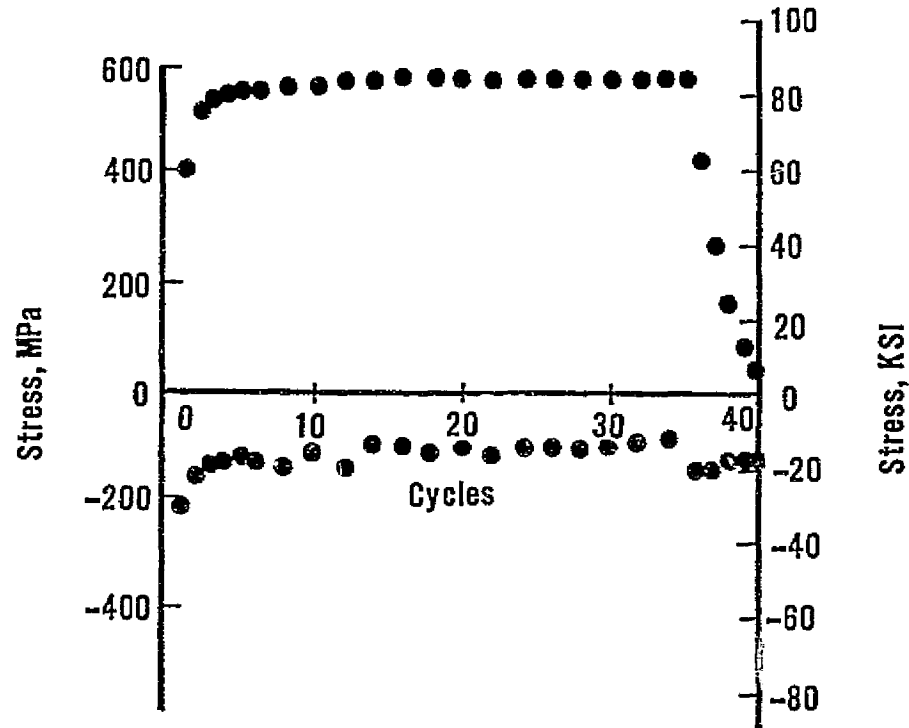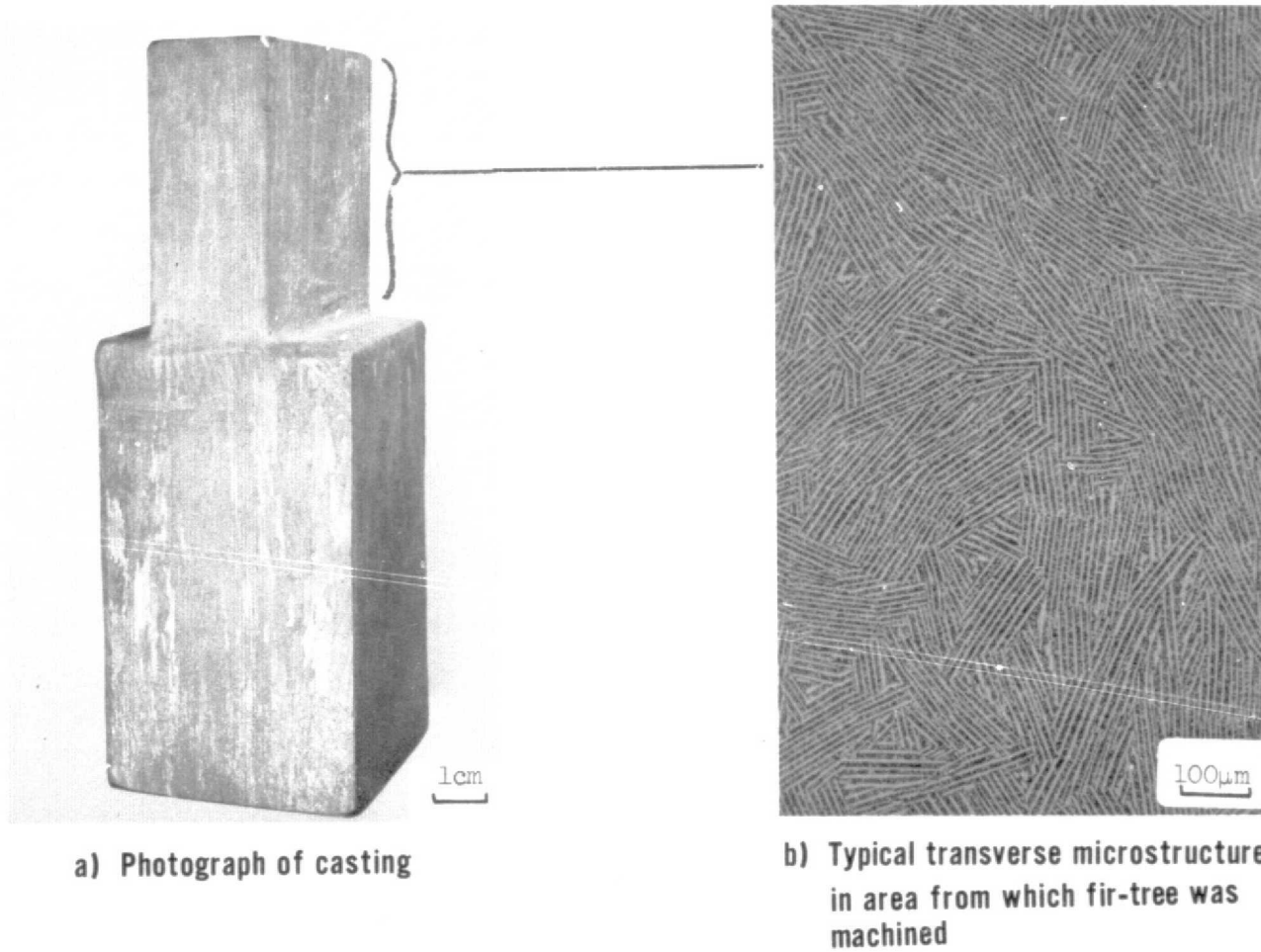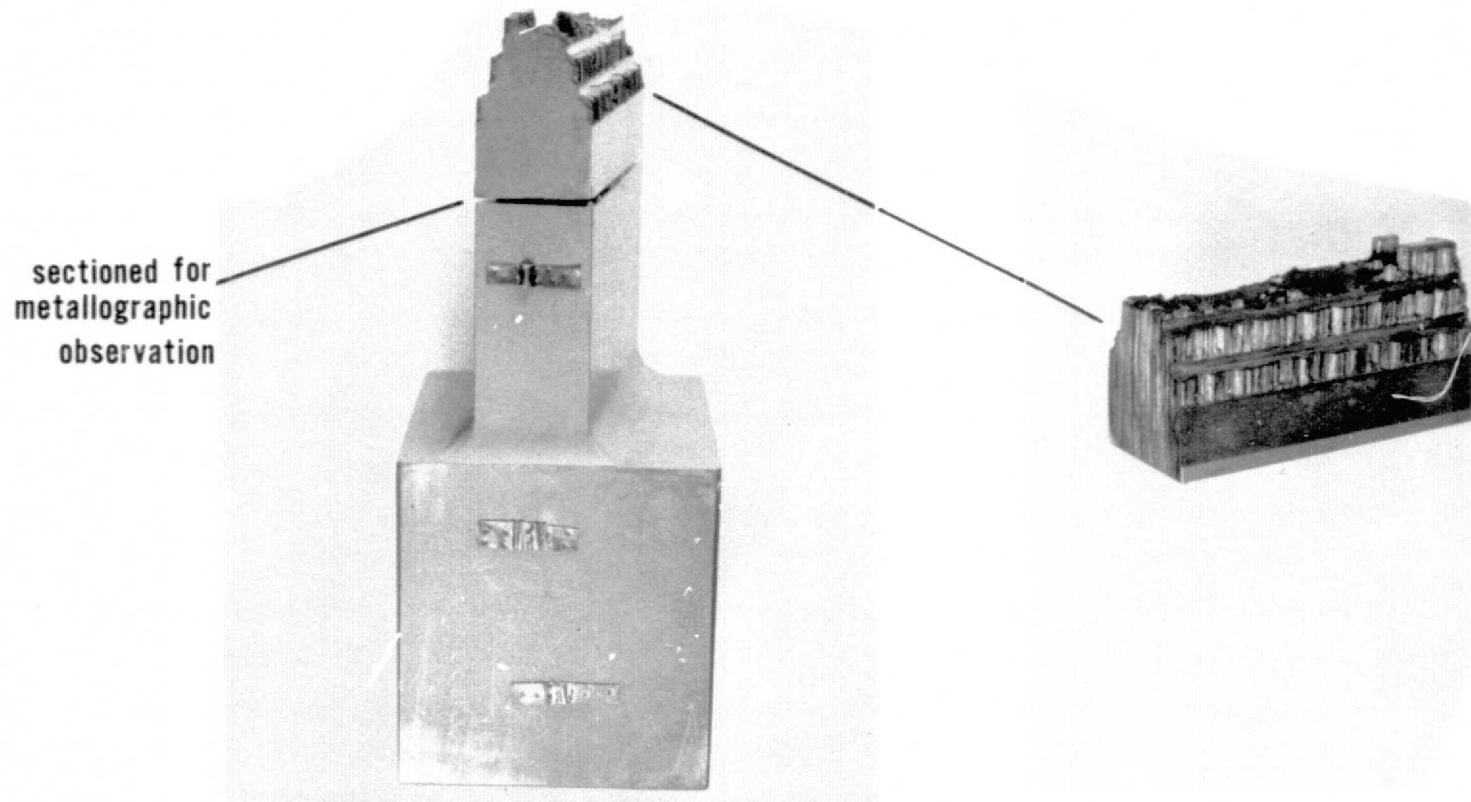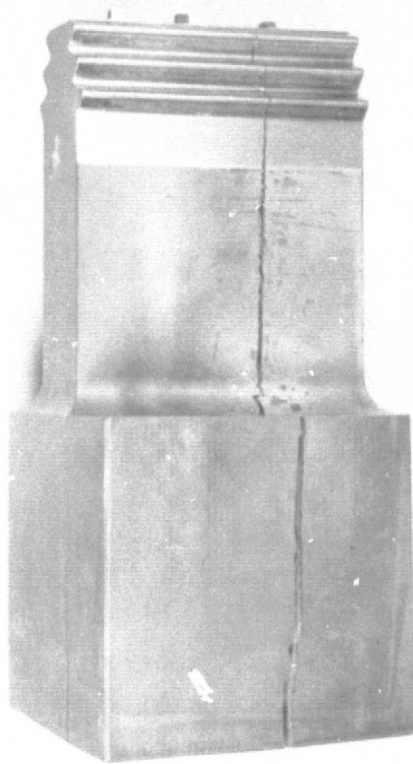
Figure 43 Shake down of Cycle I transverse specimen E580C

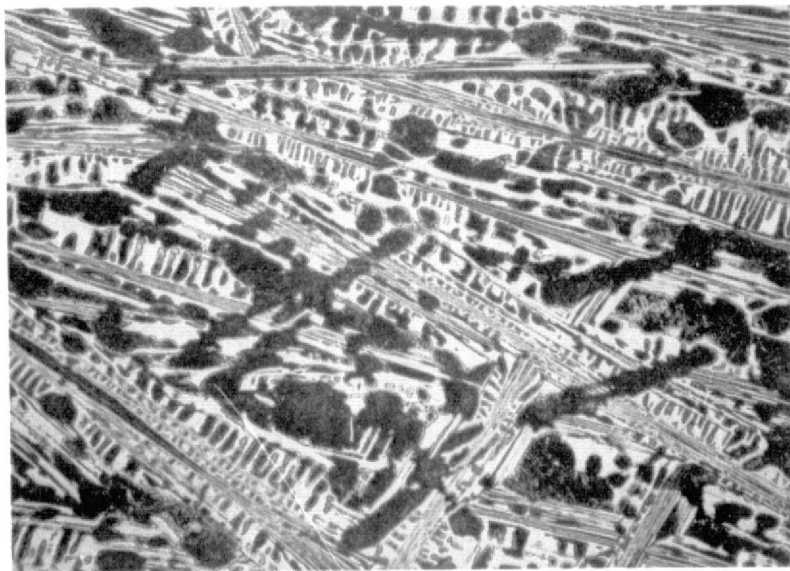a) Photograph of casting

b) Typical transverse microstructure in area from which fir-tree was machined

Figure 44 Casting used for fabrication of root subcomponent test specimen

sectioned for
metallographic
observation

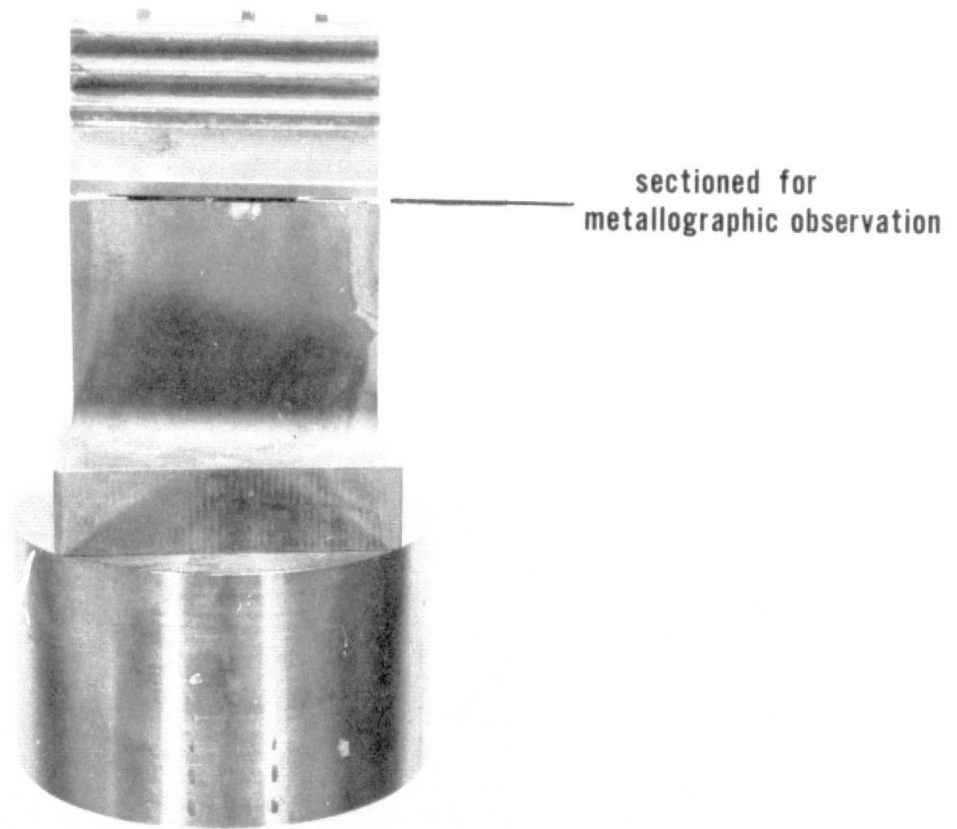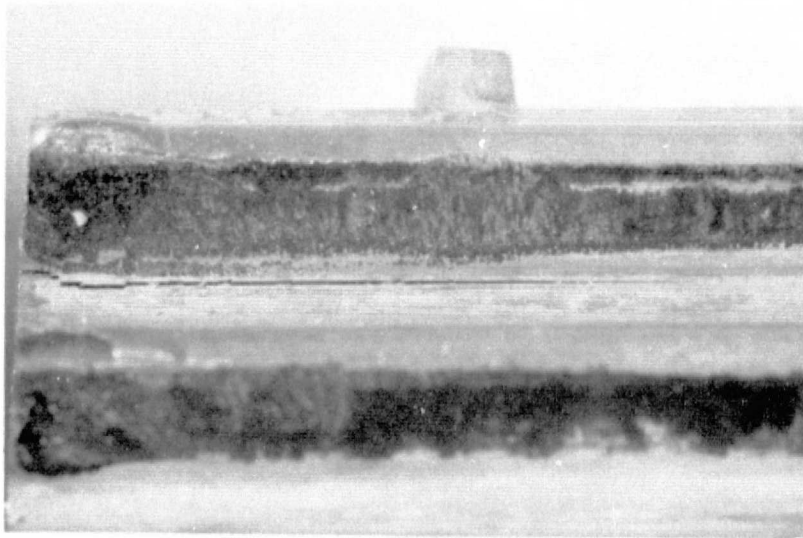Figure 45 Failed root subcomponent tensile pull-out
specimen E588

a) Split grip

b) Microstructure in grip area

Figure 46 Longitudinal splitting of eutectic grip on root subcomponent LCF test E583

sectioned for
metallographic observation

Figure 47   Shrink fit B1900 + Hf collar used to prevent splitting grip on eutectic root subcomponent LCF specimen

Figure 48 Crack found at root of bottom fir-tree serration on specimen E577 tested 11,140 cycles at 760C (1400F), 0-178 kN (0-40,000 lb)

Figure 49 Failed broach block used for root subcomponent LCF test

sectioned for
metallographic observation

1cm
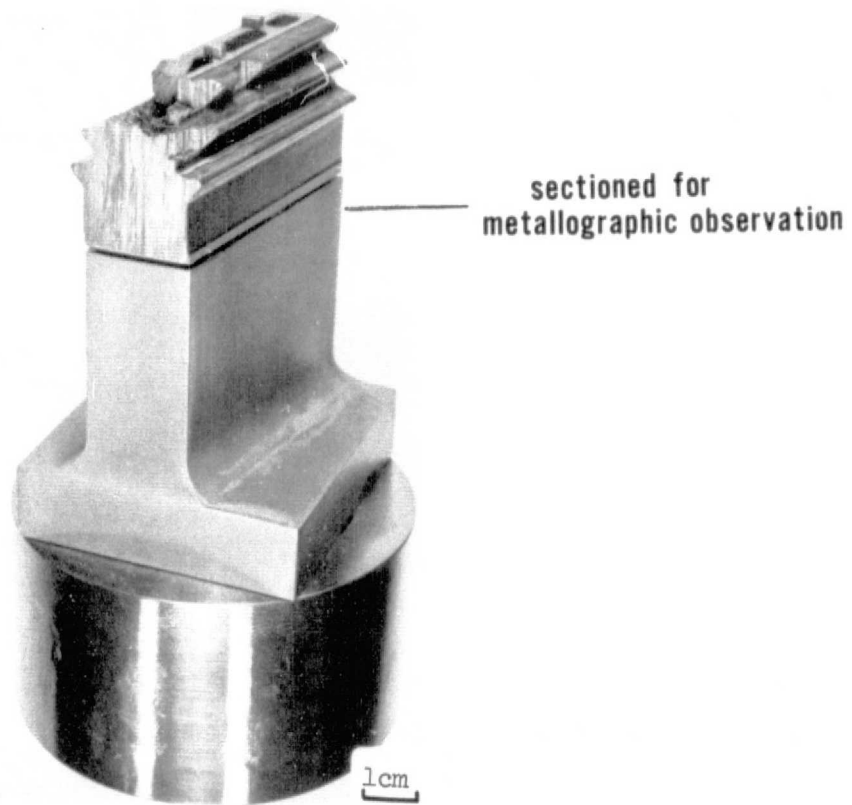
**Figure 50 Fir-tree damage caused by fatigue failure
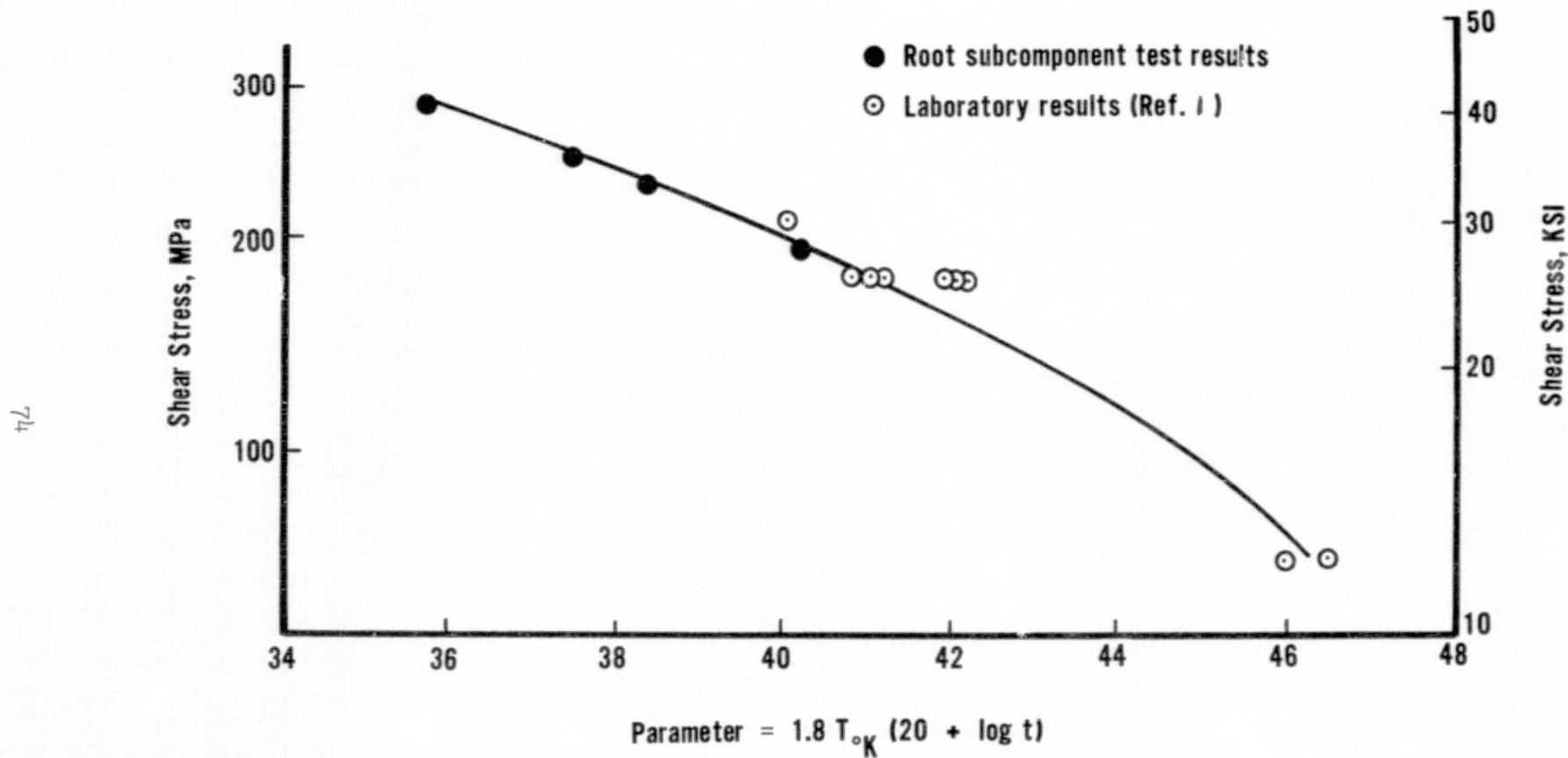of superalloy broach block**

74

Figure 51 Comparison of root subcomponent sustained load pull-out results with previous creep shear data

APPENDIX

A. MATERIAL PROPERTIES USED FOR STRESS ANALYSIS

The stress analyses performed on this program required knowledge of the thermal and elastic properties of the DS eutectic alloy. Specific properties required were heat capacity, thermal conductivity, thermal expansion coefficient, and elastic modulus. To fulfill this requirement, results obtained from tests conducted on other programs were assembled and are presented in this appendix.

Because of the unique crystallographic alignment of each phase with the direction of solidification, the physical properties of the DS eutectic are anisotropic. Since the typical transverse grain structure of fully lamellar material is essentially equiaxed and of relatively fine size ($\sim$25 to 100μm), the bulk material behaves in an axi-symmetric fashion; that is, the properties differ in the longitudinal and transverse directions, but do not vary in any direction lying in the transverse plane.

While the thermal properties of the γ/γ' phase are isotropic by virtue of the cubic crystal symmetry*, thermal conductivity and thermal expansion coefficients, being second order tensor quantities, are directional in the lower symmetry orthorhombic Ni_3Cb reinforcing phase. By virtue of the previously mentioned microstructural symmetry about the freezing direction, these two quantities can be specified for the polycrystalline DS eutectic composite by, at most, two constants measured in the longitudinal and transverse directions. As shown in Figure A-1, the thermal conductivity of the eutectic is slightly different in these two directions, while thermal expansion is, by coincidence, essentially independent of direction (Figure A-2). Heat capacity, being a scalar quantity, is independent of orientation and depends only on temperature, as shown in Figure A-3.

As shown in Figure A-4, seven elastic constants are required to fully characterize the elastic behavior of the directionally solidified lamellar eutectic. Room temperature values of these seven constants are given in Table A-I. Four of these values (E_L, E_T, ν_{LT}, and G_{LT}) were measured experimentally. The remaining three were calculated from the four measured values using the following relations

$$\nu_{TL} = \frac{E_T}{E_L} \nu_{LT}$$

$$G_{TT} = \sqrt{\frac{G_{LT} E_L}{2 (1+\nu_{LT})}}$$

$$\nu_{TT} = \frac{E_T}{2G_{TT}} - 1$$

---

*J.F. Nye, <u>Physical Properties of Crystals,</u> Oxford University Press, London, 1957.

The temperature dependence of E_L, shown in Figure A-5, was measured experimentally. The assumed temperature dependence of the remaining constants shown in this figure was scaled from the measured longitudinal modulus data.

Room Temperature Elastic Constants of D.S. γ/γ' - δ Eutectic Alloy

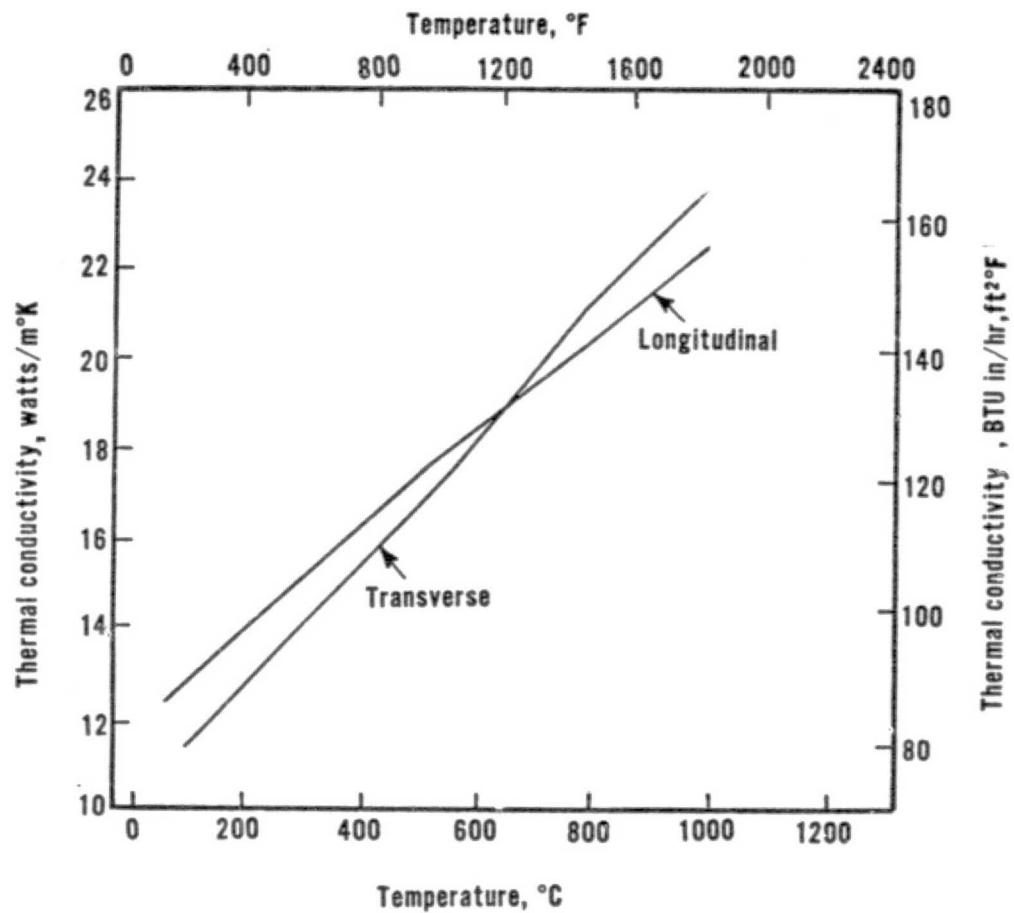| Constant	Value	
	GPa	PSI x 10^{-6}
E_L	248	36
E_T	207	30
G_{LT}	78	11.3
G_{TT}	86	12.5
ν_{LT}	0.30 (Dimensionless)	
ν_{TL}	0.25 (Dimensionless)	
ν_{TT}	0.20 (Dimensionless)	

Figure A-1 Influence of temperature and orientation on the thermal conductivity of $\gamma/\gamma' - \delta$
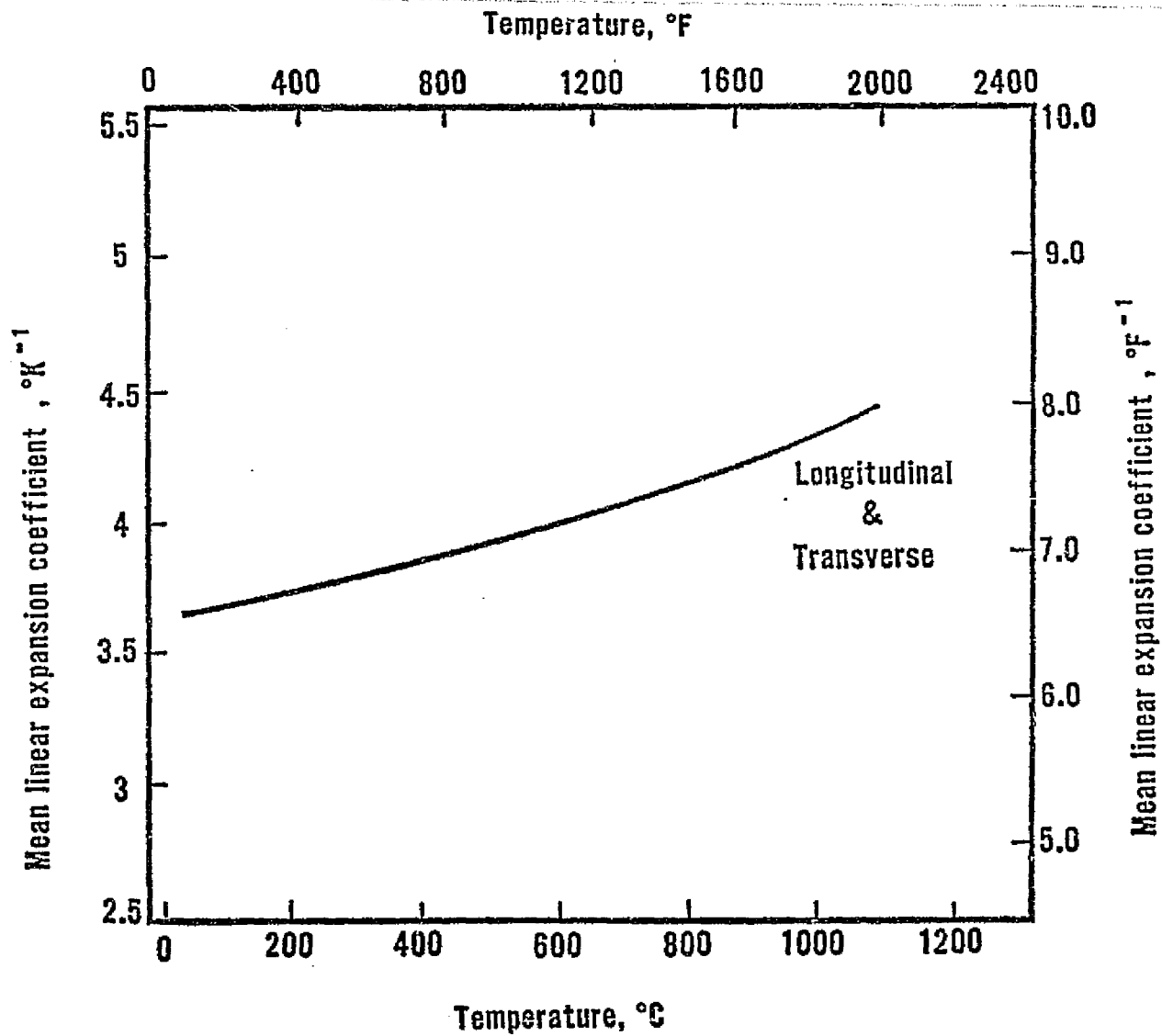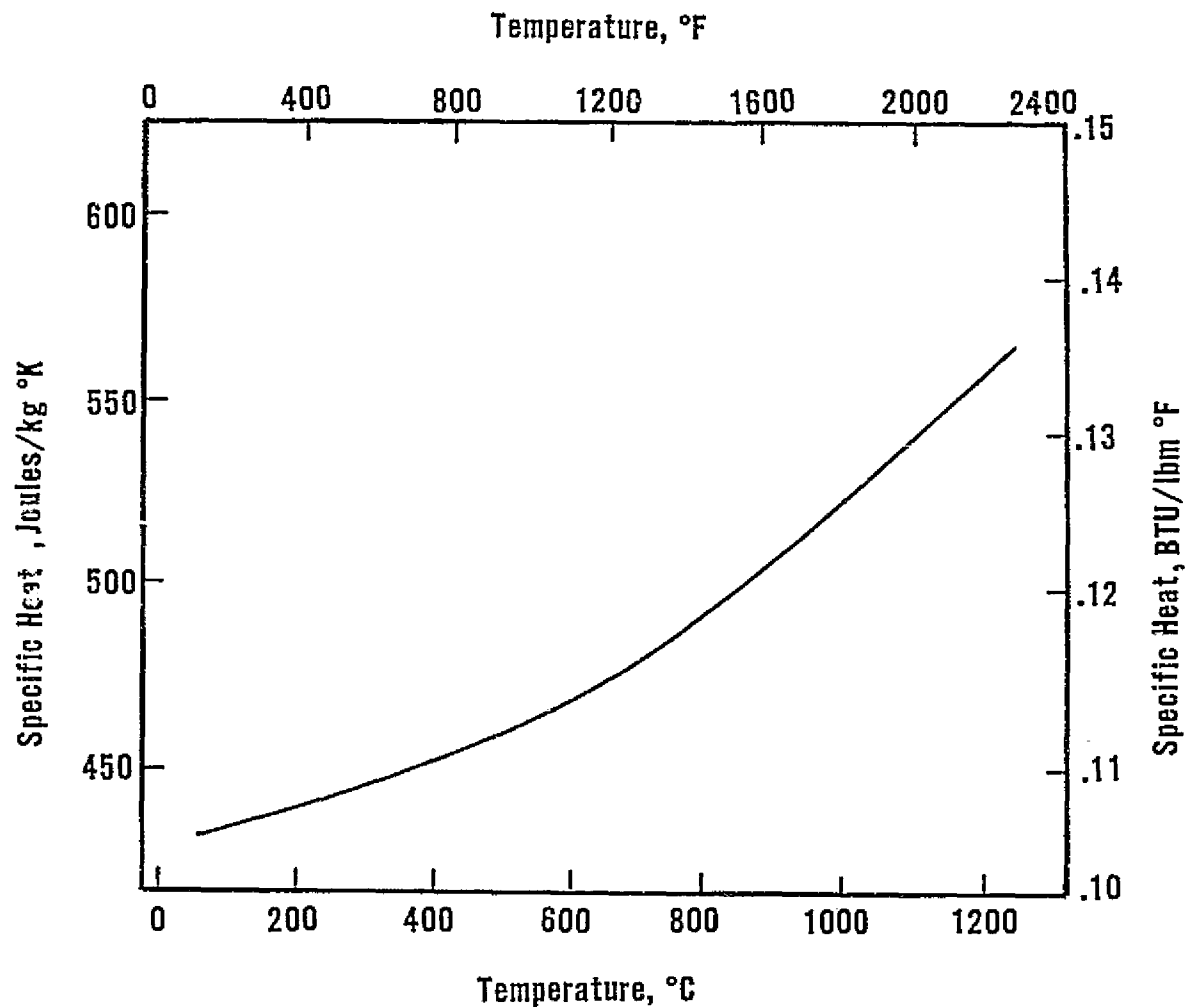
Figure A-2 Influence of temperature and orientation on the thermal expansion of $\gamma/\gamma' - \delta$ (room temperature to indicated temperature)

Figure A-3 Influence of temperature on the heat capacity of $\gamma/\gamma' - \delta$
(from 0°C to indicated temperature,

a) Definition of orthogonal axes with respect to crystal orientation

b) Definition of E_L, ν_{LT}

$E_L = \sigma_z / \epsilon_z$; $\nu_{LT} = -\epsilon_y / \epsilon_z$

c) Definition of E_T, ν_{TL}

$E_T = \sigma_y / \epsilon_y$; $\nu_{TL} = -\epsilon_z / \epsilon_y$

d) Definition of ν_{TT}

$\nu_{TT} = -\epsilon_x / \epsilon_y$

e) Definition of G_{LT}

$G_{LT} = \tau_{xz} / \epsilon_{xz}$

f) Definition of G_{TT}

$G_{TT} = \tau_{yx} / \epsilon_{yx}$
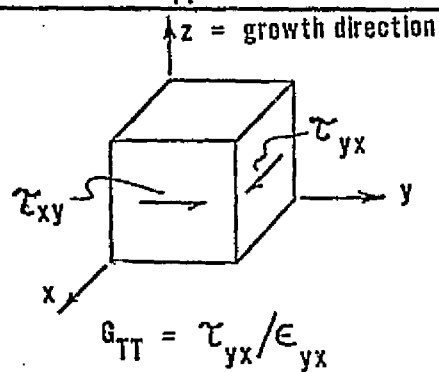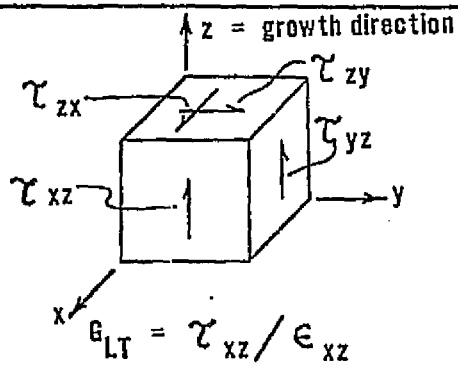
Figure A-4   Definition of elastic constants required to characterize a transversely isotropic D.S. eutectic material

81

Figure A-5 Elastic constants of 6Cr γ/γ '$-\delta$ D.S. Eutectic Alloy

(THE NUMBER IN PARENTHESES SHOWS HOW MANY COPIES
IF MORE THAN ONE ARE TO BE SENT TO AN ADDRESS.)

MR. J. ACURIO
MS 77-5
NASA LEWIS RESEARCH CTR.
21000 BROOKPARK ROAD
CLEVELAND, OHIO 44135

DR. C.W. ANDREWS
MS 49-3
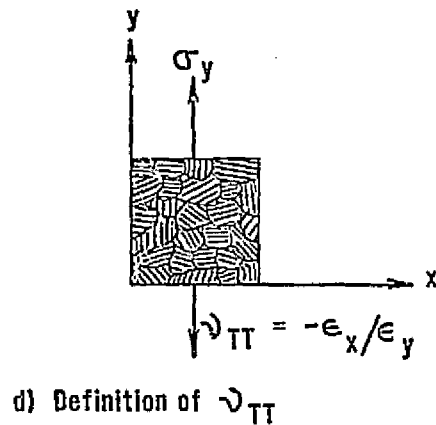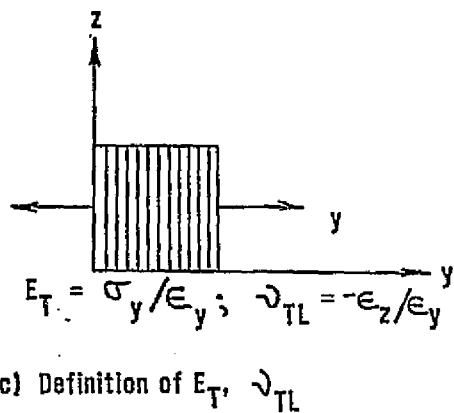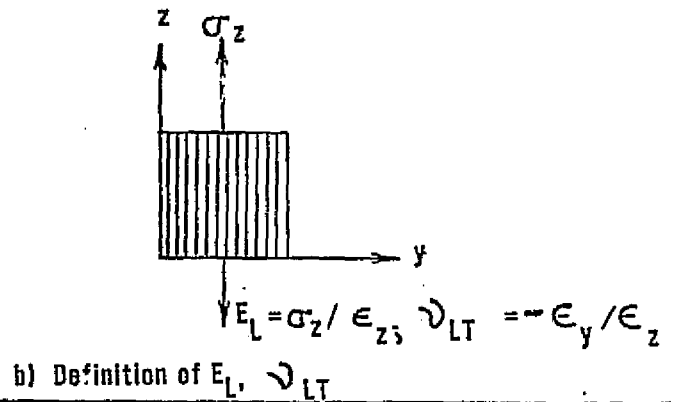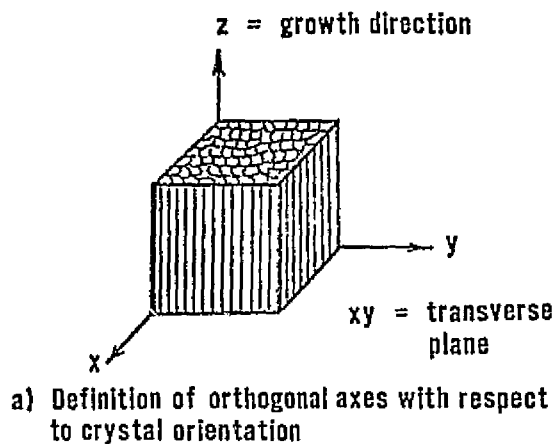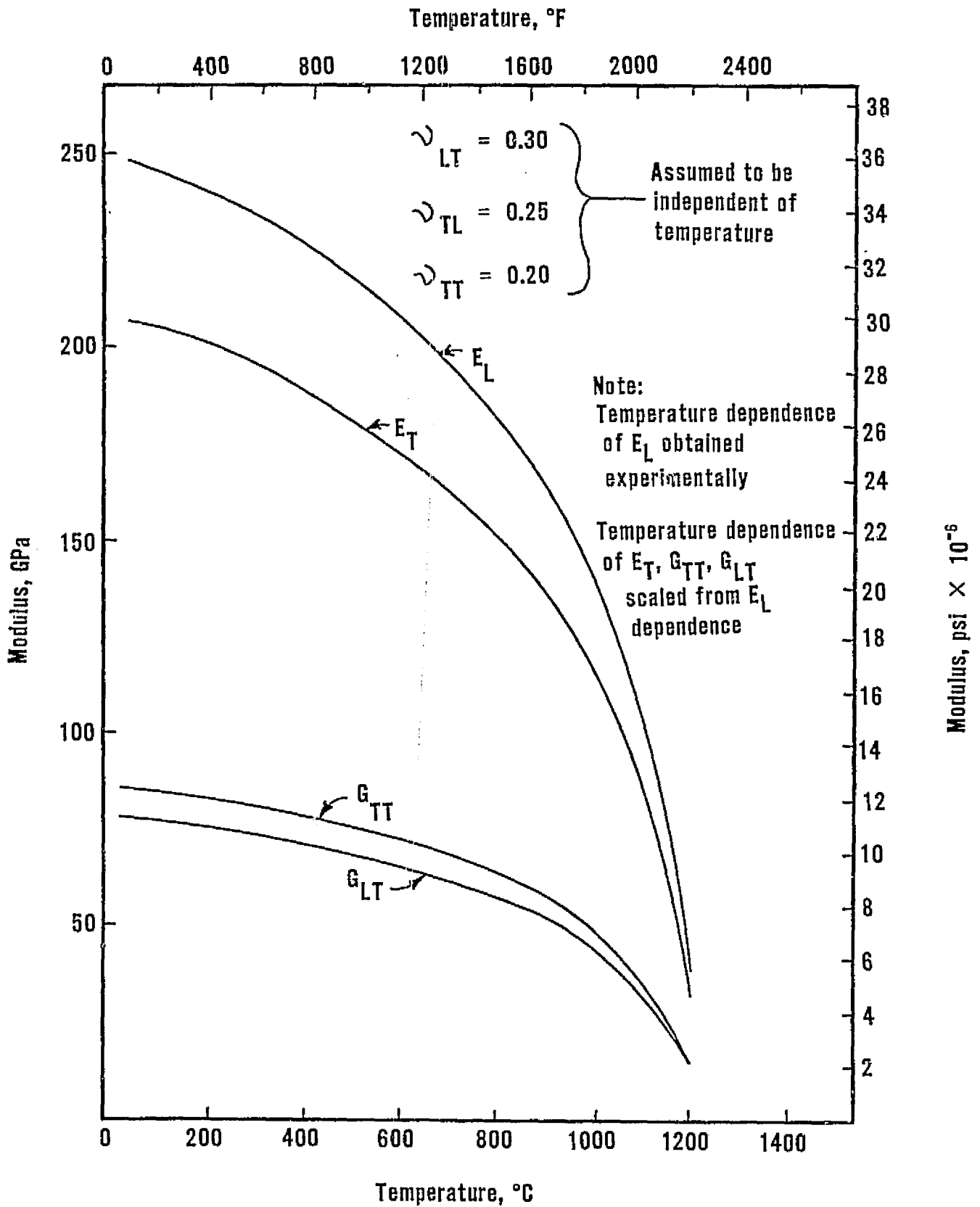NASA LEWIS RESEARCH CTR.
21000 BROOKPARK ROAD
CLEVELAND, OHIO 44135

DR. R.L. ASHBROOK
MS 49-3
NASA LEWIS RESEARCH CTR.
21000 BROOKPARK ROAD
CLEVELAND, OHIO 44135

MR. G.M. AULT
MS 3-5
NASA LEWIS RESEARCH CTR
21000 BROOKPARK ROAD
CLEVELAND, OHIO 44135

MR. C.P. BLANKENSHIP
MS 105-1
NASA LEWIS RESEARCH CTR
21000 BROOKPARK ROAD
CLEVELAND, OHIO 44135

MR. J.C. FRECHE
MS 49-1
NASA LEWIS RESEARCH CTR
21000 BROOKPARK ROAD
CLEVELAND, OHIO 44135

DR. H.R. GRAY   (10)
MS 49-3
NASA LEWIS RESEARCH CTR.
21000 BROOKPARK ROAD
CLEVELAND, OHIO 44135

MR. R.W. HALL
MS 49-1
NASA LEWIS RESEARCH CTR
21000 BROOKPARK ROAD
CLEVELAND, OHIO 44135

DR. P.H. HARF   (5)
MS 49-3
NASA LEWIS RESEARCH CTR
21000 BROOKPARK ROAD
CLEVELAND, OHIO 44135

MR. M.H. HIRSCHBERG
MS 49-1
NASA LEWIS RESEARCH CTR.
21000 BROOKPARK ROAD
CLEVELAND, OHIO 44135

DR. H.B. PROBST
MS 49-3
NASA LEWIS RESEARCH CTR.
21000 BROOKPARK ROAD
CLEVELAND, OHIO 44135

MR. A.T. SAUNDERS
MS 105-1
NASA LEWIS RESEARCH CTR
21000 BROOKPARK ROAD
CLEVELAND, OHIO 44135

MR. C.M. SCHEUERMANN
MS 49-3
NASA LEWIS RESEARCH CTR.
21000 BROOKPARK ROAD
CLEVELAND, OHIO 44135

MR. R.A. SIGNORELLI
MS 106-1
NASA LEWIS RESEARCH CTR.
21000 BROOKPARK ROAD
CLEVELAND, OHIO 44135

MR. J.W. WEETON
MS 106-1
NASA LEWIS RESEARCH CTR.
21000 BROOKPARK ROAD
CLEVELAND, OHIO 44135

MAJ. P.J. GASPERICH
AFSC LIAISON MS 501-3
NASA LEWIS RESEARCH CTR
21000 BROOKPARK ROAD
CLEVELAND, OHIO 44135

MR G. C. DEUTSCH / RW
NASA HEADQUARTERS
WASHINGTON, DC
20546

MR. J. GANGLER / RWM
NASA HEADQUARTERS
WASHINGTON, DC
20546

MR. J. MALTZ / RWM
NASA HEADQUARTERS
WASHINGTON, DC
20546

CAPT. R. DUNCO
AFML/LLC
HEADQUARTERS
WRIGHT PATTERSON AFB.
OH   45433

MR. W.J. SCHULZ
AFML/
HEADQUARTERS
WRIGHT PATTERSON AFB.
OH   45433

CAPT. D.W. ZABIEREK
AFAPL/TBP
HEADQUARTERS
WRIGHT PATTERSON AFB.
OH   45433

DR. P.J. AHEARN   AMXMR-RM
ARMY MATERIALS AND
MECHANICS RESEARCH CTR.
WATERTOWN, MA   02172

DR. J.C. HURT
ARMY RESEARCH OFFICE
BOX CM
DURHAM, NC   27706

MR. I. MACHLIN   AIR-52031B
NAVAL AIR SYSTEMS COMMAND
NAVY DEPARTMENT
WASHINGTON, DC   20361

MR. R. SCHMIDT   AIR-52031A
NAVAL AIR SYSTEMS COMMAND
NAVY DEPARTMENT
WASHINGTON, DC   20361

MR. J.W. GLATZ
NAVY DEPARTMENT
NAVAL AIR PROP. TR. CTR.
TRENTON, NJ 08628

MR. M.K. THOMAS
CODE 30231
NAV. AIR DEV. CENTER
WARMINSTER, PA 18974

DR. J.P. GUDAS
NAVY DEPARTMENT
NAVAL SHIP R&D CENTER
ANNAPOLIS, MARYLAND 21402

DR. B. MCDONALD
CODE 471, ONR
DEPARTMENT OF THE NAVY
ARLINGTON, VA   22217

MR. J.R. LANE
  MATERIALS ADV. BD.
  NAT. ACAD. OF SCIENCES
  2101 CONSTITUTION AVE.
  WASHINGTON, DC   20418

MR. M.E. BOYER
  AM. SOCIETY FOR METALS
  METALS PARK
  NOVELTY, OH   44073

MCIC
  BATTELLE MEMORIAL INST.
  505 KING AVENUE
  COLUMBUS, OHIO 43201

DR. J.K. TIEN
  HENRY KRUMB SCH. OF MINES
  COLUMBIA UNIVERSITY
  NEW YORK, NY   10027

PROF. A. LAWLEY
  DEPT. OF METALL. ENGRG.
  DREXEL UNIVERSITY
  PHILADELPHIA, PA
                19104

DR. D.L. ALBRIGHT
  DEPT. MET. & MATL. ENGRG.
  ILL. INST. OF TECHN.
  CHICAGO, IL   60616

PROF. J.D. VERHOEVEN
  DEPARTMENT OF METALLURGY
  IOWA STATE UNIVERSITY
  AMES, IOWA   50010

DR. W.B. KRAFT
  DEPT. MET. & MATL. SCI.
  LEHIGH UNIVERSITY
  BETHLEHEM, PA 18015

DR. C.W. SPENCER
  MATERIALS ADV. ED.
  NAT. ACAD. OF SCIENCES
  2101 CONSTITUTION AVE.
  WASHINGTON, DC   20418

MR. D.J. MAYKUTH
  BATTELLE MEMORIAL INST.
  COBALT INFORMATION CENTER
  505 KING AVENUE
  COLUMBUS, OH   43201

DR. M.S. SELTZER
  BATTELLE MEMORIAL INST.
  505 KING AVENUE
  COLUMBUS, OHIO 43201

MR. T.Z. KATTAMIS
  SCHOOL OF ENGINEERING
  UNIVERSITY OF CONNECTICUT
  STORRS, CT   06268

MR. A.T. CHAPMAN
  GEORGIA INST. OF. TECHN.
  ATLANTA, GA   30330

DR. R.A. GOTTSCHALL
  UNIVERSITY OF ILLINOIS
  URBANA, IL   61801

DR. W. HERTZBERG
  DEPT. MET. & MATL. SCI.
  LEHIGH UNIVERSITY
  BETHLEHEM, PA 18015

PROF. M.C. FLEMINGS
  DEPT. OF METALLURGY
  MASS. INST. OF TECHNOLOGY
  CAMBRIDGE, MA 02139

PROF. T.H. COURTNEY
  MICHIGAN TECHNOLOGICAL
  UNIVERSITY
  HOUGHTON, MI 48602

PROF. N.S. STOLOFF
  RENSSELAER POLYTECHNICAL
                INSTITUTE
  TROY, NY   12100

MR. L.J. FIEDLER
  AVCO LYCOMING DIV.
  550 S.MAIN STREET
  STRATFORD, CT 06497

DR. S.T. WLODEK
  STELLITE DIVISION
  CABOT CORPORATION
  1020 W. PARK AVE
  KOKOMO, IN 46901

MR. H. MORROW
  CLIMAX MOLYBDENUM CORP.
  1, GREENWICH PLACE
  GREENWICH, CT 06830

DR. M.G. BENZ
  CRD
  GENERAL ELECTRIC COMPANY
  P.O. BOX 8
  SCHENECTADY, N.Y. 12301

DR. M.F. HENRY
  CRD
  GENERAL ELECTRIC COMPANY
  P.O. BOX 8
  SCHENECTADY, N.Y. 12301

LIBRARY
  ADVANCED TECHNOLOGY LAB
  GENERAL ELECTRIC COMPANY
  SCHENECTADY, NY 12345

DR. S.A. DAVID
  DEPT. OF METALLURGY
  UNIVERSITY OF PITTSBURGH
  PITTSBURGH, PA 15213

DR. T.T. COURTNEY
  UNIVERSITY OF TEXAS
  MATLS.SCI. LAB.
  AUSTIN, TX 78712

MR. B. GOLDBLATT
  AVCO LYCOMING DIV.
  550 S.MAIN STREET
  STRATFORD, CT 06497

DR. D.R. MUZYKA
  CARPENTER TECHNOLOGY CORP
  RES. & DEV. CENTER
  P.O. BOX 662
  READING, PA 19603

DR. R.F. KIRBY
  CHIEF, MATERIALS ENG.
  GARRETT AIRESEARCH
  402 S. 36TH STREET
  PHOENIX, AB 85034

DR. M.F.X. GIGLIOTTI
  R. & D. CENTER
  GENERAL ELECTRIC COMPANY
  P.O. BOX 8
  SCHENECTADY, N.Y. 12301

MR. J.L. WALTER
  CRD
  GENERAL ELECTRIC COMPANY
  P.O. BOX 8
  SCHENECTADY, N.Y. 12301

TECHN. INFORMATION CENTER
  AEG
  GENERAL ELECTRIC COMPANY
  CINCINNATI, OHIO 45215

DR. P. ALDRED
AEG/GED
GENERAL ELECTRIC COMPANY
CINCINNATI, OHIO 45215

MR. R.W. SMASHEY
AEG/GED
GENERAL ELECTRIC COMPANY
CINCINNATI, OHIO 45215

LIBRARY
MATERIALS SCIENCE LAB.W5
DETROIT DIESEL ALLISON
GENERAL MOTORS
INDIANAPOLIS,IN 46206

DR. A. CHALDER
HOWMET CORPORATION
MISCO DIVISION
ONE MISCO DRIVE
WHITEHALL,MICHIGAN 49461

DR. J. BENJAMIN
INTERNATIONAL NICKEL CO.
MERICA RESEARCH LAB
STERLING FORREST
SUFFERN, NY 10901

DR. G. GARMONG
ROCKWELL INTERNATIONAL
SCIENCE CENTER
THOUSAND OAKS, CALIFORNIA
91360

DR. T. PIWONKA
MATERIALS TECHNOLOGY
TRW EQUIPMENT GROUP
23555 EUCLID AVENUE
CLEVELAND, OHIO 44117

DR. E.A. STEIGERWALD
TRW METALS DIVISION
MINERVA, OH 44657

DR. J.W. SEMMEL
AEG/GED
GENERAL ELECTRIC COMPANY
CINCINNATI, OHIO 45215

DR. M. HERMAN
DETROIT DIESEL ALLISON DV
P.O. BOX 894
INDIANAPOLIS, IN 46206

MR. E.J. CARROZZA
HOWMET CORPORATION
AUSTENAL DIVISION
DOVER, NJ 07801

DR. R.F. DECKER
INTERNATIONAL NICKEL CO.
ONE NEW YORK PLAZA
NEW YORK, NY 10004

DR. L. KAUFMAN
MANLABS, INC
21 ERIE STREET
CAMBRIDGE, MA 02139

DR. W. SUTTON
SPECIAL METALS
CORPORATION
NEW HARTFORD, N.Y. 13413

LIBRARY
MATERIALS TECHNOLOGY
TRW EQUIPMENT GROUP
23555 EUCLID AVENUE
CLEVELAND,OH 44117

MR. R.W. FAWLEY
WILLIAMS RESEARCH CORP.
2280 W. MAPLE ROAD
WALLED LAKE, MI 48088

M & S DIVISION FILES
MS 49-1
NASA LEWIS RESEARCH CTR
21000 BROOKPARK ROAD
CLEVELAND, OHIO 44135

CONTRACTS SECTION B
MS 500-313
NASA LEWIS RESEARCH CTR
21000 BROOKPARK ROAD
CLEVELAND, OH 44135

REPORT CONTROL OFFICE
MS 5-5
NASA LEWIS RESEARCH CTR
21000 BROOKPARK ROAD
CLEVELAND, OHIO 44135

LIBRARY
NASA
GODDARD SPACE FLIGHT CTR
GREENBELT, MARYLAND 20771

LIBRARY
NASA
MARSHALL SPACE FLIGHT
CENTER
HUNTSVILLE, AL 35812

LIBRARY - ACQUISITIONS
JET PROPULSION LAB.
4800 OAK GROVE DRIVE
PASADENA, CA 91102

LIBRARY - REPORTS
MS 202-3
NASA AMES RESEARCH CENTER
MOFFETT FIELD, CA 94035

DEFENCE DOCUMENTATION CTR
CAMERON STATION
5010 DUKE STREET
ALEXANDRIA, VIRGINIA
22314

MR. J.P. MERUTKA
MS 49-3
NASA LEWIS RESEARCH CTR.
21000 BROOKPARK ROAD
CLEVELAND, OHIO 44135

LIBRARY   (2)
MS 60-3
NASA LEWIS RESEARCH CTR
21000 BROOKPARK ROAD
CLEVELAND, OHIO 44135

TECHNOLOGY UTILIZATION
MS 3-19
NASA LEWIS RESEARCH CTR
21000 BROOKPARK ROAD
CLEVELAND, OHIO 44135

LIBRARY   MS 185
NASA
LANGLEY RESEARCH CENTER
LANGLEY FIELD, VA 23365

TECHNICAL LIBRARY / JM6
NASA
JOHNSON SPACE CENTER
HOUSTON, TX 77058

LIBRARY
NASA
DRYDEN FLIGHT RES. CTR.
P.O. BOX 273
EDWARDS, CA 93523

ACCESSIONING DEPT   (10)
NASA SCIENTIFIC & TECHN.
INFORMATION FACILITY
BOX 8757
BALTIMORE, MD 21240

TECHNICAL LIBRARY
AFML/LAM
HEADQUARTERS
WRIGHT PATTERSON AFB,
OH 45433

TECHNICAL REPORTS LIBRARY
ERDA
WASHINGTON, DC
            20545

MR. P.T. BIZON
            MS 49-1
NASA LEWIS RESEARCH CTR
21000 BROOKPARK ROAD
CLEVELAND, OHIO 44135

Corten, Prof H T
   321A Talbot Lab
   Univ of Ill
   Urbana, IL 61801

Creighton, Dr D L
   Mech & Aero Engrg Dept
   Univ of Missouri

DR. G.R. HALFORD
            MS 49-1
NASA LEWIS RESEARCH CTR.
21000 BROOKPARK ROAD
CLEVELAND, OHIO 44135

DR. R.L. DRESHFIELD
            MS 105-1
NASA LEWIS RESEARCH CTR.
21000 BROOKPARK ROAD
CLEVELAND, OHIO 44135

Dieter, Dr George E
   Dir - Proc Res Inst
   Carnegie-Mellon Univ
   Scaife Hall
   Pittsburgh, PA 15213

Esztergar, E P
   442 Westbourne St
   La Jolla, CA 92037

MR. T.K. GLASGOW
            MS 49-3
NASA LEWIS RESEARCH CTR.
21000 BROOKPARK ROAD
CLEVELAND, OHIO 44135

MR. S.J. GRISAFFE
            MS 49-3
NASA LEWIS RESEARCH CTR
21000 BROOKPARK ROAD
CLEVELAND, OHIO 44135

Findley, Prof William N
   Div of Engrg
   Box D
   Brown Univ
   Providence, RI 02912

Finnie, Prof I
   Dept Mech Engrg
   Univ of Cal
   Berkeley , CA 94720

MR. R.H. KEMP
            MS 49-3
NASA LEWIS RESEARCH CTR.
21000 BROOKPARK ROAD
CLEVELAND, OHIO 44135

MR. J.L. SHIALEK
            MS 49-3
NASA LEWIS RESEARCH CTR
21000 BROOKPARK ROAD
CLEVELAND, OHIO 44135

Freeman, William R Jr
   V.P. & Tech Director
   Howmet - Technical Ctr
   699 Benston Rd
   Whitehall, MI 49461

Fuchs, Dr Henry O
   Mech Engrg Dept
   Stanford Univ
   Stanford, CA 94305

Antolovich, Stephen D
   Dept Matl's Sci & Met Eng
   489 Rhodes Hall
   Univ of Cincinnati
   Cincinnati, OH 45221

Bates, Dr C E
   SRI
   2000 9th Ave S
   Birmingham, AL 35205

Garofalo, Dr Frank
   Inland Steel Res Lab
   3001 E Columbus Dr
   E Chicago, IN 46312

Gayley, Harry B
   DeLaval Turbine
   Nottingham Way
   Trenton, NJ 08602

Bernstein, Martin D
   Foster-Wheeler
   110 S Orange Ave
   Livingston, NJ 07039

Bluhm, Joseph I
   Army Matls & Mech Res Ctr
   Watertown, MA 02172

Gerdeen, Prof James C
   Dept of ME-EM
   Michigan Tech Univ
   Houghton, MI 49931

Gleich, David
   Arde Inc
   19 Industrial Ave
   Mahwah, NJ 07430

Boesch, W J
   Special Metals
   Middle Settlement Rd
   New Hartford, NY 13413

Cannett, Dr John T
   MET-CUT
   3980 Rosslyn Dr
   Cincinnati, OH 45209

Grady, Harold F
   Director - R&D
   AVCO - Lycoming
   550 S Main St
   Stratford, CT 06497

PROF. N.J. GRANT
   DEPT. OF METALLURGY
   MASS. INST. OF TECHNOLOGY
   CAMBRIDGE, MA 02139

Collins, Prof Jack A
   Dept of Mech Engrg
   Ohio State Univ
   206 W 18th Ave
   Columbus, OH 43210

Conrad, Dr Hans
   Anderson Hall
   Univ of Kentucky
   Lexington, KY 40506

Gross, Ellen
   1224 Washtenaw #10
   Ann Arbor, MI 48104

Grosskreutz, Dr J C
   Consultant
   Black & Veatch
   Box 8405
   Kansas City, MO 64114

87

Handlogten, Howar R
Sundstrand Aviation
4747 Harrison Ave
Rockford, IL 61101

Heydt, Gerald B
Carpenter Tech
Box 662
R&D Ctr
Reading, PA 19603

Himelblau, Harry
14206 Mulholland Dr
Los Angeles, CA 90024

Howes, Dr M A H
Metals Div
IIT Res Inst
10 W 35th St
Chicago, IL 60616

Jaske, Carl E
B C L
505 King Ave
Columbus, OH 43201

Kaplan, Dr Abner
TRW Systems Group
One Space Park, MB/2037
Redondo Beach, CA 90278

Kaye, Prof A L
Purdue Univ
Calumet Campus
2233 171st St
Hammond, IN 46323

Kleemann, W
7 Riddlewood Dr
Media, PA 19063

Herfert, R E
Northrop Corp   3771-62
3901 W Broadway
Hawthorne, CA 90250

Hillberry, Prof B M
School of Mech Engrg
Purdue Univ
W Lafayette, IN 47907

Holt, J M
MS-64
Research Ctr
Bethpage, L.I., NY 11714

Hulsizer, William R
Int'l Nickel
One New York Plaza
New York, NY 10004

Jonas, Otakar
1113 Faun Rd
Wilmington, DE 19803

Kattus, J R
Consulting Metallurgist
112 Azalea Rd
Birmingham, AL 35213

Kennedy, Dr C R
Met & Ceramics Div
O.R.N.L.
Box X
Oak Ridge, TN 37930

Koerwer, Dick
Franklin Institute
Research Labs
20th & Parkway
Philadelphia, PA 19103

Kulin, Dr S Andrew
Manlabs
21 Erie St
Cambridge, MA 01239

Laggett, Richard
Int'l Nickel
Merica Res Lab
Sterling Forest
Suffern, NY 10901

Lane, J (SAVDL-EU-TAPP)
Eustis Directorate
USAAMRDL
Fort Eustis, VA 23604

Lee, P P
22421 Philiprinn St
Woodland Hills, CA 91364

Martino, Albert A   (PE4)
Mgr, R&T Group
NAPTC
Trenton, NJ 08628

Miller, C R
Gas Turbine Res
Tech Ctr   F-1
Caterpillar Tractor
Peoria, IL 61611

Miller, G A
Bethlehem Steel
Homer Research Labs
Bethlehem, PA 18016

Miller, Dr William R
Dept of Mech Engrg
Univ of Toledo
Toledo, OH 43606

Kuo, Dr Albert S
409 Link Hall
Syracuse Univ
Syracuse, NY 13210

Laird, Dr Campbell
Met & Matl's Sci School
Univ of Penn
Philadelphia, PA 19174

Le Coff, Jesse
Catalytic Inc
Centre Square West
1500 Market St
Philadelphia, PA 19102

Little, Prof Robert E
Engrg Dept
Univ of Michigan
4901 Evergreen Rd
Dearborn, MI 48128

Meshii, Prof M
Dept Matl's Sci
Northwestern Univ
Evanston, IL 60201

Miller, Forbes M - Dir.
Wall Colmonoy
20120 John R
Detroit, MI 48203

Miller, Roy W
Atkins & Merrill, Inc
Main St
Ashland, MA 01721

Mitchell, M R
306-C Talbot Lab
TAM Dept
Univ of Illinois
Urbana, IL 61801

Moen, R G
Turbine Engrg
Nordberg Mfg
4602 N Marlborough
Milwaukee, WI 53211

Boteff, Dr J
Dept Matl's Sci & Met Eng
Location 12
Univ of Cincinnati
Cincinnati, OH 45221

O'Brien, John L
Arthur D Little
15 Acorn Park 15L/115
Cambridge, MA 02140

Packman, Prof Paul P
Box 3245 - Station B
Vanderbilt Univ
Nashville, TN 37235

Reensnyder, Harold S
Homer Research Labs
Bethlehem Steel
Bethlehem, PA 18016

Roy, Dr A   - Manager
Chrysler Corp
Box 1118   (418-19-30)
Detroit, MI 48231

Sandor, Prof Bela I
Dept Engrng Mech
2359 Engineering Bldg
Univ of Wisconsin
Madison, WI 53705

Schlatter, R
Research & Develeopment
Latrobe Steel
Box 31
Latrobe, PA 15650

Rogul, J
Dir - Matl's Engrg
Curtiss-Wright
1 Passaic St
Wood-Ridge, NJ 07075

Munse, Prof W H
2129 Civil Eng Bldg
Univ of Ill
Urbana, IL 61801

O'Donnell, Dr W J
O'Donnell & Assoc
5100 Centre Ave
Pittsburgh, PA 15232

Pelloux, Prof Regi M
M I T,   Rm 8-237
77 Mass Ave
Cambridge, MA 02139

Rostoker, Prof William
Dept Matl's Engrng
Univ of Illinois
Box   4348
Chicago, IL 60680

Rundell, Gene
Simonds Steel
Ohio St
Lockport, NY 14094

Schaefer, A O
M P C
United Engineering Center
345 E 47th St
New York, NY 10017

Schwenk, E B
300 Armistead
Richland, WA 99352

Semchyshen, Dr M
Climax Moly
1600 Huron Parkway
Ann Arbor, MI 48105

Sharpe, William N Jr
Dept Metallurgy Mechanics
and Materials Science
Mich State Univ
E Lansing, MI 48624

Sines, Prof George
Matl's Dept, Engineering
U C L A
Los Angeles, CA 90024

Smith, Prof G V
104 Berkshire Rd
Ithica, NY 14850

Snow, Alfred L
12 Nottingham Dr
Greensburg, PA 15601

Stephens, Prof Ralph I
Matl's Engrg Div
Univ of Iowa
Iowa City, IA 52242

Straub, Edward Jr
Fairchild Republic
Showalter Rd
Hagerstown, MD 21740

Tagart, Sam W Jr
Nuclear Services Corp
1700 Dell Ave
Cambell, CA 95008

Semonek, M P
Int'l Harvester
5400 Dearborn Pkwy
Downers Grove, IL 60515

Sherby, Prof Oleg D
Dept of Matl's Sci
Stanford Univ
Stanford, CA 94305

Slot, Dr T
2 Yorkshire Terrace
Clifton Park, NY 12065

Smith, Dr Thomas E Jr
Mgr, Research Analysis
Waukesha Engine Div
St Paul Ave
Waukesha, WI 53186

Starkey, W L
Mech Engrg Dept
206 W 18th Ave
Ohio State Univ
Columbus, OH 43110

Stetson, Alvin R
Solar Division
2200 Pacific Highway
San Diego, CA 92138

Stroup, James P
Latrobe Steel Co
2626 S Ligonier St
Latrobe, PA 15650

Thielsch, Helmut
140 Shaw Ave
Cranston, RI 02905

Valdez, Paul J
  Solar -Chief Metallurgist
  Int'l Harvester
  2200 Pacific Highway
  San Diego, CA 92138

Voorhees, Howard B
  Natl's Tech Corp
  Box 358
  Ann Arbor, MI 48107

Webster, Dr George A
  Dept Mech Engrng
  Imperial College
  London, SW7
  ENGLAND

Wells, Dr Clifford H
  Southwest Research
  P.O. Drawer 28510
  San Antonio, TX 78284

Yao, Prof J T P
  Civil Engrg
  Purdue Univ
  W Lafayette, IN 47906

Vanderveldt, Hendrixus H
  Head, Metals Engrn Br
  Code 2814
  Naval Ship R&D Ctr
  Annapolis, MD 21402

Walker, E Ken
  Box 422
  Fillmore, CA 91305

Weertman, Prof Julia R
  Dept of Mtl's Sci
  Northwestern Univ
  Evanston, IL 60201

Wilson, Jay M
  Cooper Energy Services
  Mount Vernon, OH 43050